

LASER INTERFEROMETER GRAVITATIONAL WAVE OBSERVATORY  
- LIGO -  
CALIFORNIA INSTITUTE OF TECHNOLOGY  
MASSACHUSETTS INSTITUTE OF TECHNOLOGY

<b>Document Type</b>	<b>LIGO-T980010-01 - D</b>	<b>4/23/98</b>
<b>Core Optics Support Preliminary Design</b>		
Michael Smith		

*Distribution of this draft:*

This is an internal working note  
of the LIGO Project.

**California Institute of Technology**  
**LIGO Project - MS 51-33**  
**Pasadena CA 91125**  
Phone (818) 395-2129  
Fax (818) 304-9834  
E-mail: info@ligo.caltech.edu

**Massachusetts Institute of Technology**  
**LIGO Project - MS 20B-145**  
**Cambridge, MA 01239**  
Phone (617) 253-4824  
Fax (617) 253-7014  
E-mail: info@ligo.mit.edu

WWW: <http://www.ligo.caltech.edu/>

1	PRODUCT PERSPECTIVE.....	1
	1.1. Definitions and Acronyms .....	1
	1.2. Ghost Beam Designation .....	2
2	SCATTERED LIGHT IN THE IFO.....	4
	2.1. Recap of Light Scattering Requirements .....	4
	2.2. COS Scattered Light Control Design Approach.....	4
	2.3. Estimate of Light Power Scattered into the IFO.....	5
	2.4. Scattered Light Budget for Scattering Surfaces in the ISC Portion of the PO Beam Train Outside the Vacuum Window <sup>7</sup>	
	2.4.1. COS Contribution to Scattered Light Budget.....	7
	2.4.2. IOO Contribution to Scattered Light Budget .....	9
	2.4.3. ISC Contribution to Scattered Light Budget.....	9
3	SCHEMATIC LAYOUT OF COSELEMENTS IN THE WASHINGTON INTERFEROMETER	
10		
	3.1. COS layout in the 4k interferometer.....	10
	3.1.1. HAM2 and HAM3.....	10
	3.1.1.1 Layout of HAM2 and HAM3.....	10
	3.1.2. HAM3 and BSC2.....	11
	3.1.3. HAM4 and BSC2.....	13
	3.1.4. BSC2, BSC1, and BSC8.....	15
	3.1.5. BSC2, BSC3, and BSC7.....	16
	3.1.5.1 COC Baffles and 2K ITM beam dump .....	20
	3.1.6. 4K End Stations, BSC9 and BSC10 .....	22
	3.1.6.1 COC Baffle .....	22
	3.1.6.2 ETM PO Telescope and Beam-dump for 4K ETMGBAR3 .....	22
	3.2. COS layout in the 2k interferometer.....	22
	3.2.1. BSC4.....	22
	3.2.2. BSC8/BSC7 and WB-1B/WB-1A.....	24
	3.2.2.1 2K ITM GBHR3 and GBHR4 beam-dumps, and COC baffle.....	24
	3.2.2.2 2K FM GBARX and GBARY beam-dumps .....	24
	3.2.3. Mid Station .....	25
	3.2.3.1 Baffle on BSC5/BSC6.....	25
	3.2.3.2 ETM PO Telescope and Beam-dump for 2K ETMGBAR3 .....	25
4	BEAM-DUMP .....	27
	4.1. Beam-dump Surface Reflectivity .....	27
	4.2. Beam-dump Surface Scattering .....	29
5	STRAY LIGHT BAFFLES .....	29
	5.1. Baffling of the ITM and the ETM in the arm cavity .....	29
	5.1.1. Mechanical Structure of the COC Baffle .....	30
	5.1.2. Large-angle Scattering from the ITM and ETM, Scattering Calculations	31
	5.1.3. Edge Diffraction from Aperture in the COC Baffle.....	32

5.2.	Baffle in Vacuum Manifold . . . . .	33
5.2.1.	<i>2K IFO vacuum manifold scattering geometry.</i> . . . . .	33
5.2.2.	<i>4K IFO vacuum manifold scattering geometry.</i> . . . . .	34
5.2.3.	<i>Vacuum manifold light scattering calculations</i> . . . . .	34
5.2.4.	<i>Cryopump Surface Light Scattering</i> . . . . .	36
5.2.5.	<i>Summary of vacuum manifold and cryopump light scattering calculations.</i> 37	
5.3.	COC Elliptical Baffles for Recycling Cavity . . . . .	39
5.3.1.	<i>Glint Power into the IFO from the Light Spilling Around the BS Mirror</i> 40	
5.3.2.	<i>Power Scattered from the Elliptical Baffle into IFO</i> . . . . .	40
5.3.3.	<i>Summary of Elliptical Baffle Calculations</i> . . . . .	40
5.4.	Mode-cleaner Baffles . . . . .	42
6	VERTEX (ITM, BS, AND APS) PO BEAM OPTICAL TRAIN . . . . .	44
6.1.	Wavefront Aberrations in the PO Beam Optical Train . . . . .	44
6.2.	Image Distortion and Polarization Rotation of the PO Beams . . . . .	45
6.3.	Vertex PO Telescope and ISC Telescope . . . . .	46
6.3.1.	<i>Mechanical Specifications of the ITM, BS, APS PO Telescope and ISC Telescope</i> 46	
6.3.2.	<i>PO Telescope Mounting Structure</i> . . . . .	47
6.3.2.1	<i>PO Telescope Assembly</i> . . . . .	47
6.3.3.	<i>Thermal Noise Amplitude at Test Mass Due to Telescope Assembly Mounted on SEI Platform</i> 48	
6.4.	ETM PO Telescope . . . . .	49
6.5.	PO mirror . . . . .	50
6.5.1.	<i>PO Mirror Specification</i> . . . . .	50
6.5.2.	<i>PO Mirror Mount</i> . . . . .	50
6.5.3.	<i>Thermal Noise Amplitude at Test Mass Due to PO Mirror Assembly</i> . . .	52
6.6.	Output Vacuum Window . . . . .	52
6.6.1.	<i>Output Window Specification</i> . . . . .	52
6.6.1.1	<i>Surface Figure</i> . . . . .	52
6.6.1.2	<i>Surface Scattering</i> . . . . .	52
6.6.1.3	<i>Specifications for the Vacuum Windows.</i> . . . . .	52
6.6.2.	<i>Output Window Mount</i> . . . . .	53
6.6.2.1	<i>Conflat Flange Mount.</i> . . . . .	53
6.6.2.2	<i>Differential Pressure Distortion of the Window.</i> . . . . .	53
6.7.	Faraday Isolator . . . . .	53
7	OPTICAL ALIGNMENT OF COS ELEMENTS . . . . .	54
7.1.	Alignment of beam-dumps and baffles . . . . .	54
7.2.	Alignment of PO Beam Telescope . . . . .	54
7.2.1.	<i>Telescope pre-alignment.</i> . . . . .	54
7.3.	Final alignment . . . . .	54
7.3.1.	<i>Special alignment equipment</i> . . . . .	54

	7.3.2. <i>Alignment procedure</i> . . . . .	54
	7.3.3. <i>PO Beam Initial Alignment Error</i> . . . . .	57
	7.3.4. <i>PO Beam Long-term Drift Alignment Error</i> . . . . .	57
	7.3.5. <i>PO Beam Alignment Error Correction</i> . . . . .	58
	7.3.6. <i>PO Optics Clear Aperture and Field-of-view Requirements</i> . . . . .	58
8	.....ENGINEERING MOCK-UP59	
	8.1. ITM PO Beam Optical System Mock-up . . . . .	59
	8.2. Anti-symmetric Port Pick-off Beam Optical System . . . . .	59
	8.3. BS PO Beam Optical System . . . . .	60
	8.4. ETM PO Beam Optical System . . . . .	61
	8.5. Beam-dump. . . . .	61
	8.5.1. <i>Beam-dumps in the BSC2 chamber</i> . . . . .	61
	8.5.2. <i>Beam-dumps in the HAM4 chamber</i> . . . . .	61
9	ENGINEERING TEST PLANS . . . . .	61
	9.1. Receiving Inspection. . . . .	61
	9.2. Engineering Tests . . . . .	61
	9.2.1. <i>Alignment of PO Telescopes</i> . . . . .	61
	9.2.2. <i>Wavefront Distortion of PO Telescopes</i> . . . . .	62
	9.2.3. <i>BRDF Measurement of Beam-dump Surfaces</i> . . . . .	62
	9.2.4. <i>Vibration Test of Telescope Assembly and PO Mirror Assembly</i> . . . . .	62
10	COS BILL OF ASSEMBLIES . . . . .	62
	APPENDIX 1 SCATTERED LIGHT NOISE CALCULATIONS . . . . .	66
11	SCATTERED LIGHT NOISE CALCULATIONS . . . . .	66
	11.1. Scattering from Vacuum Housing Mounted Surfaces . . . . .	66
	11.1.1. <i>APS beam scattered light power</i> . . . . .	67
	11.1.2. <i>ITM PO beam scattered light power</i> . . . . .	68
	11.1.3. <i>ETM PO beam scattered light power</i> . . . . .	69
	11.1.4. <i>SPS beam scattered light power</i> . . . . .	71
	APPENDIX 2 GHOST BEAM GLINT CALCULATIONS . . . . .	72
12	GHOST BEAM GLINT CALCULATIONS . . . . .	72
	12.1. Glint Efficiency. . . . .	73
	12.1.1. <i>Surface Curvature Efficiency</i> . . . . .	73
	12.1.2. <i>Coherence Efficiency</i> . . . . .	75
	12.1.3. <i>Total Glint Efficiency</i> . . . . .	75
	APPENDIX 3 SCATTERING FROM COC SURFACES . . . . .	76
13	SCATTERING FROM COC SURFACES . . . . .	76
	APPENDIX 4 THE EFFECT OF OPTICAL ABERRATIONS ON THE WAVEFRONT SEN-	

## SOR SIGNAL 78

14 THE EFFECT OF OPTICAL ABERRATIONS ON THE WAVEFRONT SENSOR SIGNAL  
78

- 14.1. ASAP Wavefront Model Numerical Results . . . . . 79
  - 14.1.1. 0.9 Waves Astigmatic Aberration . . . . . 79
  - 14.1.2. 0.98 Waves Spherical Aberration with 1.3 m PO telescope . . . . . 86
  - 14.1.3. Mixed 0.45 Waves Astigmatic, and 0.23 Waves Spherical Aberration with  
0.8 m PO telescope 89

APPENDIX 5 THERMAL NOISE CONTRIBUTION TO SEI PLATFORM MOTION FROM  
PO TELESCOPE AND PO MIRRORS 9115 THERMAL NOISE CONTRIBUTION TO SEI PLATFORM MOTION FROM PO TELE-  
SCOPE AND PO MIRRORS 91

- 15.1. Thermal Noise Amplitude of a Resonant Mechanical System Coupled to the SEI Platform  
91
- 15.2. Transfer Of Thermal Noise Amplitude to the Test Mass . . . . . 91
- 15.3. Maximum Noise Amplitude at Resonance . . . . . 92
  - 15.3.1. Torsional Resonance Model with Discrete Distributed Torques . . . . . 92
    - 15.3.1.1 Equivalent Torque . . . . . 93
    - 15.3.1.2 Effective Spring Constant . . . . . 93
    - 15.3.1.3 Torsional Resonant Frequency . . . . . 93
    - 15.3.1.4 Bending Resonant Frequency . . . . . 94
  - 15.3.2. Thermal Noise Amplitude at Test Mass Due to Telescope Assembly . . . . 94
  - 15.3.3. Thermal Noise Amplitude at Test Mass Due to PO Mirror Assembly . . . 94

## APPENDIX 6 EDGE DIFFRACTION . . . . . 95

- 16 EDGE DIFFRACTION . . . . . 95
  - 16.1. Effective Edge Length Reduction Due to Coherence Effects . . . . . 97
  - 16.2. Edge Diffraction from COC Baffle Aperture . . . . . 100

DRAFT

# 1 PRODUCT PERSPECTIVE

A schematic layout of the detector assembly is shown in the figure 1, indicating the physical relationship of the COS subsystem components to the rest of the detector system.

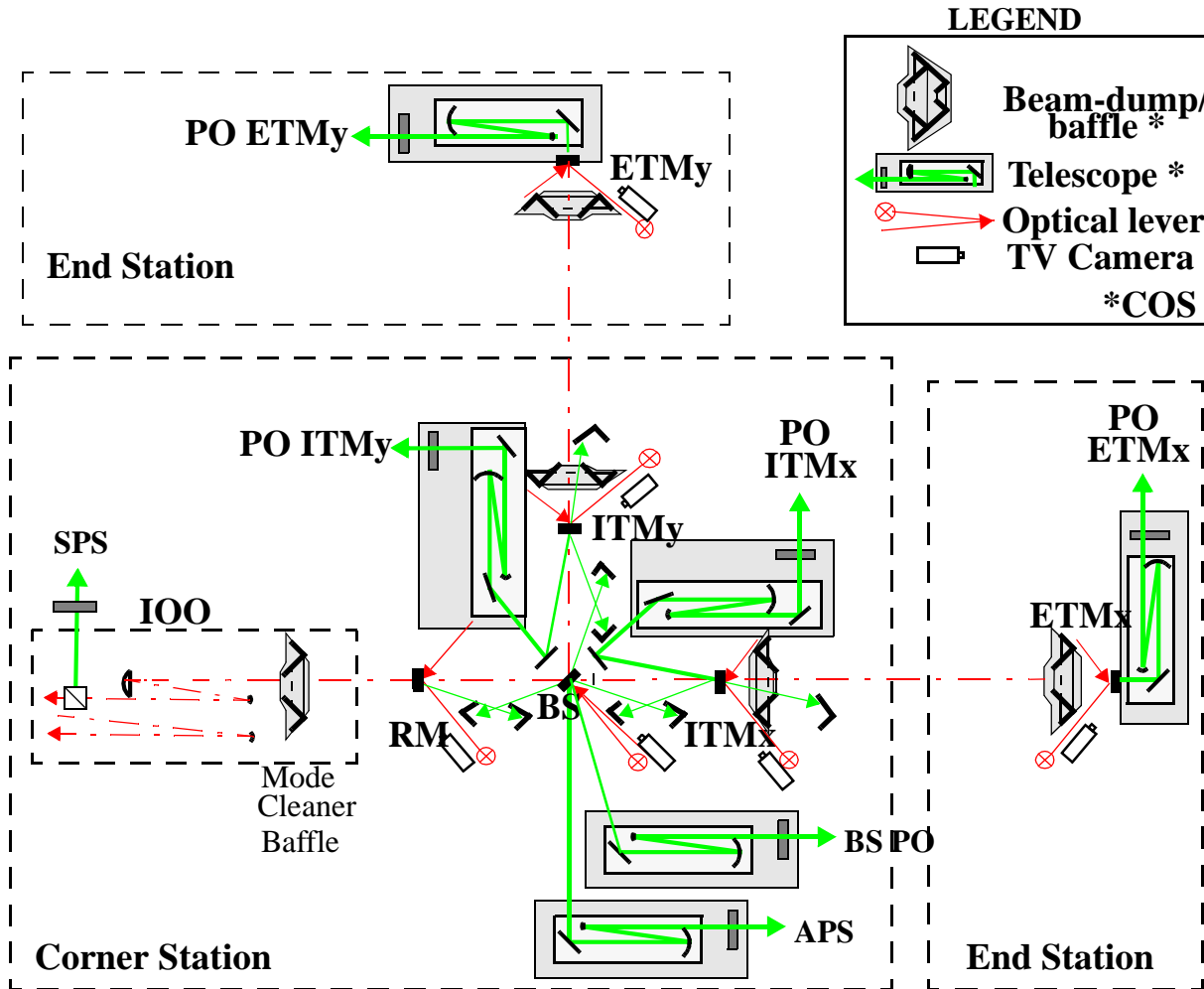


**Figure 1: Core Optics Support Subsystem Elements- Schematic Layout**

## 1.1. Definitions and Acronyms

- LIGO - Laser Interferometer Gravity Wave Observatory
- COS - Core Optics Support
- IOO - Input Optics
- DRD - Design Requirements Document
- SRD - Science Requirements Document
- RM - Recycling Mirror

- BS - Beam Splitter
- ITM<sub>x</sub>, ITM<sub>y</sub> - Input Test Mass in the interferometer 'X' or 'Y' arm
- ETM<sub>x</sub>, ETM<sub>y</sub> - End Test Mass in the interferometer 'X' or 'Y' arm
- AR - Antireflection Coating
- HR - Reflective mirror coating
- GBAR - Ghost Beam from AR side of COC
- GBHR - Ghost Beam from HR side of COC
- PO - Pick-off Beam
- beam-dump, a light trap used to absorb unwanted ghost beams
- vh - Vacuum housing
- SEI - Seismic Isolation subsystem
- SUS - Suspension subsystem
- ppm - parts per million
- ISC- Interferometer Sensing and Control
- LSC - Length Sensing and Control
- COC - Core Optics Components
- ASC - Alignment Sensing and Control
- ISC - Interferometer Sensing and Control
- IFO - LIGO interferometer
- HAM - Horizontal Access Module
- BSC - Beam Splitter Chamber
- BRDF - Bidirectional Reflectance Distribution Function
- TBD - To Be Determined
- APS - anti-symmetric port signal
- SPS - symmetric port signal
- rms - root-mean-square
- p-v, peak to valley

## 1.2. Ghost Beam Designation

The ghost beams created by the wedge surfaces of the RM, BS, ITM, and ETM are numbered according to the schematic drawing in figures 2 and 3.

The first surface reflection from the RM, ITM, and ETM COC is designated GBAR1. The main beam is designated 2. The higher order ghost beams leaving the AR surface are designated GBAR3, GBAR4, etc. The ghost beams leaving the HR surface are designated GBHR3, GBHR4, etc.

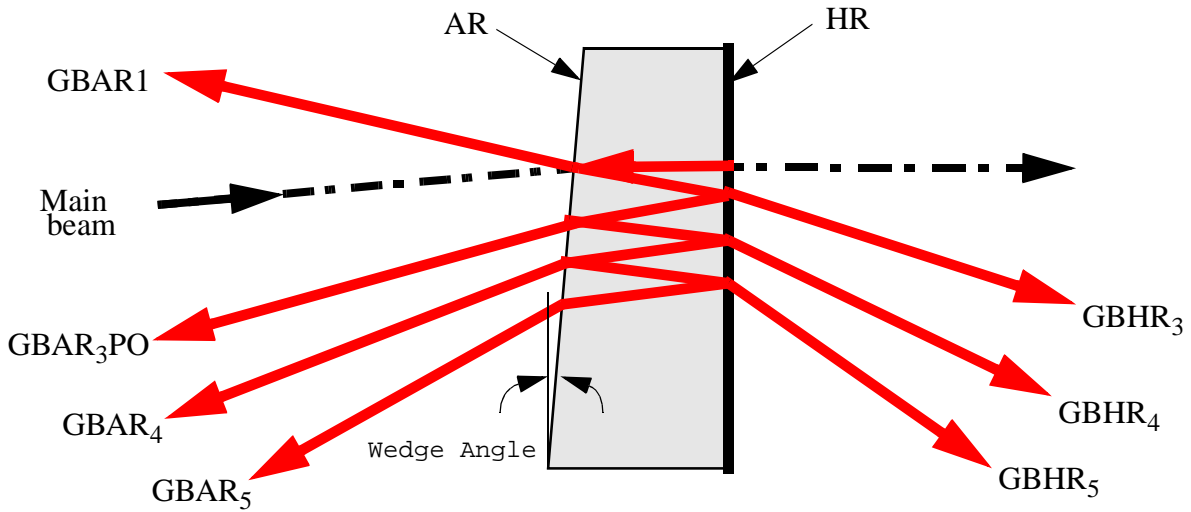


**Figure 2: Optical Beam Designation: RM, ITM, ETM**

The BS has four sets of ghost beams, as shown in figure 3. Ghost beams which originate in the +x direction are designated sub x; beams which originate in the -x direction are designated sub x'; beams which originated from the -y direction are designated sub y'.

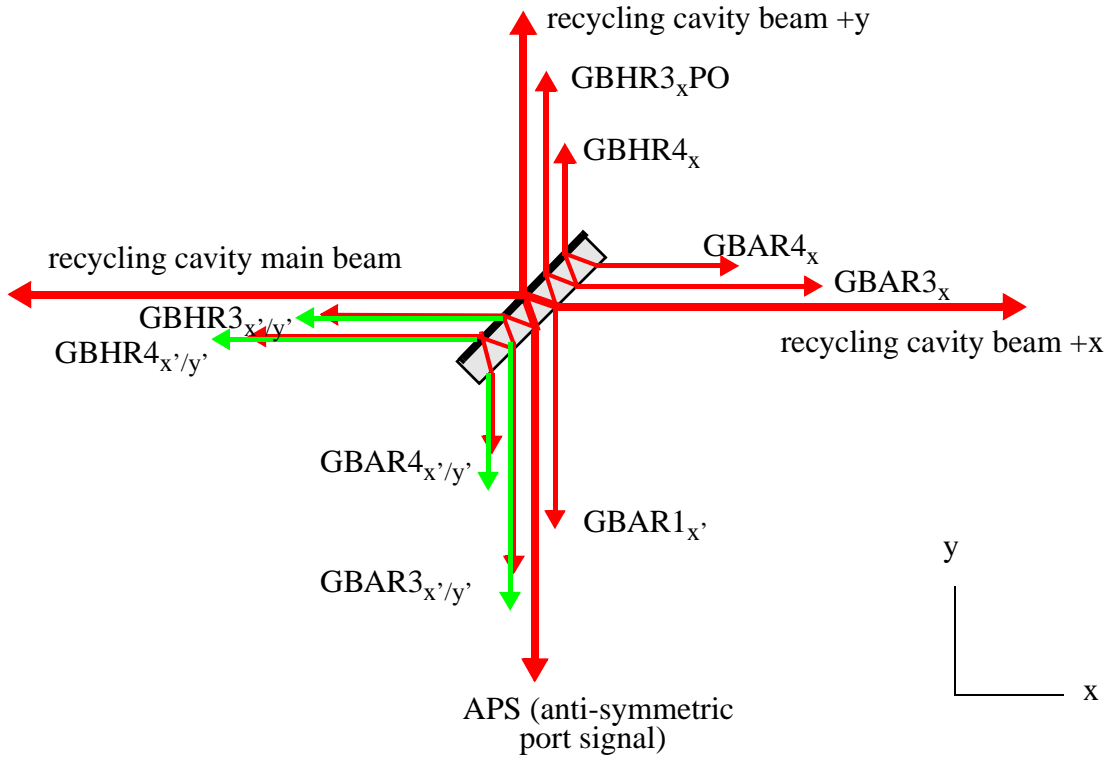


**Figure 3: Optical Beam Designation: beam splitter**



## 2 SCATTERED LIGHT IN THE IFO

### 2.1. Recap of Light Scattering Requirements

- The LIGO requirement for light power scattered back into the IFO from moving surfaces is that the resulting phase noise shall not exceed 1/10 the initial LIGO sensitivity as given in the LIGO Science Requirements Document: LIGO-E950018-02-E.
- This noise requirement was translated into a maximum total scattered power requirement for scattering from seismic floor-mounted surfaces, as described in COS DRD LIGO-T970071-01-D. The total scattered power was based on an estimate of the relative scattered light phase noise contribution from each scattering path, as described in the appendix (See “Scattered light noise calculations” on page 66.).
- The total scattered power was *optimally budgeted* within the various scattering paths so that the rms sum of the individual paths equalled the total scattered power requirement.
- The scattered power budget became the implied requirement for maximum scattered light from each scattering path.

### 2.2. COS Scattered Light Control Design Approach

The objective of the COS scattered light control design approach was to minimize the required number of baffles and beam-dumps inside the vacuum enclosure, to keep the baffles and beam-dumps off of the SEI platforms whenever possible, to minimize the light scattering budget used by COS, and to specify the maximum allowed power scattered from each PO beam by surfaces outside the vacuum enclosure which would meet the LIGO scattered light phase noise requirements.

The criteria for deciding which ghost beams should be dumped and the placement of baffles in the IFO beam path was based on the likelihood of glint reflections from the walls of the vacuum chamber causing excessive phase noise.

The maximum allowed power scattered from each PO beam *by external surfaces* places an implied requirement on the BRDF of the external scattering surfaces; which depends upon the diameter of the beam, the power spectrum of the moving surface, and the particular PO beam path.

The COS design approach is summarized in the following.

- All GBAR1, and unused GB3 ghost beams will be caught by beam-dumps mounted to the walls of the vacuum housing (See “Beam-dump” on page 32., and Table 1 on page 6)
- GB4 ghost beams with  $P_{incident} > 50 \times 10^{-6}$  watts will be dumped
- The glint from undumped ghost beams hitting the vacuum chamber will *not exceed* the scattered light requirement (See “Ghost Beam Glint Calculations” on page 72.)
- PO mirrors, PO telescopes, and all accessory PO beam optics will be rigidly mounted on SEI platforms (See “Thermal Noise Contribution to SEI Platform Motion from PO Tele-

- scope and PO Mirrors” on page 89.)
- Faraday isolator in APS beam and ND filter in ETM PO beam are *required* to balance the scattered light budget
  - Recommended  $BRDF < 8 \times 10^{-4} \text{ sr}^{-1}$  for all seismic floor-mounted optical surfaces in the demagnified PO beam train
  - Stray light baffle to block IOO mode-cleaner scattered light from entering the recycling cavity
  - Stray light baffle to block small-angle scattered light from ITM and ETM exiting the beam tube (See “Baffling of the ITM and the ETM in the arm cavity” on page 34.)
  - Cryopump baffle to hide internal reflecting surfaces of cryopump at ends of beam tubes (See “Baffle in Vacuum Manifold” on page 37.)

### 2.3. Estimate of Light Power Scattered into the IFO

A summary of the estimated scattered light power into the 4K IFO from the first two orders of ghost beams is shown in Table 1, “Summary of Scattered Light Powers from Seismic floor-mounted Surfaces,” on page 6. The calculations are described in the appendix (See “Scattered light noise calculations” on page 66.), and were based on the following parameters:

gravity wave frequency	$f=100\text{Hz},$
laser power	$P_{\text{laser}}=6\text{w},$
recycling cavity gain	$G_{\text{rc}}=50,$
telescope demagnification	$1/72,$

BRDF of windows, mirrors, and beam-dumps  $8 \times 10^{-4} \text{ sr}^{-1}$ .

Except where noted, the beam-dumps, baffles, and output windows are mounted on the vacuum housing.

The pick-off mirrors, telescopes, and attenuators are mounted on SEI platforms.

The dispositions of all the ghost beams are indicated in the last column in Table 1 on page 6. A null entry in the last column indicates that the beam is *not* dumped and consequently is assumed to glint from the wall of the BSC chambers back into the IFO. The scattered or glinted light powers in every path are within the budgeted COS scattering requirements.

Note: In order to balance the scattered light budget for all PO beam paths, it was necessary to place a Faraday isolator (or similar attenuator) with an attenuation of  $1 \times 10^{-3}$  in the APS PO beam path, and a 0.1 transmissivity attenuator in the ETM PO beam path.

**Table 1: Summary of Scattered Light Powers from Seismic floor-mounted Surfaces**

<i>Scattering Source</i>		<i>Power incident on scattering surface, watt</i>	<i>Scattered power into IFO, watt</i>	<i>Glint power into IFO, watt</i>	<i>Budgeted scattered light power requirement, watt</i>	<i>Scattered Light Power Allocation factor</i>	<i>Disposition of ghost beam</i>
RM	GBAR1	6.00E-03	NA	1.46E-14	1.0E-06	NA	
power glint into laser path toward mode cleaner							
RM	GBAR3	5.6E-03	1.5E-18		5.8E-13	1.0E-03	beam-dump
RM	GBAR4	5.5E-06		1.2E-20	5.8E-13	1.0E-03	
RM	SPS-vh-rc	1.20E-01	1.8E-12		2.4E-12	4.0E-03	ISC PO
BS	APS-vh-rc	3.00E-01	3.3E-13		3.3E-13	5.0E-01	ISC PO
BS	GBHR3x PO	7.50E-02	2.1E-14		2.1E-14	3.1E-02	ISC PO
ITMx	GBAR3 PO	1.41E-01	1.5E-13		1.5E-13	2.2E-01	ISC PO
ITMy	GBAR3 PO	1.41E-01	1.5E-13		1.5E-13	2.2E-01	ISC PO
ETMx	GBAR2 PO	3.93E-01	2.4E-12		2.4E-12	1.6E-02	ISC PO
ETMy	GBAR2 PO	3.93E-01	2.4E-12		2.4E-12	1.6E-02	ISC PO
BS	GBHR3x'	3.75E-02	1.4E-18		6.4E-16	1.0E-03	beam-dump
BS	GBHR4x'	1.87E-05		5.7E-21	6.4E-16	1.0E-03	
BS	GBHR3y'	3.75E-02	1.4E-18		6.4E-16	1.0E-03	beam-dump
BS	GBHR4y'	1.88E-05		5.7E-21	6.4E-16	1.0E-03	
RM	GBHR3	1.80E-04	8.3E-22		5.8E-13	1.0E-03	beam-dump
RM	GBHR4	1.74E-07		1.2E-23	5.8E-13	1.0E-03	
ITMx	GBAR1	1.50E-01	4.0E-17		6.8E-16	1.0E-03	beam-dump
ITMx	GBAR4	1.37E-04	3.3E-23	3.0E-19	6.8E-16	1.0E-03	beam-dump
ITMy	GBAR1	1.50E-01	4.0E-17		6.8E-16	1.0E-03	beam-dump
ITMy	GBAR4	1.37E-04	3.3E-23	3.0E-19	6.8E-16	1.0E-03	beam-dump
FMx	GBAR	7.49E-02	1.2E-17	9.1E-14	3.3E-16	1.0E-03	beam-dump
FMy	GBAR	7.49E-02	1.2E-17	9.1E-14	3.3E-16	1.0E-03	beam-dump
BS	GBAR3x	7.49E-02	2.8E-18		6.4E-16	1.0E-03	beam-dump
BS	GBAR4x	3.75E-05	6.9E-25	1.1E-20	6.4E-16	1.0E-03	
BS	GBHR4x	3.75E-05	6.9E-25	1.1E-20	6.4E-16	1.0E-03	
BS	GBAR1x'	1.50E-01	4.4E-19		6.4E-16	1.0E-03	beam-dump
BS	GBAR3x'	3.74E-02	2.7E-20		6.4E-16	1.0E-03	beam-dump
BS	GBAR4x'	1.87E-05	6.9E-27	5.7E-21	6.4E-16	1.0E-03	
BS	GBAR3y'	3.75E-02	2.8E-20		6.4E-16	1.0E-03	beam-dump

Scattering Source		Power incident on scattering surface, watt	Scattered power into IFO, watt	Glint power into IFO, watt	Budgeted scattered light power requirement, watt	Scattered Light Power Allocation factor	Disposition of ghost beam
BS	GBAR4y'	1.87E-05	6.9E-27	5.7E-21	6.4E-16	1.0E-03	
ETMx	diffuse-vh-ETM	1.00E-01	3.3E-19		3.2E-18	1.0E-03	baffle
ITMx	diffuse-vh-ITM	1.00E-01	3.3E-19		3.2E-18	1.0E-03	baffle
ITMx	GBHR3	4.36E-03	9.8E-21		2.9E-18	1.0E-03	beam-dump
ITMx	GBHR4	4.23E-06	9.2E-27	2.9E-22	2.9E-18	1.0E-03	beam-dump
ETMx	GBHR3	7.87E-09		3.8E-25	2.9E-18	1.0E-03	
ETMx	GBHR4	7.87E-12		3.8E-31	2.9E-18	1.0E-03	
ETMy	diffuse-vh-ETM	1.00E-01	3.3E-19		3.2E-18	1.0E-03	baffle
ITMy	diffuse-vh-ITM	1.00E-01	3.3E-19		3.2E-18	1.0E-03	baffle
ITMy	GBHR3	4.36E-03	9.8E-21		2.9E-18	1.0E-03	beam-dump
ITMy	GBHR4	4.23E-06	9.2E-27	2.9E-22	2.9E-18	1.0E-03	beam-dump
ETMy	GBHR3	7.87E-09		3.8E-25	2.9E-18	1.0E-03	
ETMy	GBHR4	7.87E-12		3.8E-31	2.9E-18	1.0E-03	
ETMx	GBAR3	3.93E-04	4.6E-20		1.4E-13	1.0E-03	beam-dump
ETMx	GBAR4	3.93E-07		9.5E-22	1.4E-13	1.0E-03	
ETMy	GBAR3	3.93E-04	4.6E-20		1.4E-13	1.0E-03	beam-dump
ETMy	GBAR4	3.93E-07	4.6E-26	9.5E-22	1.4E-13	NA	

## 2.4. Scattered Light Budget for Scattering Surfaces in the ISC Portion of the PO Beam Train Outside the Vacuum Window

### 2.4.1. COS Contribution to Scattered Light Budget

The scattered light budget was based on scattering from seismic floor-mounted surfaces, with a beam diameter which was demagnified by 1/72 from the IFO beam diameter. However, some of the COS elements are isolated on an SEI platform and have an incident beam diameter which is relatively larger.

The *equivalent scattered light contribution* to the budget from SEI mounted surfaces should be reduced relative to seismic floor-mounted surfaces by the factor  $3.6 \times 10^{-9}$  to account for the attenuation of the phase noise by the SEI stacks. This factor is the square of the SEI horizontal motion transfer function (see Seismic Isolation DRD, LIGO-T960065-02-D). Similarly, scattering surfaces that are suspended by the SUS will have an additional phase noise attenuation factor of

$4.9 \times 10^{-7}$ . The equivalent scattered light is also inversely proportional to the square of the demagnification factor and equivalent scattered light contribution should be scaled accordingly.

The total equivalent light power scattered into the IFO from *only* the COS PO beam optical train surfaces is shown in Table 2 on page 8. This includes scattering from the PO mirror, the PO telescope surfaces, the output turning mirrors, an optical isolator where appropriate, the two surfaces of the output window, and the ISC telescope mounted on the ISC optical table.

We have assumed a BRDF of  $1\text{E-}4 \text{ sr}^{-1}$  for the telescope primary and secondary, the internal mirror of the IOO telescope, COS Faraday isolator, turning mirrors, and output window surfaces. The BRDF of the IOO Faraday was assumed to be  $1\text{E-}3 \text{ sr}^{-1}$ . The demagnification of the PO telescope is 0.125, the demagnification of the ISC telescope is 0.278, and the demagnification of the IOO telescope is 0.05.

**Table 2: Total Equivalent Scattered Light into IFO from COS PO Beam Optical Train Surfaces**

Surface	No of surfaces	Square of SEI transfer fcn	Square of SUS transfer fcn	Equivalent Scattered Light Power, watt				
				ITM PO	BS PO	APS PO	SPS PO	ETM PO
incident power, watt				0.141	0.075	0.30	0.12	0.39
PO mirror	1	3.60E-09		1.30E-26	3.65E-27			
PO telescope primary (2 surfaces for ETM PO telescope)	1	3.60E-09	4.90E-07	1.30E-26	1.82E-27	2.86E-26	1.02E-31	4.17E-25
PO telescope secondary (2 surfaces for ETM PO telescope)	1	3.60E-09	4.90E-07	8.33E-25	1.17E-25	1.83E-24	4.08E-29	2.67E-23
PO Telescope internal	1	3.60E-09	4.90E-07				1.63E-28	
PO Telescope mirror	1	3.60E-09		8.33E-25	2.36E-26	1.83E-24		1.33E-23
attenuator	4	3.60E-09		NA	NA	7.33E-24	6.67E-21	2.67E-23
turning mirror, on SEI platform (3 mirrors for SPS PO beam)	5	3.60E-09		4.17E-24	5.83E-25	9.17E-24	2.50E-22	6.67E-23
output window	2	1.00E+00		4.63E-16	6.48E-17	1.02E-15	7.41E-15	7.41E-15
turning mirror, on ISC table	1	1.00E+00		2.31E-16	3.24E-17	5.09E-16	3.70E-15	3.70E-15
ISC Telescope objective	2	1.00E+00		4.63E-16	6.48E-17	1.02E-15		7.41E-15
ISC Telescope eyepiece	2	1.00E+00		6.00E-15	8.40E-16	1.32E-14		9.60E-14

**Table 2: Total Equivalent Scattered Light into IFO from COS PO Beam Optical Train Surfaces**

<i>Surface</i>	<i>No of surfaces</i>	<i>Square of SEI transfer fcn</i>	<i>Square of SUS transfer fcn</i>	<i>Equivalent Scattered Light Power, watt</i>				
				<i>ITM PO</i>	<i>BS PO</i>	<i>APS PO</i>	<i>SPS PO</i>	<i>ETM PO</i>
<b>subtotal COS</b>				<b>7.2E-15</b>	<b>1.0E-15</b>	<b>1.6E-14</b>		<b>1.1E-13</b>
<b>subtotal IOO</b>							<b>1.1E-14</b>	
<b>subtotal ISC</b>				<b>1.4E-13</b>	<b>2.0E-14</b>	<b>3.1E-13</b>	<b>2.4E-12</b>	<b>2.3E-12</b>
total COS, IOO, ISC				1.5E-13	2.1E-14	3.3E-13	2.4E-12	2.4E-12
required scattered light budget				1.5E-13	2.1E-14	3.3E-13	2.4E-12	2.4E-12

### 2.4.2. IOO Contribution to Scattered Light Budget

The IOO contribution to the scattered light budget is shown in Table 2, “Total Equivalent Scattered Light into IFO from COS PO Beam Optical Train Surfaces,” on page 8. It was assumed that the IOO Faraday isolator has four surfaces with each surface having a BRDF of  $1\text{E-}3\text{ sr}^{-1}$ . Even with this conservative scattering figure, the IOO surfaces do not contribute much to the total scattered light budget because they are mounted on an SEI platform, and some of the mirrors are suspended.

### 2.4.3. ISC Contribution to Scattered Light Budget

The COS and IOO surfaces account for a small fraction of the total scattered light budget of the PO beams. The difference between the COS plus the IOO contributions and the required scattered light budget forms the scattered light budget for the ISC subsystem, as shown in Table 2 on page 8.

The scattered light requirement varies proportionally to the BRDF of the scattering surface, and inversely proportionally to the Gaussian beam diameter (in mm) squared of the scattering beam and inversely as the seismic horizontal attenuation factor squared. Therefore the maximum BRDF for any surface in a particular scattering path can be scaled according to these same parameters in the following manner.

$$BRDF = 8 \times 10^{-4} \cdot \frac{d^2}{1^2} \cdot \frac{A_{SEI}^2}{1^2}$$

### 3 SCHEMATIC LAYOUT OF COS ELEMENTS IN THE WASHINGTON INTERFEROMETER

#### 3.1. COS layout in the 4k interferometer

##### 3.1.1. HAM2 and HAM3

##### 3.1.1.1 Layout of HAM2 and HAM3

Plan view and elevation view integrated layout drawings (ILD) of HAM2 and HAM3, compiled by overlaying an ASAP optical layout of the IFO beams and an AUTOCAD mechanical drawing of the vacuum equipment, are shown in figures 4 and 5.

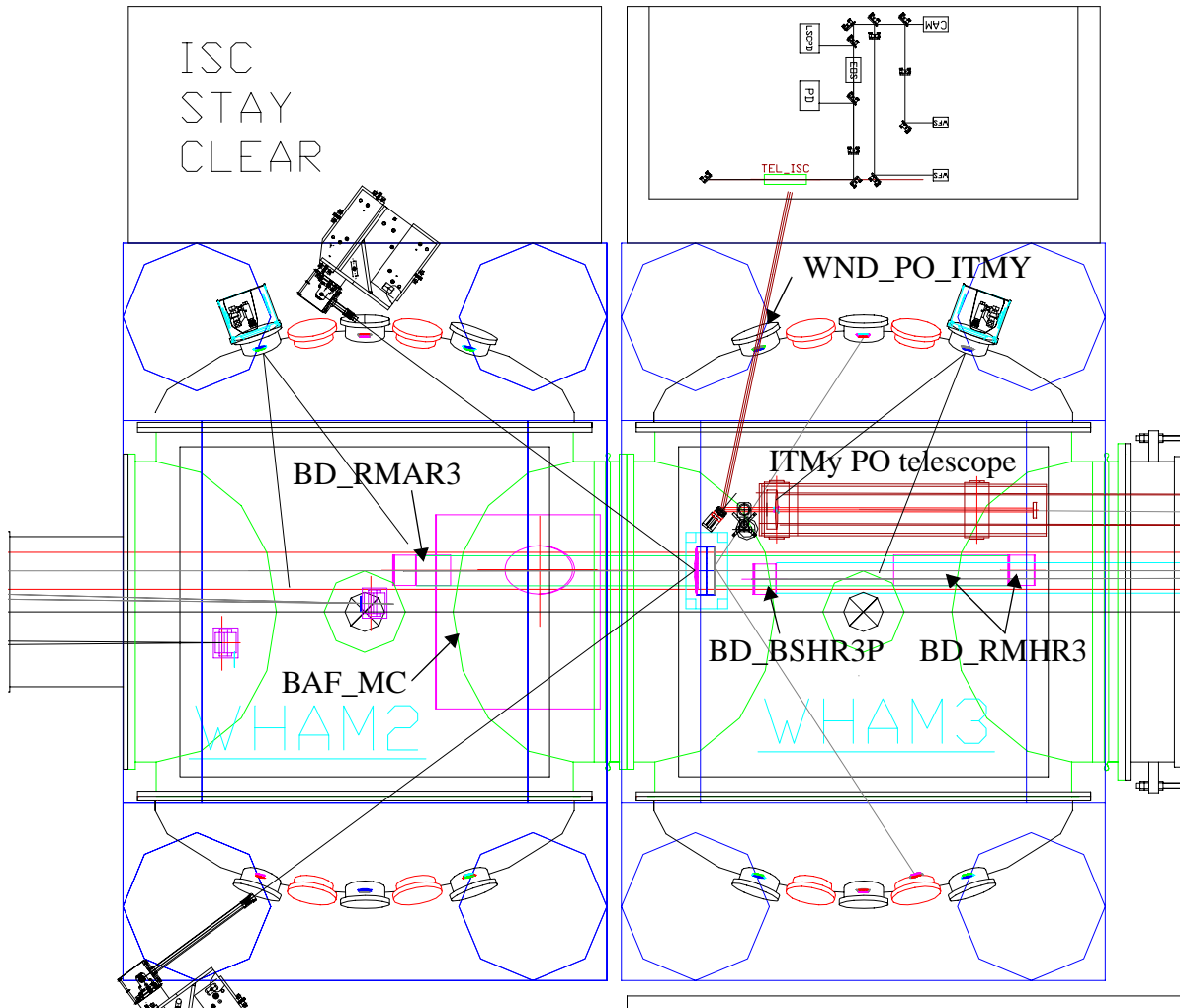
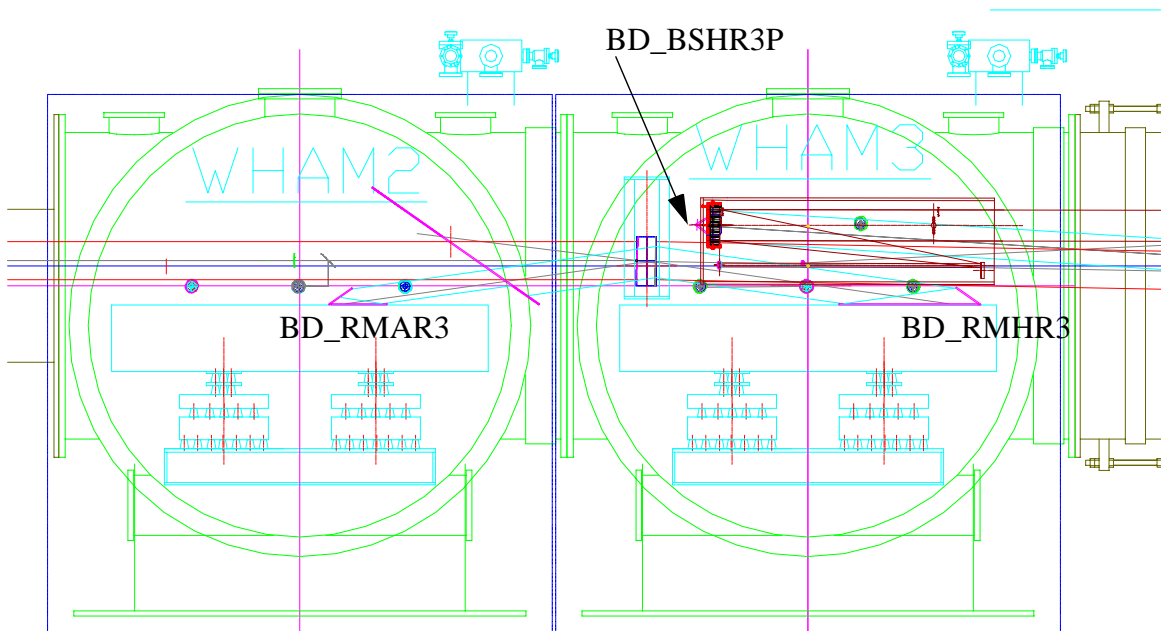


Figure 4: HAM2 and HAM 3 optical layout, plan view



**Figure 5: HAM2 and HAM 3 optical layout, elevation view**

HAM3 contains the ITM<sub>x</sub> PO beam telescope and output window. Beam-dumps for the co-linear BSGBHR3<sub>x</sub>' and BSGBHR3<sub>y</sub>' are mounted to the HAM3 housing. The ghost beam RMGBAR3 glances off the SEI platform and is caught by the half beam dump mounted to the HAM3 SEI platform.

HAM2 contains a baffle for the mode cleaner scattered light, and a beam-dump. The RMGBHR3 ghost beam glances from the SEI platform and is caught by the half beam dump mounted to the HAM2 SEI platform. A stray-light baffle is mounted to the walls of HAM2 to block the light scattered toward the RM from the mode cleaner. The baffle has an access hole for passage of the main beam and the RMGBHR3. The properties of the beam-dumps and baffles are described elsewhere. See "Beam-dump" on page 32. See "Baffling of the ITM and the ETM in the arm cavity" on page 34.

### 3.1.2. HAM3 and BSC2

An ILD elevation view of the HAM3 and BSC2 chambers, looking toward the y-arm, is shown in figure 6. HAM 3 contains the ITM<sub>y</sub> PO telescope and beam dumps for the BS and RM ghost beams. BSC2 contains the PO mirror for ITM<sub>y</sub> and beam-dumps for the ITM ghost beams.

Beam-dumps for the BSGBHR3<sub>x</sub>' and BSGBHR3<sub>y</sub>' beams are mounted on the vacuum housing above the telescope on HAM3. The beam-dump for the RMGBHR3 is comprised of a plate on the surface of the SEI table and an angled plate as shown. The locations of the beam-dumps, PO mirrors, and PO telescope can also be seen in the plan view of figure 7.



Beam-dumps for ITMxGBAR1 and ITMxGBAR4 beams are shown, mounted on the walls of the BSC2 housing. The PO mirror for the ITMyGBAR3(PO) beam is rigidly mounted to the SEI platform. See “PO Mirror Mount” on page 49. The ITMyPO beam is directed to the PO telescope on HAM3. A pair of steering mirrors is used to direct the reduced PO beam through the vacuum window on HAM3 to the ISC table.

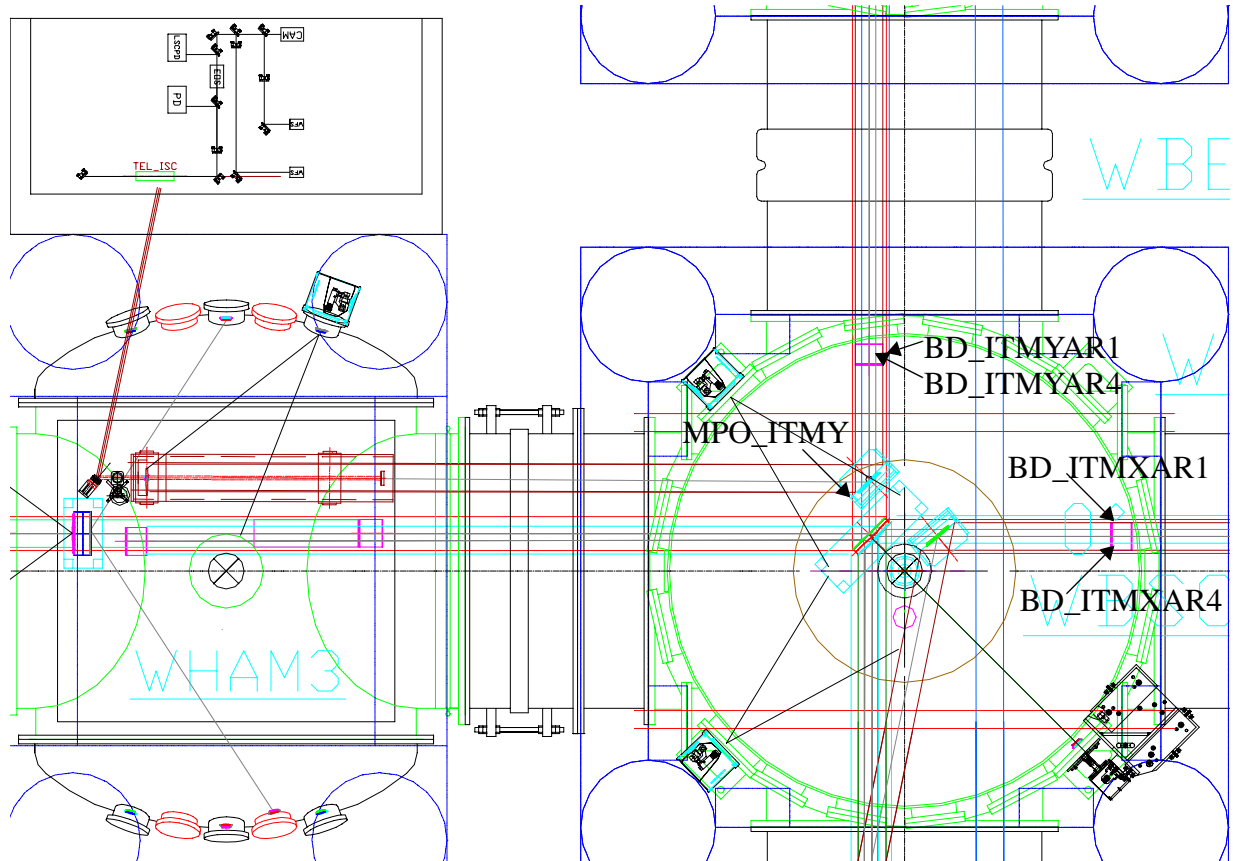


**Figure 6: ILD plan view of HAM 3 and BSC2 optics platforms, with ITM<sub>x</sub>PO and ITM<sub>y</sub>PO beam mirrors, and ITM beam-dumps**

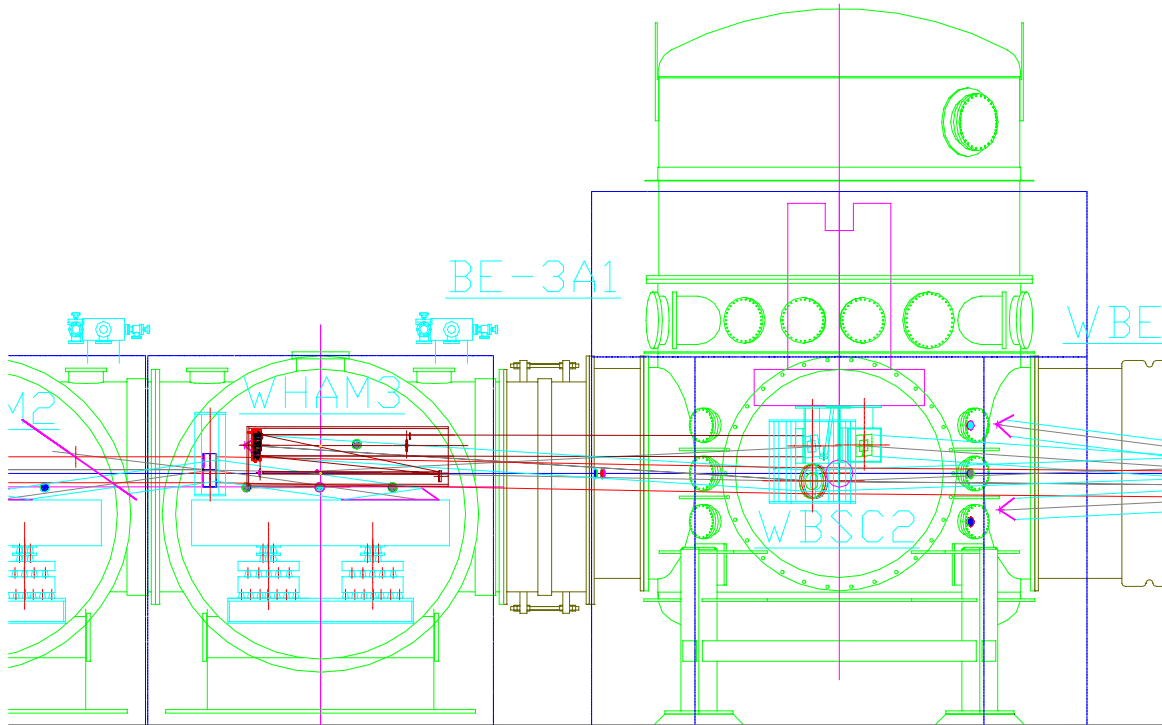


**Figure 7: ILD ELEVATION view of HAM 3 and BSC2 optics platforms, with ITM<sub>y</sub> PO beam mirrors and ITM<sub>y</sub> PO telescope; looking toward the y-arm**

### 3.1.3. HAM4 and BSC2

An ILD elevation view of the HAM4 and BSC2 chambers, looking toward the RM, is shown in figure 8. HAM4 contains the ITM<sub>x</sub> PO telescope, BS PO telescope, APS PO telescope, and beam dumps for the BS ghost beams. BSC2 contains the PO mirror for ITM<sub>y</sub> and beam-dumps for the ITM ghost beams.

The locations of the beam-dumps, PO mirrors, and PO telescope can also be seen in the plan view of figure 9.

Beam-dumps for the co-linear BSGBAR3<sub>x</sub>' and BSGBAR3<sub>y</sub>' beams are mounted on the vacuum housing above the SEI platform on HAM4. The extended beam-dump for the BSGBAR1<sub>x</sub>', which glances across the top of the SEI platform, is comprised of a partial beam dump at the front edge of the platform mounted on the vacuum housing and a partial beam-dump mounted to the SEI platform. A beam-dump for ITM<sub>y</sub>GBAR4 beam is mounted on the walls of the BSC2 housing.

The PO mirror for the ITMxGBAR3(PO) beam is rigidly mounted to the BSC2 SEI platform and directs the beam to the telescope on HAM4. Pairs of steering mirrors are used to direct the three reduced PO beams through the vacuum windows on HAM4 to the ISC table.

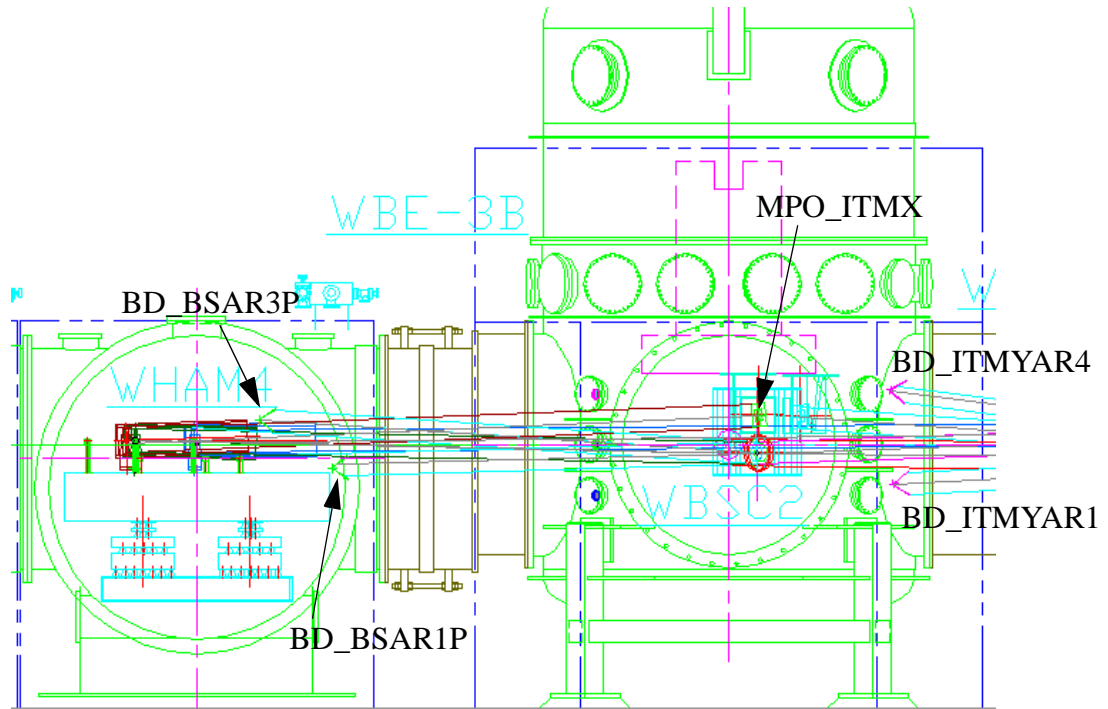


**Figure 8: ILD elevation view of HAM4 and BSC2 optics platforms, looking toward the RM**

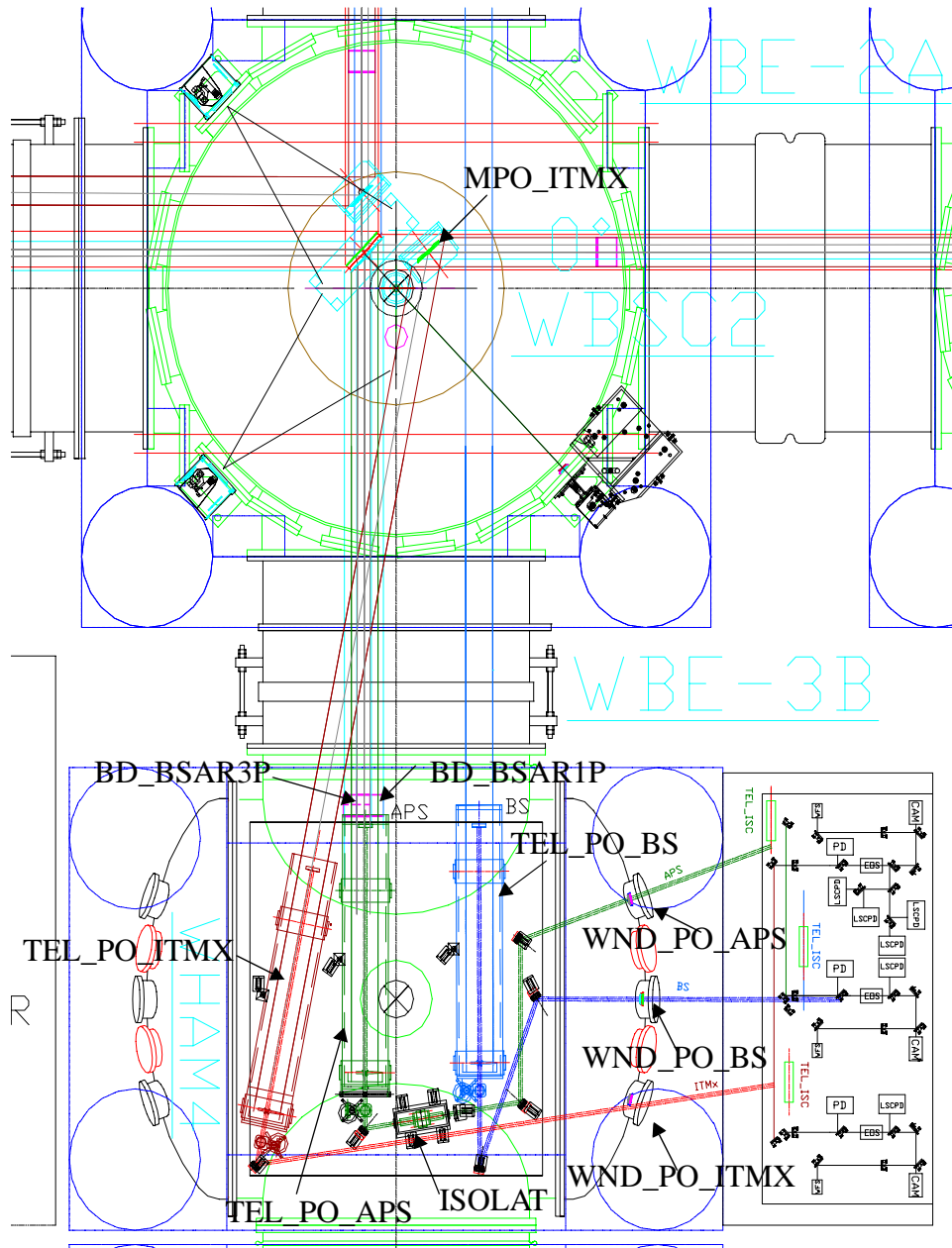


**Figure 9: ILD plan view of HAM4 and BSC2 optics platforms, with  $ITM_x$  PO beam mirror, APS PO, BS PO, and  $ITM_x$  PO telescopes**

### 3.1.4. BSC2, BSC1, and BSC8

The beam-dumps for the 4KITMy GBHR3, GBHR4, and 4KBS GBAR3x ghost beams are mounted on the wall of the neighboring BSC8, as shown in the elevation view figure 10, and the plan view figure 11. BSC8 also contains the 2K fold mirror, 2K ITMy, and a beam-dump for the 2K BSGBAR3x ghost beam.

The 4K BS PO mirror, mounted to the SEI platform of BSC1, directs the 4KBS GBHR3x (PO) beam to the PO telescope on HAM4.

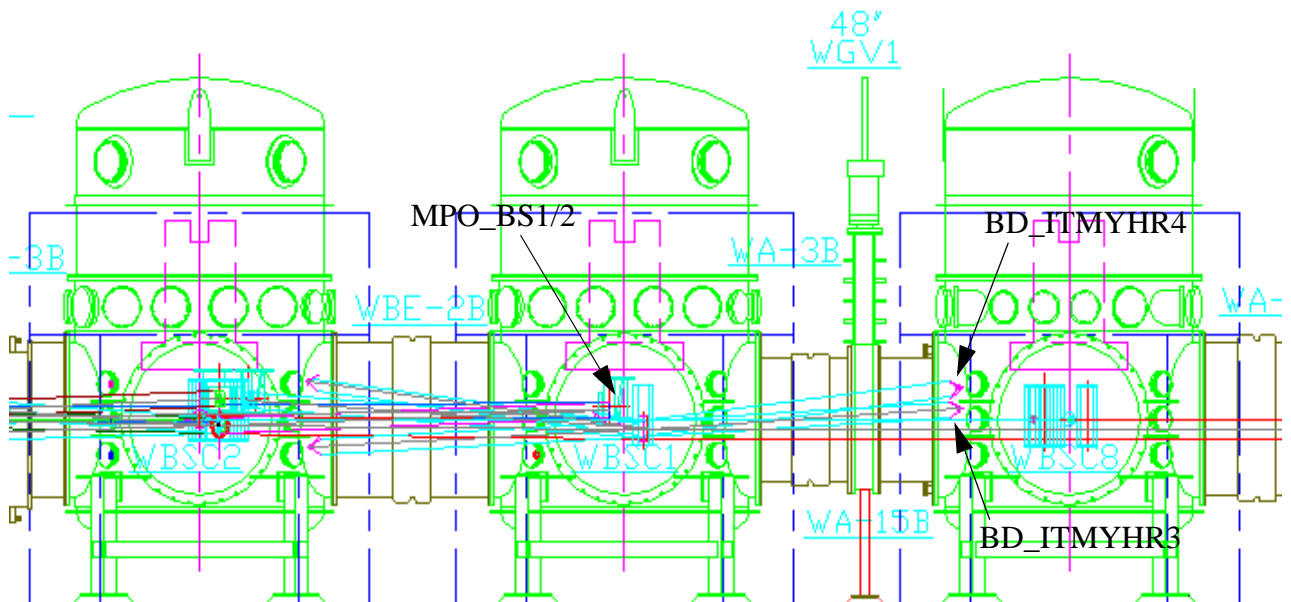


**Figure 10: ILD elevation view of BSC2, BSC1 and BSC8**

### 3.1.5. BSC2, BSC3, and BSC7

Similarly, the beam-dumps for the 4KITMx GBHR3, and GBHR4 ghost beams are mounted on the wall of the neighboring BSC7, as shown in the elevation view figure 12 and the plan view figure 13. BSC7 also contains the 2K fold mirror, 2K ITMx, and a PO mirror for the 2K BSGBHR3x (PO) beam.

A detail of the beam-dump for the 4KBS GBAR3x beam on BSC3 is shown in figure 14.

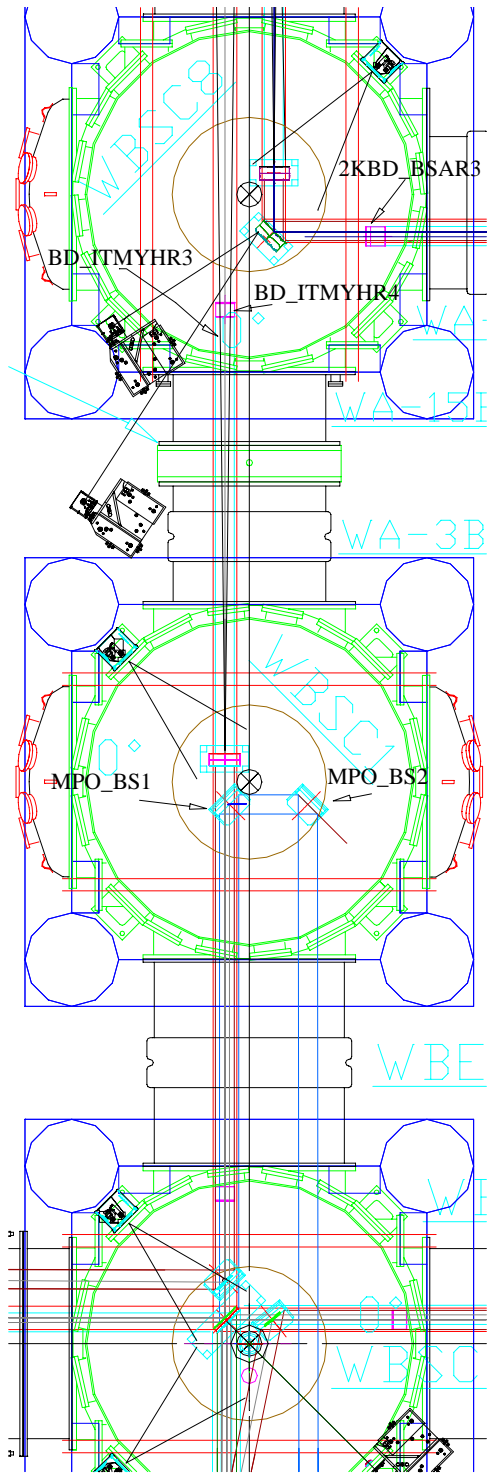
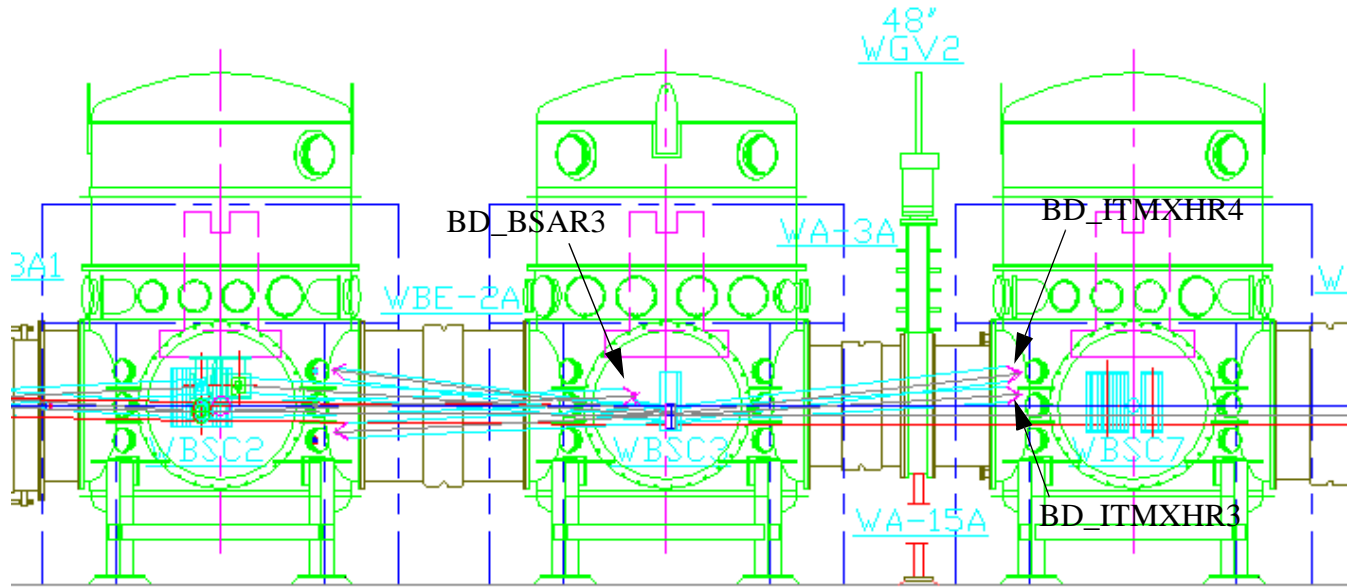


Figure 11: ILD plan view of BSC2, BSC1 and BSC8



**Figure 12: ILD elevation view of BSC2, BSC3 and BSC7**

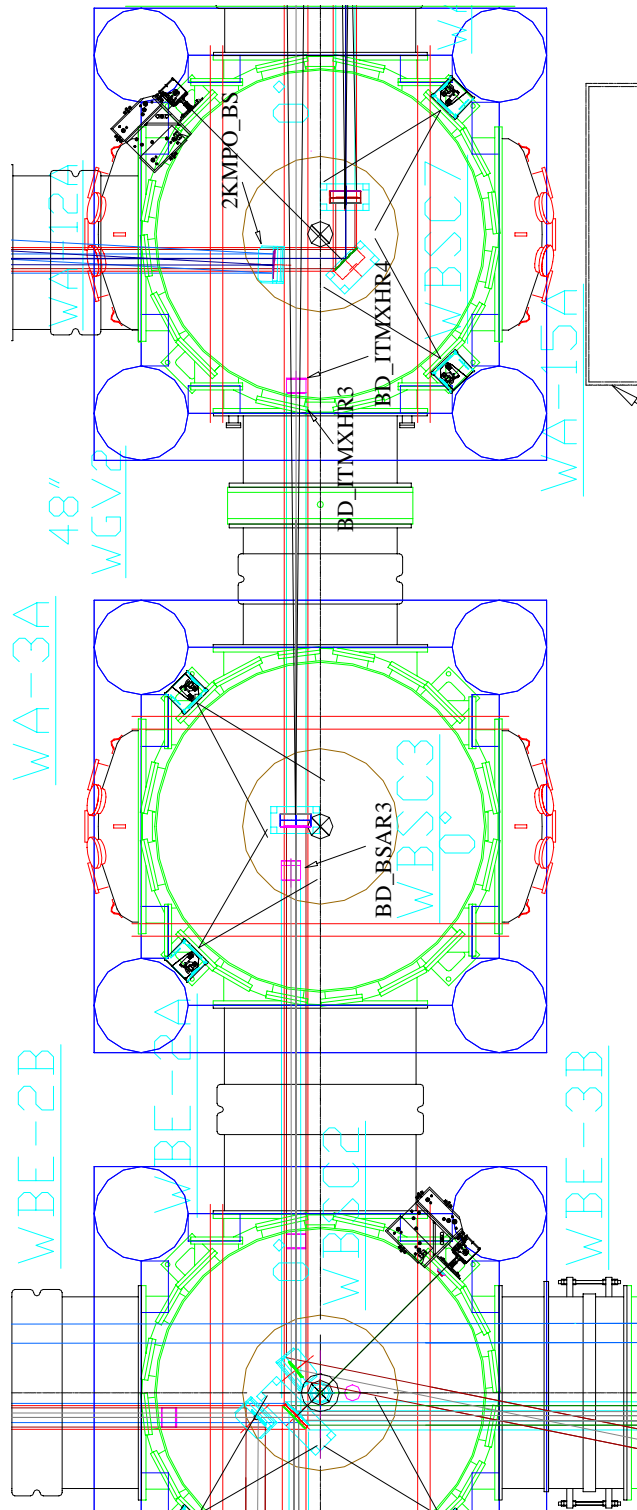
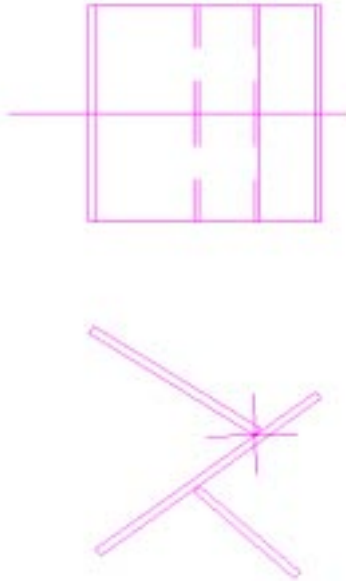


Figure 13: ILD plan view of BSC2, BSC3 and BSC7





**Figure 14: Detail of 4KBS GBAR3x beam-dump on BSC3**

### 3.1.5.1 COC Baffles and 2K ITM beam dump

Baffles to block the low-angle scattered light from the ETMs at the far end of the beam tubes will be mounted on the walls of spools WB1-A and WB1-B facing toward the 2K ETM<sub>x</sub>, 4K ETM<sub>x</sub>; and 2K ETM<sub>y</sub>, 4K ETM<sub>y</sub> respectively. Refer to the plan and elevation views shown in figures 15 and 16. COC baffles are also placed at the mid station in BSC5 and BSC6, and at the end station in BSC9 and BSC10. In the Washington IFO, the baffles contain clear apertures to allow passage of both the 4K and 2K IFO main beams. In the Louisiana IFO, the baffles will have a single clear aperture to allow passage of the 4K main beam. An analysis of the baffle performance is given in “Stray Light Baffles” on page 34. The baffles also serve as beam-dumps for the 2KITM GBHR3, GBHR4 ghost beams, as shown in the elevation view figure 16.

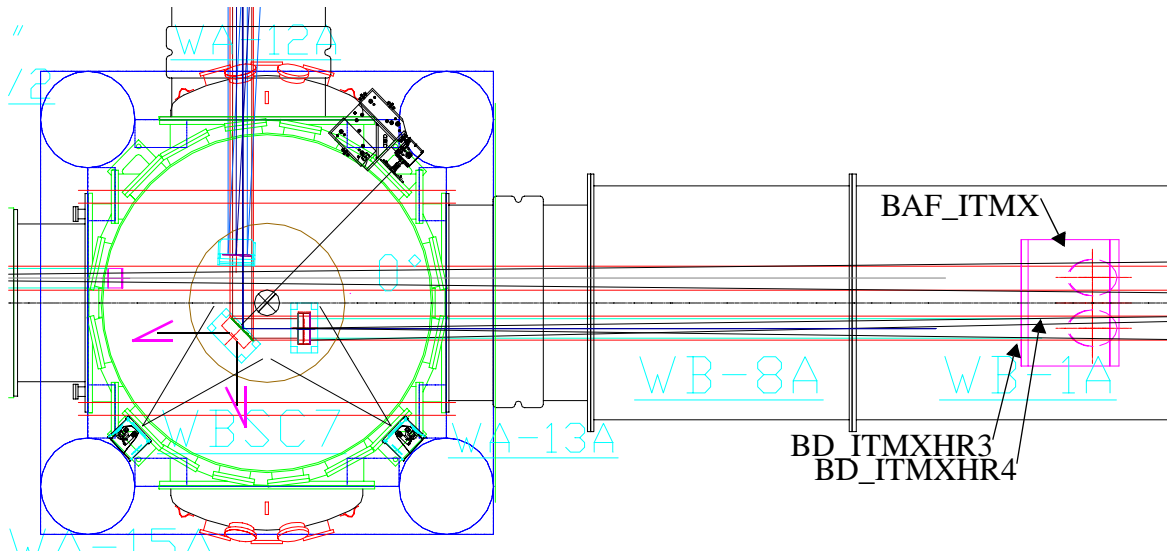


**Figure 15: COC baffle ITMx and 2K ITMx beam-dump, plan view**

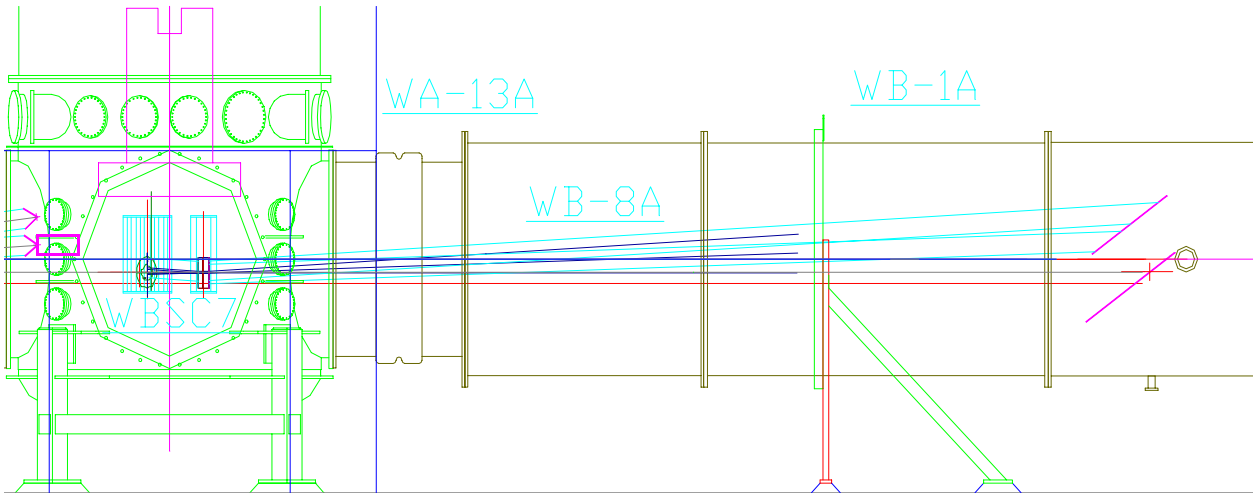


**Figure 16: COC baffle ITMx and 2K ITMx beam-dump, elevation view**

### 3.1.6. 4K End Stations, BSC9 and BSC10

#### 3.1.6.1 COC Baffle

A baffle will be mounted on the walls of BSC9 (x-arm) and BSC10 (y-arm) facing toward the ITM end of the arm cavity to intercept small angle scattered light from the ITM, as shown in figure 17.

#### 3.1.6.2 ETM PO Telescope and Beam-dump for 4K ETMGBAR3

PO telescopes for the 2K ETM<sub>x</sub> and ETM<sub>y</sub> PO beams will be suspended from the BSC9/BSC10 SEI platforms. The telescopes contain a 0.1 transmissivity attenuator. The telescopes also contain integral beam-dumps for the ETM GBAR3 beams.

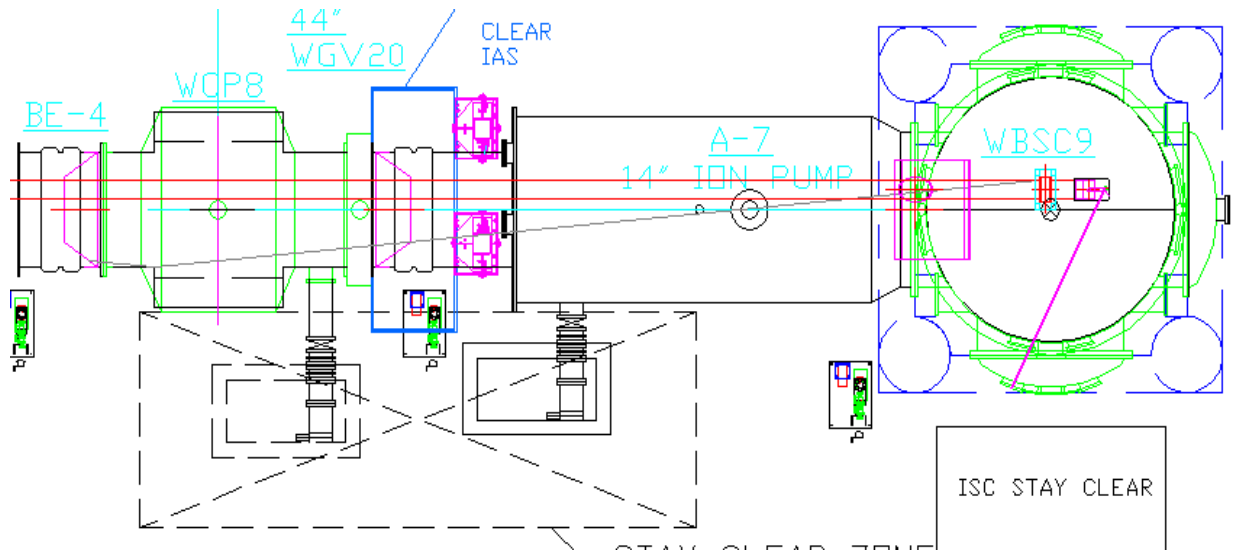


Figure 17: ILD elevation view of BSC9, showing ETM baffle and ETM PO beam.

## 3.2. COS layout in the 2k interferometer

### 3.2.1. BSC4

The elevation view of BSC4 and HAM9 in figure 18 shows that the 2K BS wedge angle is not large enough to deviate the BSGBHR<sub>3<sub>x</sub>'/y</sub> beam sufficiently to clear the RM. Part of BSGBHR<sub>3<sub>x</sub>'/y</sub> does clear the RM and will be dumped with a beam-dump suspended from the SEI platform near the RM. The part that is reflected back toward the BS will be dumped on an additional beam-dump mounted to the vacuum housing. The portion which hits the edge of beam-dump BD-HAM9 will diffract into the solid angle of the IFO. The diffracted power is large enough so that the beam-dump must be mounted to the SEI platform in order to reduce the scat-

tered light phase noise. beam-dump BD-HAM9 will be suspended from the SEI platform to avoid coupling of excessive thermal noise.

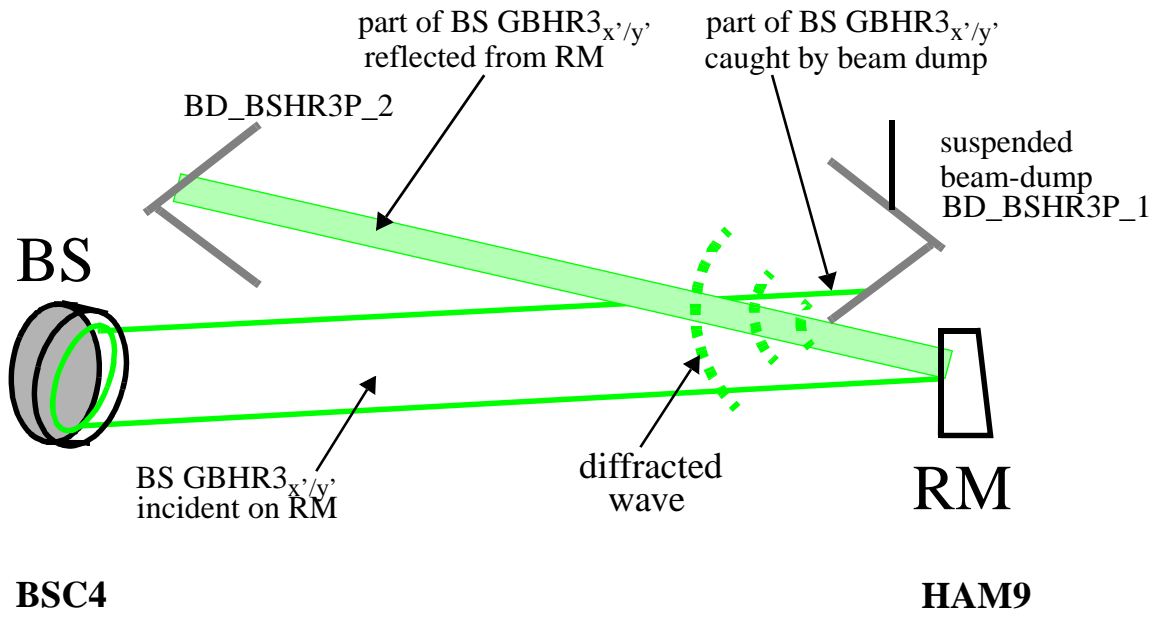
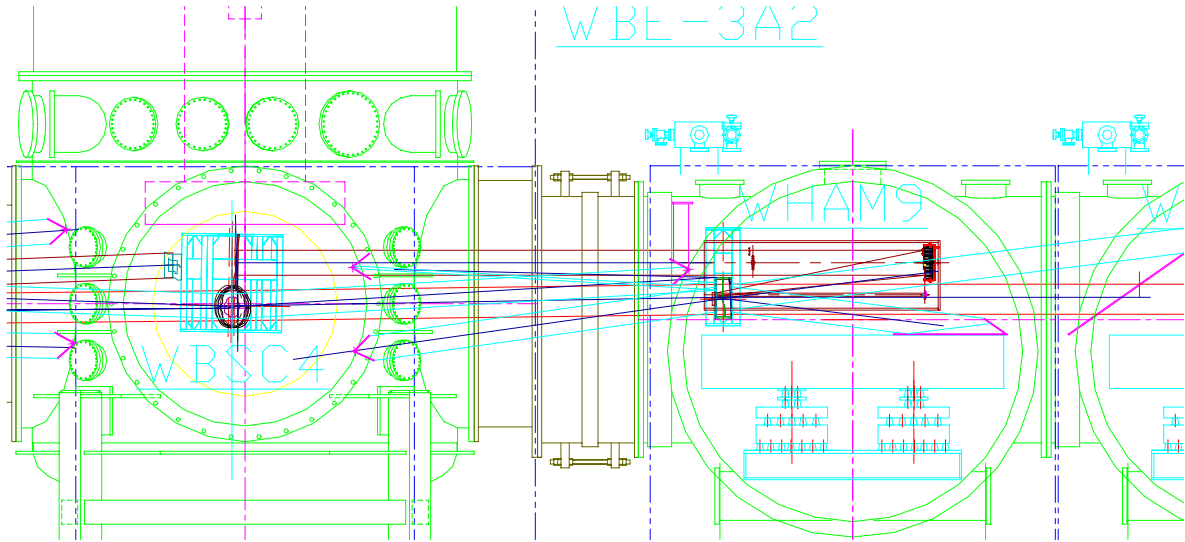


**Figure 18: 2K BSGBHR3x'/y' Beam-dump Detail in BSC4 and HAM9. Part of the BG is Dumped at RM, the Part Reflected from RM Is Dumped at BS.**

The diffracted light power can be estimated using Sommerfeld diffraction theory<sup>1</sup>. See “Edge diffraction” on page 92. The geometry of the source will be approximated as an illuminated edge of length  $w$  equal to the gaussian beam parameter, with a width of a few wavelengths, e.g.  $10\lambda$ .

Then the diffracted power can be written as

$$P_d = \frac{P_T}{\pi w^2/2} \cdot e^{-2r_0^2/w^2} \cdot 10\lambda l \cdot \frac{\sin \frac{\alpha_0}{2}}{4 \cos \alpha_0} \cdot 2\theta_0$$

Aside from the trigonometric factor, the result can be interpreted as a cylindrical wave diffracting from a line source of length  $l$  and width  $10\lambda$  into the solid angle of the IFO.

The fractional power retro-diffracted into the IFO solid angle from an edge which is tipped at various complimentary incidence angles is shown in figure 47. For this data, the beam center is displaced from the edge by 36.4 mm (equal to the beam parameter). A fraction  $2.7 \times 10^{-12}$  will be edge-diffracted back into the IFO from an edge tipped at 35 deg complimentary incidence angle. With a laser power of 300 W inside the recycling cavity, it is estimated that 0.030 W will be incident on the edge. Therefore the maximum diffracted light power into the IFO will be  $8 \times 10^{-14}$  W.

This exceeds the requirement of  $< 6.4 \times 10^{-16}$  shown in Table 1 on page 11 for scattering of the BS GBHR3x’y’ beams into the recycling cavity from a vacuum-housing-mounted surface. A factor  $>10$  attenuation in the horizontal seismic motion will be achieved by *suspending the beam-dump from the vacuum housing*. This will reduce the effective scattered light power by a factor  $>100$  to meet the requirements.

### 3.2.2. BSC8/BSC7 and WB-1B/WB-1A

#### 3.2.2.1 2K ITM GBHR<sub>3</sub> and GBHR<sub>4</sub> beam-dumps, and COC baffle

The 2K ITM GBHR<sub>3</sub> and GBHR<sub>4</sub> beam-dumps are an integral part of the COC baffle which is mounted to the vacuum housing inside the spools WB-1B/WB-1A, as shown in figure 19.

The baffle will face toward the ETM end of the arm cavity and will intercept small-angle scattered light from the 2K ETM and 4K ETM, as shown in figures 19.

#### 3.2.2.2 2K FM GBARX and GBARY beam-dumps

Beam-dumps for the GBARX and GBARY ghost beams which transmit through the HR coating of the FM are mounted to the walls of BSC7 and BSC8 in the x and y arms of the 2K IFO, as shown in figure 19.

---

1. private communication, Rai Weiss, see also Born & Wolf, Principles of Optics, 6th Ed, 1993

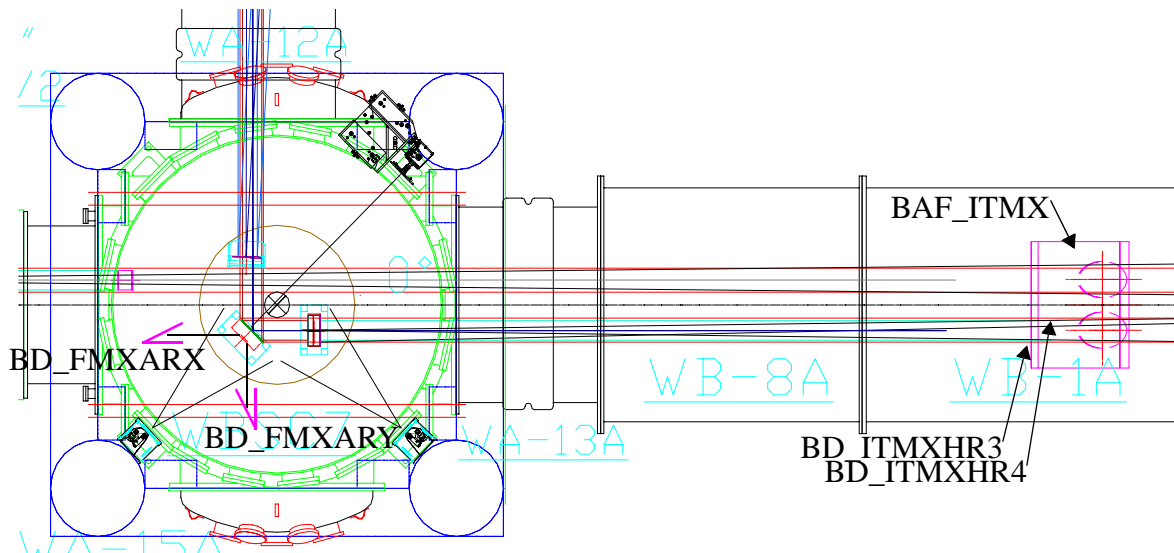


**Figure 19: Plan view of 2K ITM beam-dump/baffle, showing passage of the 4K LIGO main beam**

### 3.2.3. Mid Station

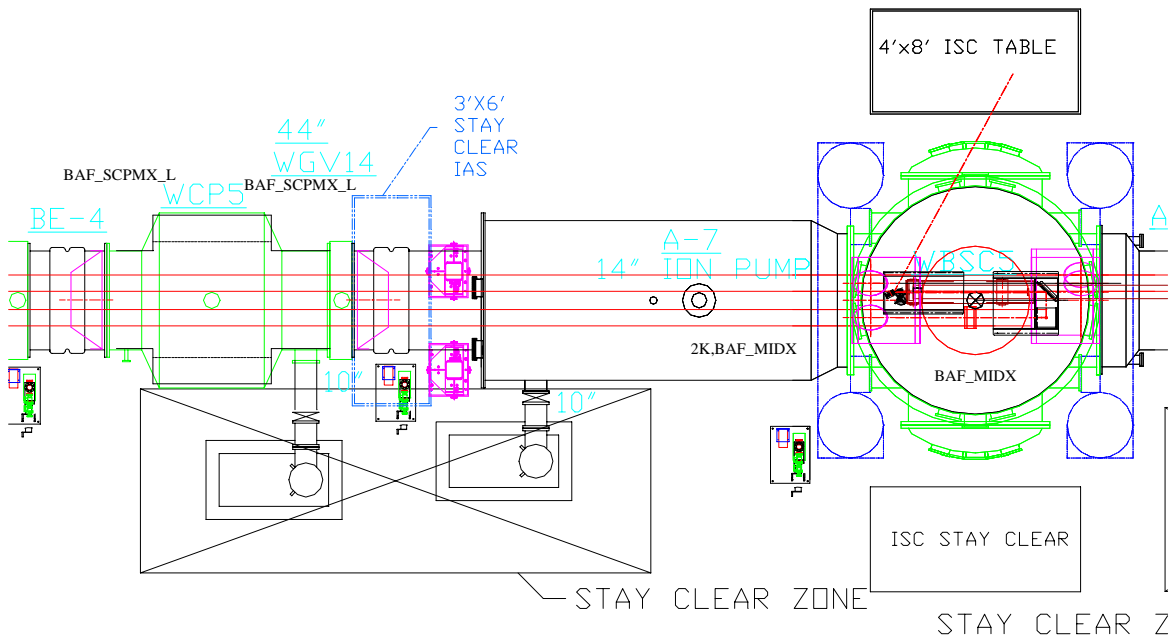
#### 3.2.3.1 Baffle on BSC5/BSC6

A baffle will be mounted on the wall of the BSC5/BSC6 at the mid station of the 2K IFO facing toward the ITM end of the arm cavity to intercept small-angle scattered light from the ITM, as shown in figure 20.

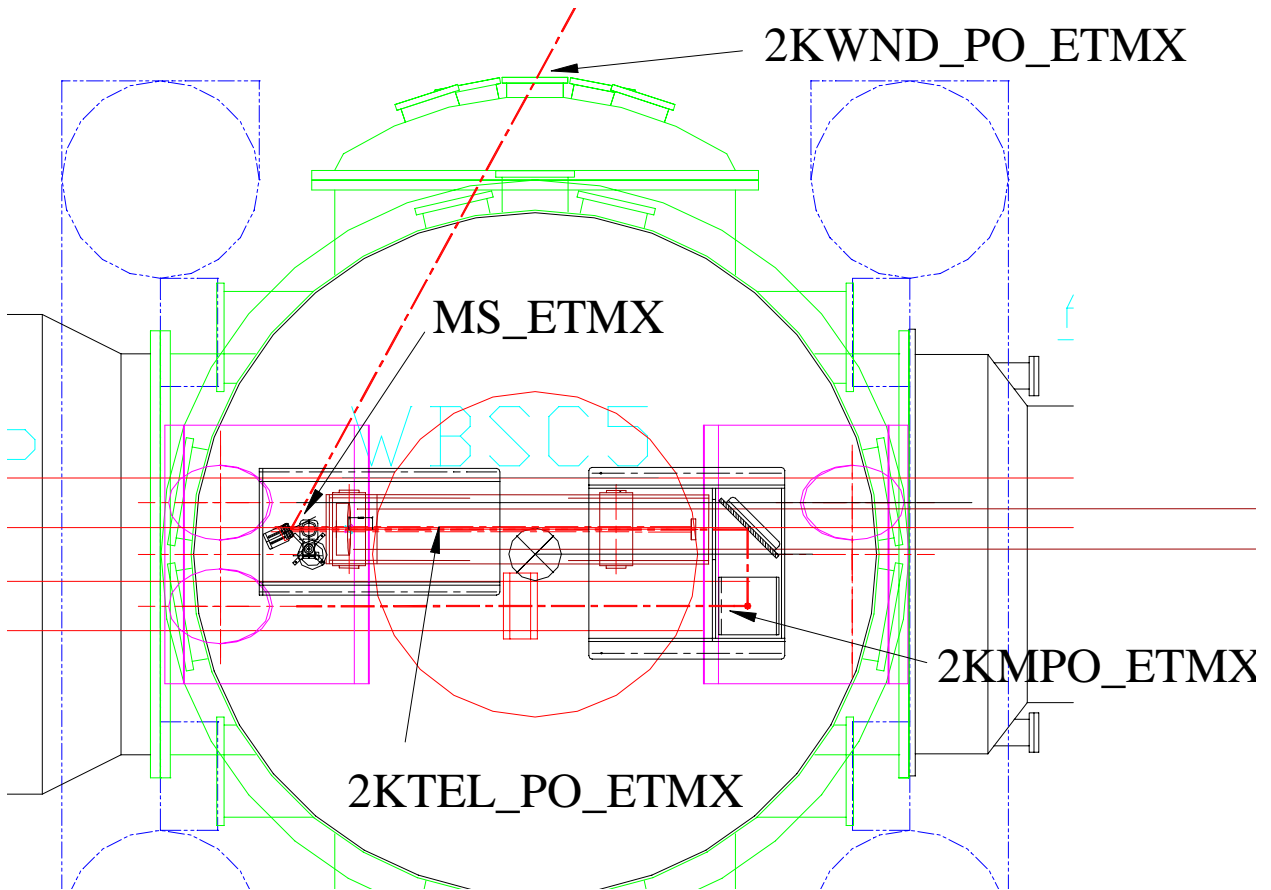
#### 3.2.3.2 ETM PO Telescope and Beam-dump for 2K ETMGBAR3

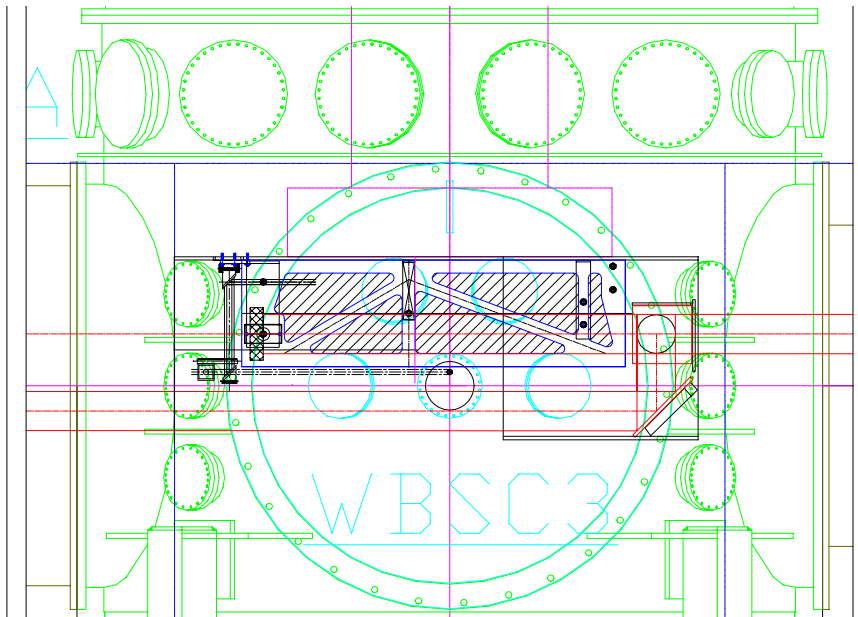
PO telescopes for the 2K ETM<sub>x</sub> and ETM<sub>y</sub> PO beams will be mounted to the BSC5/BSC6 SEI platforms, as shown in figures 21 and 22. The telescopes contain a 0.1ND output attenuator. The telescopes also contain integral beam-dumps for the ETM GBAR3 beams.

The PO beam transmitted through the HR side of the ETM is redirected into the telescope by means of a three-mirror periscope assembly. The output beam from the telescope is directed toward the output vacuum window by means of a two-mirror periscope. The resulting image rotation can be corrected outside on the ISC table with a dove prism if necessary.



**Figure 20: Plan view at the mid station of the 2K IFO showing the cryopump baffles, the ETM baffle, and the 2K ETM PO beam with ETMx PO telescope**



**Figure 21: ETM PO telescope at mid station, plan view****Figure 22: ETM PO telescope at mid station, elevation view**

## 4 BEAM-DUMP

### 4.1. Beam-dump Surface Reflectivity

The beam-dump will be made from two plates of IR absorbing glass, with a mounting structure to attach it to the wall of the vacuum chamber. The principle of operation is shown in figure 23. The full width of the incident ghost beam will reflect from the surface of the first piece of glass which is oriented at Brewster's angle with respect to the p-polarization of the ghost beam. The beam will not hit the edge of the plates in order to minimize edge diffraction. The first surface reflectivity is expected to be  $< 0.002$ , and the ghost beam will undergo at least one more reflection with a reflectivity of  $< .04$ . Therefore, the net reflectivity of the ghost beam from the beam-dump apparatus is expected to be  $< 8 \times 10^{-5}$ . This meets the beam-dump reflectivity requirement in the COS DRD of  $< 5 \times 10^{-3}$ . A measurement of the reflectivity of Schott IR glass indicated a reflectivity for p-polarization  $< 0.002^1$ .

A preliminary design concept for the beam-dump is shown in figure 24.

---

1. private communication Rai Weiss.



# beam-dump assembly

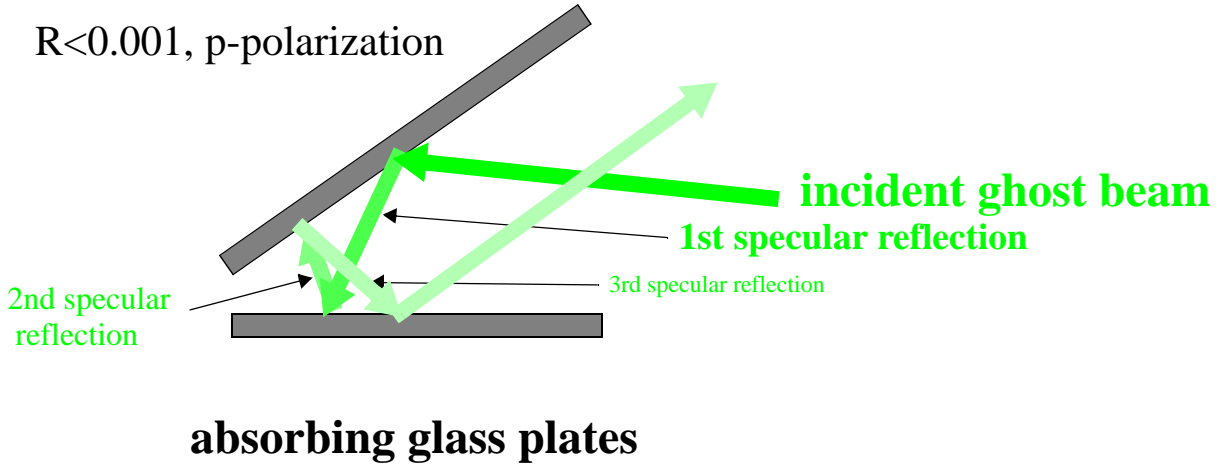


Figure 23: Beam-dump principle

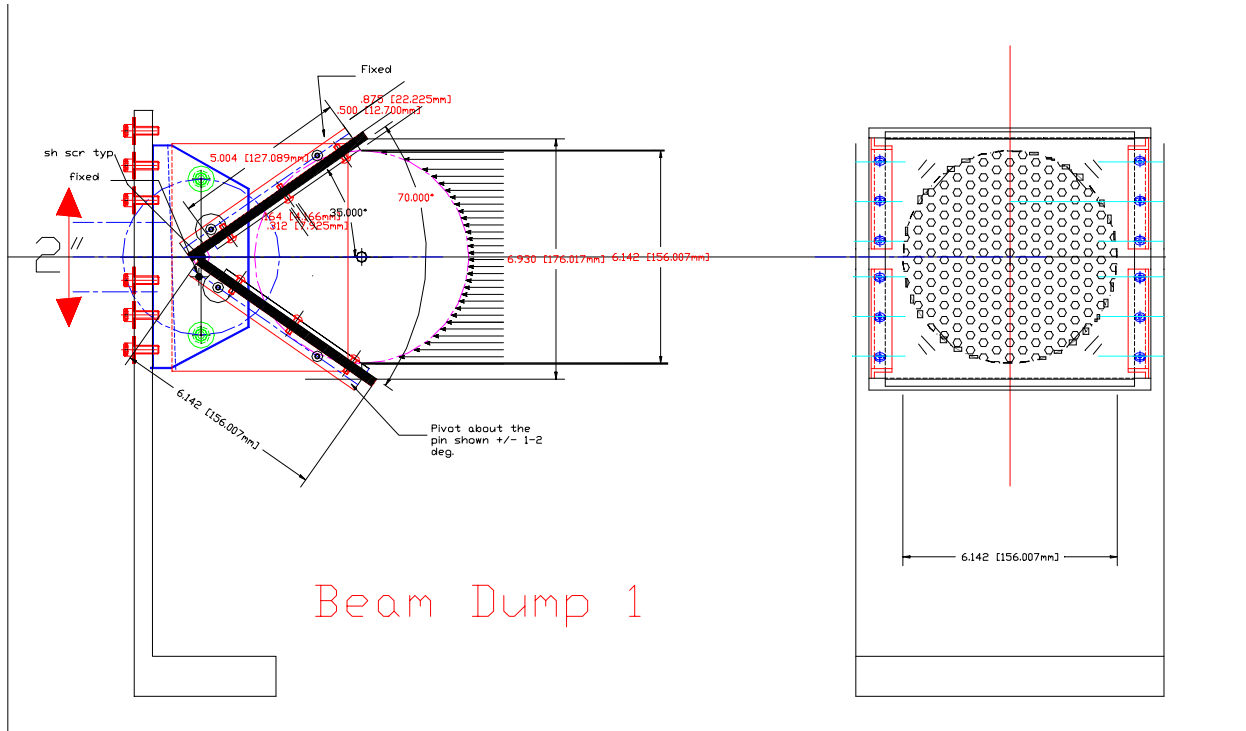


Figure 24: Design concept for a beam-dump

## 4.2. Beam-dump Surface Scattering

A measurement<sup>1</sup> of the BRDF of Schott IR absorbing glass at 55 deg incidence angle indicated a value

$$\text{BRDF} = 1 \times 10^{-4} \text{sr}^{-1},$$

which meets the scattering requirement  $\text{BRDF} < 1.7 \times 10^{-2} \text{sr}^{-1}$  for the beam-dump as described in the COS DRD.

## 5 STRAY LIGHT BAFFLES

### 5.1. Baffling of the ITM and the ETM in the arm cavity

The baffle shown schematically in figure 25 is designed to block the ETM diffusely scattered light from hitting the surfaces of the BSC vacuum housing, backscattering onto the ETM, then scattering again from the ETM into the IFO. The stray light baffle will attenuate the scattered light as a result of the relatively small BRDF of the baffle surface with several reflections within the baffle at near-Brewster's angle incidence. The reflected light from the baffle will be redirected toward the beam tube walls at a large enough angle so that the probability of scattering back into the IFO will be relatively small. In exactly the same manner, the diffusely scattered light from the ITM will be blocked, as shown in figure 26.

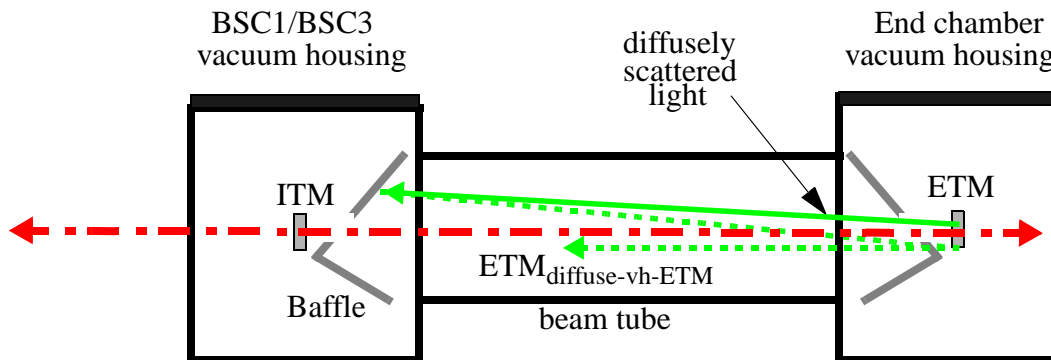


**Figure 25: Diffuse Scattering from ETM, then Backscattered from the BSC Vacuum Housing, and Re-scattered by ETM into the IFO**

1. private communication Rai Weiss.

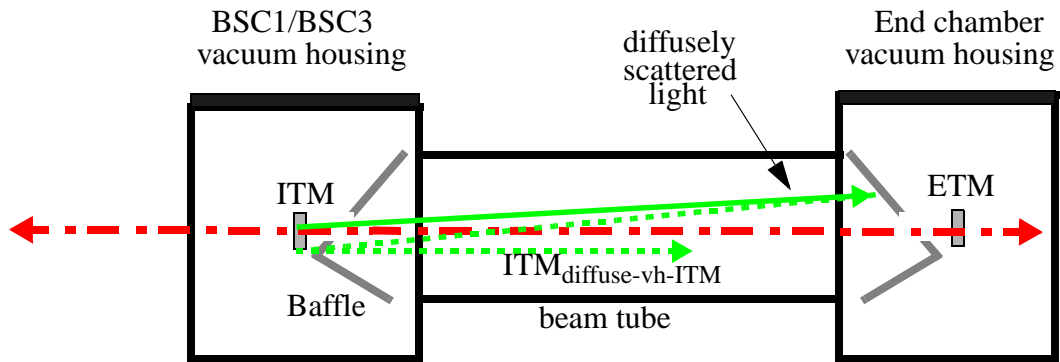


**Figure 26: Diffuse Scattering from ITM, then Backscattered from the End Vacuum Housing, and Re-scattered by ITM into the IFO**

### 5.1.1. Mechanical Structure of the COC Baffle

The stray-light baffle surfaces will be fabricated from several sheets of the same absorbing glass material used for the beam-dumps. The surfaces will be tilted at approximately Brewster's angle to the beam-tube axis. The tilt of the surfaces will also discourage any parasitic cavity resonances between the two opposing stray light baffles. A preliminary detail of the COC baffle is shown in figure 27.

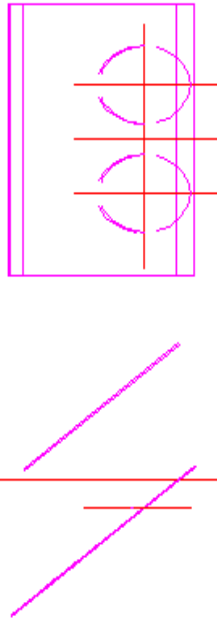
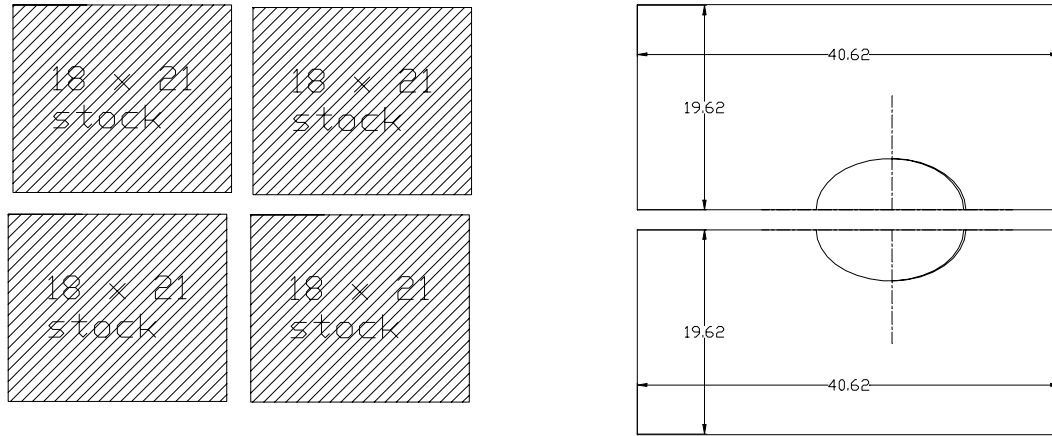


**Figure 27: Detail of COC baffle**

The baffle surface will be divided into segments to enable the use of standard-sized absorbing glass panels, as shown in figure 28. Segmented panels will also facilitate the baking of the baffle in a smaller vacuum oven.



Glass Material in Std. 18 x 24  
Size

**Figure 28: Glass panel fabrication approach for the COC baffle**

### 5.1.2. Large-angle Scattering from the ITM and ETM, Scattering Calculations

The diffusely scattered light  $P_{diff}$  from the COC passing out the ends the beam tube may hit the chamber walls and cause a glint back into the IFO beam. *The glint would exceed the scattering noise requirement as shown in Table 3 on page 32. However, the glint will be blocked by the COC baffles.* The scattered light from the COC baffles meets the LIGO scattering requirement.

The glint power can be estimated as follows (See “Ghost Beam Glint Calculations” on page 72.).

$$P_g = P_{diff} \cdot \frac{2R\lambda}{\pi^2 w^2} \eta_{glint}$$

Some of the light hitting the baffle will be backscattered to the original ITM or ETM source surface and then re-scatter back into the IFO. The power scattered into the IFO is given by the following

$$P_s = P_{diff} \cdot BRDF_{baff} \cdot \frac{A_{COC}}{L^2} \cdot BRDF_{COC} \cdot \Delta\Omega$$

The light power back-scattered from the COC baffles into the IFO was calculated using the following values:

BRDF of baffle	$BRDF_{baffle} = 1 \times 10^{-3} \text{ sr}^{-1}$
area of COC scattering surface	$A_{COC} = \pi r^2 = 4.9 \times 10^{-2} \text{ m}^2$
separation between 4K COC and baffle	$L = 4000 \text{ m}$
separation between 2K COC and baffle	$L = 2000 \text{ m}$
BRDF of COC at $3.0 \times 10^{-5}$ rad incidence angle	$BRDF_{COC}(3 \times 10^{-5} \text{ rad}) = 1 \times 10^3 \text{ sr}^{-1}$
scattering acceptance cone	$\Delta\Omega = 2.7 \times 10^{-10} \text{ sr}$

The results are shown in Table 3 on page 32.

**Table 3: Summary of Scattering from COC in Arm Cavity Out the End of the Beam Tube**

<i>Parameter</i>	<i>4K</i>	<i>2K</i>
scattered power out the beam tube, watt	0.110	0.140
radius of chamber wall, m	1.5	1.5
ITM beam parameter, w, mm	36.3	26.9
ETM beam parameter, w, mm	45.7	31.5
ITM glint power from chamber wall, watt	$2.7 \times 10^{-13}$	$4.9 \times 10^{-13}$
ETM glint power from chamber wall, watt	$1.7 \times 10^{-13}$	$3.6 \times 10^{-13}$
scattered power from COC baffle, watt	$9.1 \times 10^{-20}$	$4.6 \times 10^{-19}$
scattered light requirement, watt	$3.2 \times 10^{-18}$	$3.2 \times 10^{-18}$

### 5.1.3. Edge Diffraction from Aperture in the COC Baffle

The main beam will diffract from the edges of the aperture in the COC baffle, as shown in figure 29. The diffracted power into the IFO from the 124 mm radius aperture ITM COC baffle tilted 33 deg from the beam axis was calculated to be  $2.0 \times 10^{-24}$  watts. Similarly, the power diffracted into the IFO from the tilted ETM COC baffle with a 124 mm radius aperture is  $6.4 \times 10^{-21}$  watts. See “Edge diffraction” on page 95. This values *do not exceed* the scattered light power requirements for diffuse light in the arm cavity  $< 3 \times 10^{-18}$ , see Table 1 on page 11.

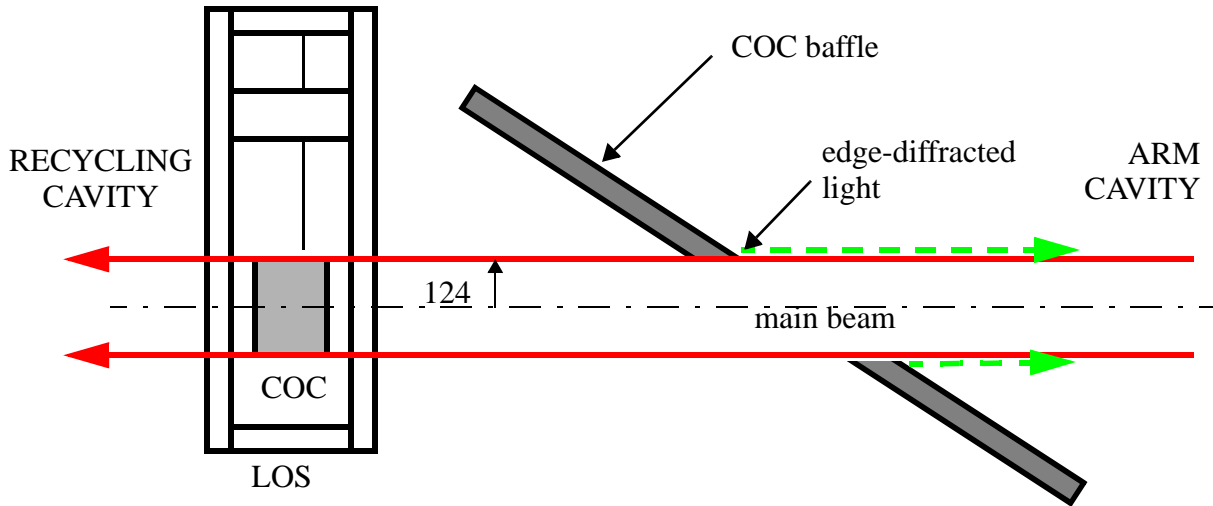


**Figure 29: Edge diffraction by COC baffle**

## 5.2. Baffle in Vacuum Manifold

The following discussion will show that 1) *baffles are not needed in the vacuum manifold segments at both ends of the beam tubes*, 2) *baffles are needed at the near side of the cryopumps*.

### 5.2.1. 2K IFO vacuum manifold scattering geometry

The light scattered at small-angles from the surface of the 2K ITM mirror (shown in green) toward the beam tube will backscatter from the bare walls of the vacuum manifold, then re-scatter from the surface of the 2K ITM into the IFO. The predominant scattering surfaces as shown in figure 30 are the walls of the following vacuum manifold sections: B-8A, B-1A, BE-5A, B-9A, A-1A, the cryopump liner surfaces of CP2, BE-4A, the beam tube, BE-4C, the cryopump liner surfaces of CP5, and A-1C. Only light scattered from the vacuum manifold surfaces in the 2 km length section of the beam tube out to the mid station need be considered, because scattered light from surfaces beyond the mid-section will be blocked by the stray-light baffle in front of the 2K ETM and

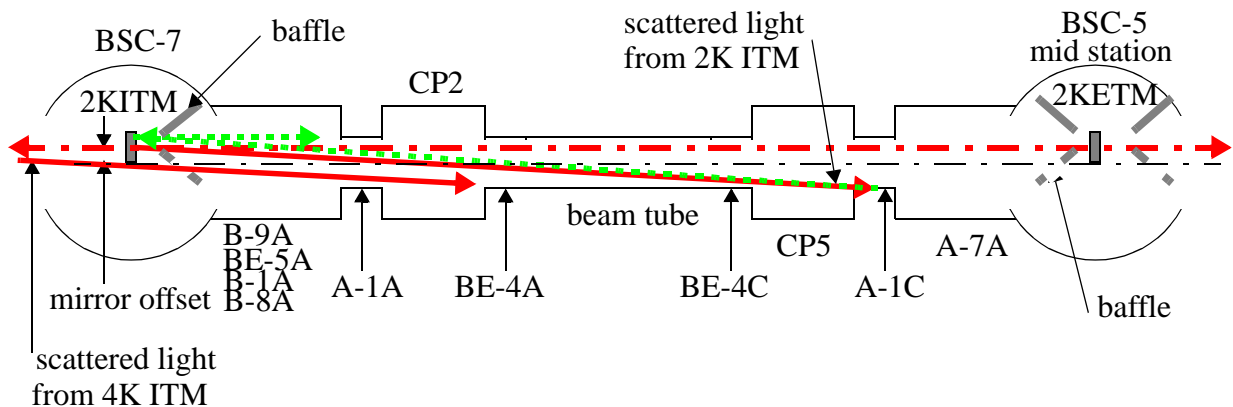


**Figure 30: 2K IFO, scattered light from ITM, backscattering from vacuum manifold walls (shown in green) then re-scattering from ITM into the IFO.**

will not scatter into the 2K ITM.

The light scattered from the 2K ETM mirror will backscatter from the same walls of the vacuum manifold described above, except in reverse order; and will then re-scatter from the surface of the ETM into the IFO.

In addition, light scattered from the surface of the 4K ITM mirror on BSC-3 toward the beam tube, as shown in figure 31, will pass through the 4K beam hole in the baffle at BSC-7 and will scatter from the same surfaces of the vacuum manifold described above in the near 2km section of the IFO.

### 5.2.2. 4K IFO vacuum manifold scattering geometry

The light scattered from the surface of the 4K ETM toward the beam tube (shown in green) will backscatter from the bare walls of the vacuum manifold, then re-scatter from the surface of the 4K ETM into the IFO, as shown in figure 31. The scattering surfaces are the walls of the following vacuum manifold sections: A-7C, A-1E, the cryopump liner surfaces of CP8, BE-4G, the beam tube, BE-4E, the cryopump liner surfaces of CP6, and A-14A.

In addition, a portion of the 4K ITM scattered light will also pass through the 4K beam holes in the mid station baffles on BSC-5 and will be intercepted by the 4K ETM baffle.

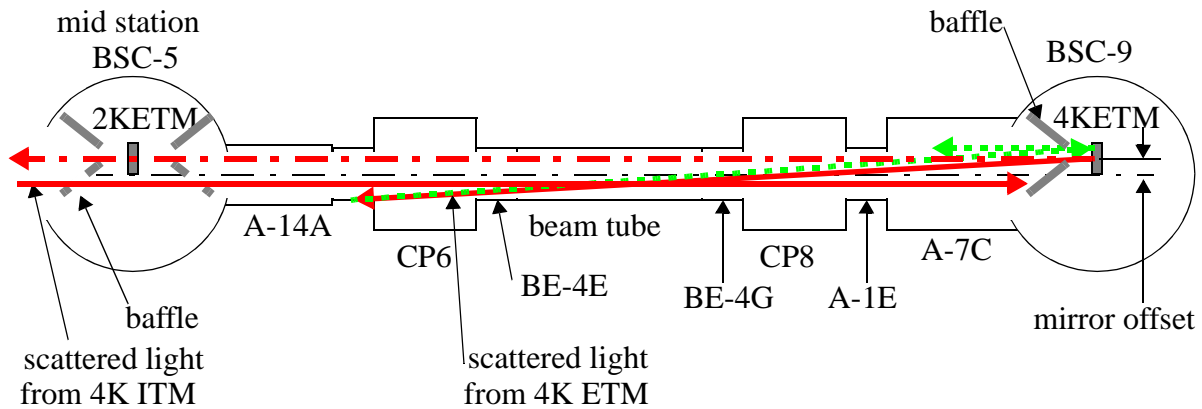


**Figure 31: 4K IFO, scattered light from ETM, backscattering from vacuum manifold walls (shown in green) then re-scattering from ETM into the IFO.**

### 5.2.3. Vacuum manifold light scattering calculations

The light scattered from the COC surface out to the IFO wall is highly dependent upon the micro roughness, which determines the large angle scattering characteristics of the COC. In order to provide a conservative estimate of the COC large angle scattering, the BRDF data from the Pathfinder sample CSIRO, surface 2, S/N 2 was used; which exhibits greater microroughness than the GO S/N 5 sample. The measured BRDF( $\theta$ ) is described by the following analytic expression<sup>1</sup> for large angles.

$$BRDF(\theta) = 2.53 \times 10^{-8} \cdot \theta^{-2.472} sr^{-1} \text{ for } \theta > 3.4 \times 10^{-5} rad .$$

The differential light power scattered from the vacuum manifold walls or the beam tube baffles into the IFO beam is given by

$$dP_s = P_{ac} \cdot BRDF_{COC} \cdot d\Omega \cdot BRDF_{wall} \cdot \frac{A_{COC}}{l^2} \cdot BRDF_{COC} \cdot \Delta\Omega ,$$

where  $P_{ac}$  is the arm cavity power incident on the COC,  $l$  is the distance to the scattering wall, and  $r$  is the radial distance from the COC mirror center to the scattering surface.

$d\Omega = 2\pi \sin\theta d\theta = 2\pi\theta d\theta$ .  $\theta = \frac{r}{l}$ , using a small angle approximation, and assuming that the scattering is symmetric about the COC.

The mirror offset effect on the scattering angle will be approximated by separating the scattering into two half-cylinders and averaging the sum of the contributions from each half-cylinder. The radius of the negative mirror-offset half-cylinder is  $r_{neg} = (r - r_0)$ , and the radius of the positive mirror-offset half-cylinder is  $r_{pos} = (r + r_0)$ . This is a conservative approximation, because it overstates the number of light rays at the smaller incident angles, as shown in figure 32; and the scattering is greater at smaller angles.

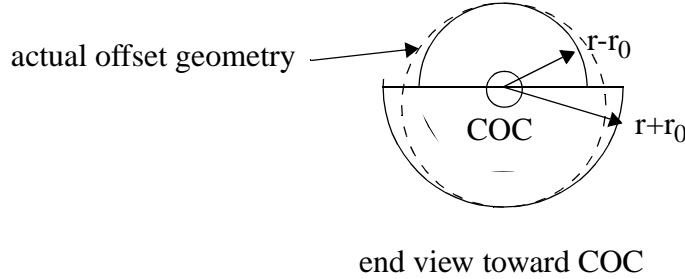


**Figure 32: Split geometry to approximate mirror offset effects**

Then the power scattered by a segment of wall which is subtended between the angles  $\theta_1$  and  $\theta_2$  is calculated by evaluating the integral.

$$P_s = P_{ac} \cdot A_{coc} \cdot BRDF_{wall} \cdot \Delta\Omega \cdot \frac{2\pi}{r^2} \cdot \int_{\theta_1}^{\theta_2} (2.53 \times 10^{-8} \cdot \theta^{-2.472})^2 \cdot \theta^3 d\theta$$

then

$$P_s = P_{ac} \cdot A_{coc} \cdot BRDF_{wall} \cdot \Delta\Omega \cdot \frac{2\pi}{r^2} \cdot \left( \frac{6.4 \times 10^{-16}}{0.944} \right) \cdot (\theta_1^{-0.944} - \theta_2^{-0.944})$$

The scattered power was calculated assuming the values below for the BRDF of the baffled beam tube and the unbaffled vacuum manifold walls, and the following parameters:

- 
1. Scattered Light and its Control in the LIGO Beam Tubes, Albert Lazzarini, LIGO Science Meeting Talk, 4/1/97



$$BRDF_{beamtube\,baffle} = 0.001\,sr^{-1}$$

$$BRDF_{manifold\,wall} = 0.1\,sr^{-1}$$

$$\Delta\Omega = 2.7 \times 10^{-10}\,sr$$

$$A_{COC} = 4.9 \times 10^{-2}\,m^2$$

$r = 0.91\,m, 0.62\,m$  , for large and small manifold respectively.

$$r_0 = 375\,mm$$

$$P_{ac} = 10 \times 10^3\,watt,$$

#### 5.2.4. Cryopump Surface Light Scattering

The cryopump surface inner lining, as shown in figure 33, can intercept scattered light from the ITM and ETM mirror surfaces at the near end of each beam tube, and the right-angle edge can retro-reflect back into the IFO. The retro-reflected cryopump light may exceed the LIGO

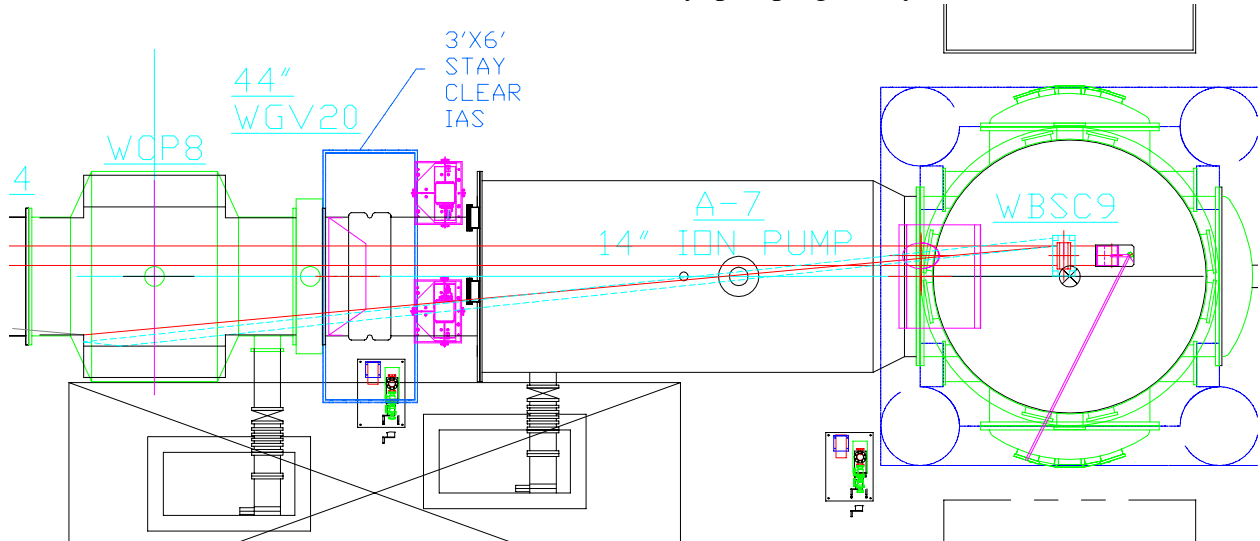


**Figure 33: Retro-reflection from cryopump baffle**

scattering requirements, as the calculations below will show, and *therefore baffles must be provided to hide the cryopump surfaces of CP2 and CP8 from the nearby COC. The far side of the cryopump does not need to be baffled, because the 1.13m inside diameter of the cryopump surface is occluded from the far end of the beam tube by the 1.06m inside diameter of the beam tube baffles.*

The cryopump lining may become coated with ice crystals or with areas of ice, so the BRDF of the surface is not predictable. However, a worst-case estimate of the scattering properties will be made by *assuming that the total integrated light which hits the inner surface of the cryopump will retro-reflect from the inside corner back to the COC which produced the incident light. Then the COC will re-scatter the retro-reflected light into the IFO solid angle.*

The differential power entering the IFO from this path can be calculated as follows,

$$dP_r = P_{ac} \cdot BRDF_{COC} \cdot d\Omega \cdot BRDF_{COC} \cdot \Delta\Omega;$$

and the total retroreflected power is obtained as before by integrating over the solid angle subtended by the cryopump surface.

$$P_r = P_{ac} \cdot \Delta\Omega \cdot 2\pi \cdot \left( \frac{6.4 \times 10^{-16}}{2.944} \right) \cdot (\theta_1^{-2.944} - \theta_2^{-2.944})$$

The results of the calculations are presented in “Summary of vacuum manifold and cryopump light scattering calculations” on page 37.

### 5.2.5. Summary of vacuum manifold and cryopump light scattering calculations

The results are presented in Table 4, “2K ITM Diffusely Scattered Power from Beam-tube and Vacuum Manifold Segments into IFO,” on page 38, and Table 5, “4K ETM Diffusely Scattered Power from Beam-tube and Vacuum Manifold Segments into IFO,” on page 39.

The scattered power from the 2K ITM should be interpreted as follows, referring to figure 30 and to the average scattered power column in Table 4 on page 38: the segment of wall from the mid station through the A-7A does not scatter; the 3m length of exposed wall included within the A-1C and the BE-4C scatters  $2.7\text{E-}22$  watts; the baffles in the beam tube scatter  $3.0 \times 10^{-21}$  watts;...etc. The unbaffled cryopump surfaces of CP2 may retroreflect  $2.5 \times 10^{-16}$ , which exceeds the initial LIGO requirement.

The scattered power from the 4K ITM should be interpreted in a similar manner, referring to figure 31 and to the average scattered power column in Table 5 on page 39: the 5m length of exposed wall included within the A-14A and the BE-4E scatters  $4.9 \times 10^{-22}$  watts; the baffles in the beam tube scatter  $3.1 \times 10^{-21}$ ;...etc. The unbaffled cryopump surfaces of CP8 may retroreflect  $1.7 \times 10^{-17}$ , which barely meets the initial LIGO requirement.

- *therefore baffles must be provided to hide the cryopump surfaces from the near ends of CP2 and CP8.*

**Table 4: 2K ITM Diffusely Scattered Power from Beam-tube and Vacuum Manifold Segments into IFO**

	$r-r_0$ , mirror offset negative		$r+r_0$ , mirror offset positive		average offset	
scattering distance from 2K ITM, m	scattered power per length interval, watt	scattering angle, negative- mirror offset, rad	scattered power per length interval, watt	scattering angle, positive- mirror offset, rad	average scattered power, watt	description
2000		1.220E-04		4.970E-04		mid station
1992	0.00E+00	1.225E-04	0.00E+00	4.991E-04	0.00E+00	3m length of 1.2 ID tubing (A-1C, BE-4C)
1989	4.30E-22	1.227E-04	1.14E-22	4.997E-04	2.72E-22	end 2000m beam tube
37	4.77E-21	4.235E-03	1.28E-21	2.473E-02	3.03E-21	begin 2000m beam tube
37	0.00E+00	6.667E-03	0.00E+00	2.716E-02	0.00E+00	end 1.2 ID tube
35	4.31E-22	7.052E-03	1.15E-22	2.873E-02	2.73E-22	2m length 1.2 ID tub- ing (BE-4A)
30	0.00E+00	8.106E-03	0.00E+00	3.302E-02	0.00E+00	end of CP2
28	4.84E-16	8.683E-03	7.75E-18	3.537E-02	2.46E-16	begin CP2
28	0.00E+00	8.683E-03	0.00E+00	3.537E-02	0.00E+00	end transition tube
7.6	2.57E-21	7.099E-02	6.11E-22	1.697E-01	1.59E-21	1.8 ID transition tube (B-9A, BE-5A, B-1a, B-8A)
		<b>total</b>			<b>2.46E-16</b>	
		<b>initial LIGO requirement<sup>a</sup></b>			<b>1.50E-17</b>	
		<b>enhanced LIGO requirement<sup>b</sup></b>			<b>1.50E-21</b>	

a. See the requirement for diffuse scattered light from ETM and ITM, Table 1 on page 11.

b. The enhanced LIGO requirement for strain amplitude density is a factor 1E-2 lower than the initial LIGO requirement (Ref. SRD, LIGO-E950018-02-E); so the strain power density requirement is a factor 1E-4 lower. Therefore the enhanced LIGO noise power requirement will also be a factor 1E-4 lower.

**Table 5: 4K ETM Diffusely Scattered Power from Beam-tube and Vacuum Manifold Segments into IFO**

scattering distance from 4K ETM, m	$r-r_0$ , mirror offset negative		$r+r_0$ , mirror offset positive		average offset	description of scattering location
	scattered power per length interval, watt	scattering angle, negative-mirror offset, rad	scattered power per length interval, watt	scattering angle, positive-mirror offset, rad	average scattered power, watt	
2000		1.220E-04		4.970E-04		mid station
1992	0.00E+00	1.225E-04	0.00E+00	4.991E-04	0.00E+00	5m length of 1.2 tubing (A-14A, BE-4E)
1987	7.75E-22	1.228E-04	2.06E-22	5.003E-04	4.90E-22	end 2000m beam tube
11.5	4.88E-21	1.348E-02	1.30E-21	7.870E-02	3.09E-21	begin 2000m beam tube
11.5	0.00E+00	2.122E-02	0.00E+00	8.643E-02	0.00E+00	end 1.0 tube
10.0	3.46E-22	2.440E-02	9.19E-23	9.940E-02	2.19E-22	end CP8
8.8	3.23E-17	2.773E-02	5.18E-19	1.130E-01	1.64E-17	begin CP8
7.3	3.52E-22	3.342E-02	9.34E-23	1.362E-01	2.22E-22	1.5m length 1.0 tubing (A-1E)
7.3	0.00E+00	3.342E-02	0.00E+00	1.362E-01	0.00E+00	end transition tube
5.0	5.59E-22	1.079E-01	1.00E-22	2.579E-01	3.30E-22	1.8 ID transition tube (A-7C)
		<b>total</b>			<b>1.64E-17</b>	
		<b>initial LIGO requirement<sup>a</sup></b>			<b>1.50E-17</b>	
		<b>enhanced LIGO requirement<sup>b</sup></b>			<b>1.50E-21</b>	

a. See the requirement for diffuse scattered light from ETM and ITM, Table 1 on page 11.

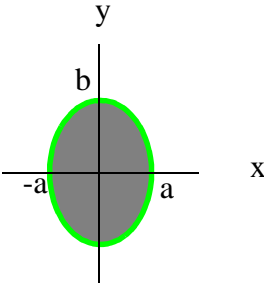
b. The enhanced LIGO requirement for strain amplitude density is a factor 1E-2 lower than the initial LIGO requirement (Ref. SRD, LIGO-E950018-02-E); so the strain power density requirement is a factor 1E-4 lower. Therefore the enhanced LIGO noise power requirement will also be a factor 1E-4 lower.

### 5.3. COC Elliptical Baffles for Recycling Cavity

A portion of the main beam in the recycling cavity will spill over the periphery of the 250 mm diameter BS, which is tipped at 45 deg to the beam axis. The main beam is displaced by 7.8 mm as it passes through the BS. The input beam will be shifted by half this amount so that the displacement is shared on both sides, then the BS presents an elliptical cross-section to the main beam with a semi-major axis of 125 mm and a semi-minor axis of 80.6 mm.

The fraction of the total power which hits the BS mirror is calculated by integrating the normalized intensity of the Gaussian profile laser beam across the elliptical cross-section of the mirror.

$$I(x,y) := \frac{2 \cdot e^{-2 \cdot \left( \frac{x^2 + y^2}{w^2} \right)}}{\pi \cdot w^2}$$

$$f_M := \frac{2}{\pi \cdot w^2} \int_{-a}^a \int_0^{\sqrt{1 - \frac{x^2}{a^2}}} 2 \cdot e^{-2 \cdot \frac{y^2}{w^2}} dy \cdot e^{-2 \cdot \frac{x^2}{w^2}} dx$$


where  $a$  is the semi-minor axis, and  $b$  is the semi-major axis of the elliptical cross-section.

### 5.3.1. Glint Power into the IFO from the Light Spilling Around the BS Mirror

A fraction of the power that spills over the sides of the BS may hit the walls of the vacuum enclosure and cause a glint back into the IFO.

$$P_g = P_{ann} \cdot \frac{2R\lambda}{\pi^2 w^2} \eta_{glint}$$

### 5.3.2. Power Scattered from the Elliptical Baffle into IFO

The power spilling over the BS mirror will be blocked with an isolated elliptical baffle mounted to the LOS structure. However, the baffle itself will scatter a lesser amount of power into the IFO.

$$P_s = P_{BS} \cdot BRDF \cdot \Delta\Omega \cdot A_{SEI},$$

where the scattered power has been effectively reduced by the seismic attenuation factor,  $A_{SEI}$ .

The elliptical baffle also causes edge diffraction into the IFO, but the seismic isolation factor reduces the effective diffracted light to a safe level, as shown in Table 6 on page 41. See “Edge Diffraction from COC Baffle Aperture” on page 100.

### 5.3.3. Summary of Elliptical Baffle Calculations

The glint and scattered power from the light spilling around the BS may exceed the scattering requirements, as shown in Table 6 on page 41, and *must be caught with seismically isolated baffles*.

**Table 6: Summary of Light Spilling Around BS**

<i>Parameter</i>	<i>4K</i>	<i>2K</i>
power in the recycling cavity, watt	300	300
beam parameter, w, mm	36.3	26.9
BRDF of elliptical baffle, sr <sup>-1</sup>	0.01	0.01
IFO solid angle, sr	$2.7 \times 10^{-10}$	$2.7 \times 10^{-10}$
seismic isolation factor	$3.6 \times 10^{-9}$	$3.6 \times 10^{-9}$
semi-major axis, b, mm	125	125
semi-minor axis, a, mm	80.6	80.6
fractional power spilled around BS, watt	$1.19 \times 10^{-5}$	$2.73 \times 10^{-9}$
power spilling toward RM, watt	$1.79 \times 10^{-3}$	$4.1 \times 10^{-7}$
power spilling toward ITMx, watt	$3.57 \times 10^{-3}$	$8.2 \times 10^{-7}$
power spilling toward AP, watt	$1.79 \times 10^{-3}$	$4.1 \times 10^{-7}$
glint power, RM beam, watt	$4.4 \times 10^{-12}$	$1.8 \times 10^{-15}$
glint power, ITMx beam, watt	$8.8 \times 10^{-12}$	$3.7 \times 10^{-15}$
glint power, AP beam, watt	$4.4 \times 10^{-12}$	$1.8 \times 10^{-15}$
total glint power, all beams, watt	$1.8 \times 10^{-11}$	$7.3 \times 10^{-15}$
total scattered power from wall, watt	$1.9 \times 10^{-14}$	$4.4 \times 10^{-18}$
total scattered power from isolated elliptical baffles, watt	$6.9 \times 10^{-23}$	$1.6 \times 10^{-26}$
edge diffraction from isolated elliptical baffle, watt	$2.8 \times 10^{-28}$	$1.8 \times 10^{-36}$
scattered light requirement per path, watt	$3.3 \times 10^{-13}$	$3.3 \times 10^{-13}$

Elliptical baffles which match the apparent elliptical cross-section of the 45 degree BS will be placed in front of the RM, ITMx, and ITMy, as shown in figure 34; so that the glint does not exceed the scattering requirements.

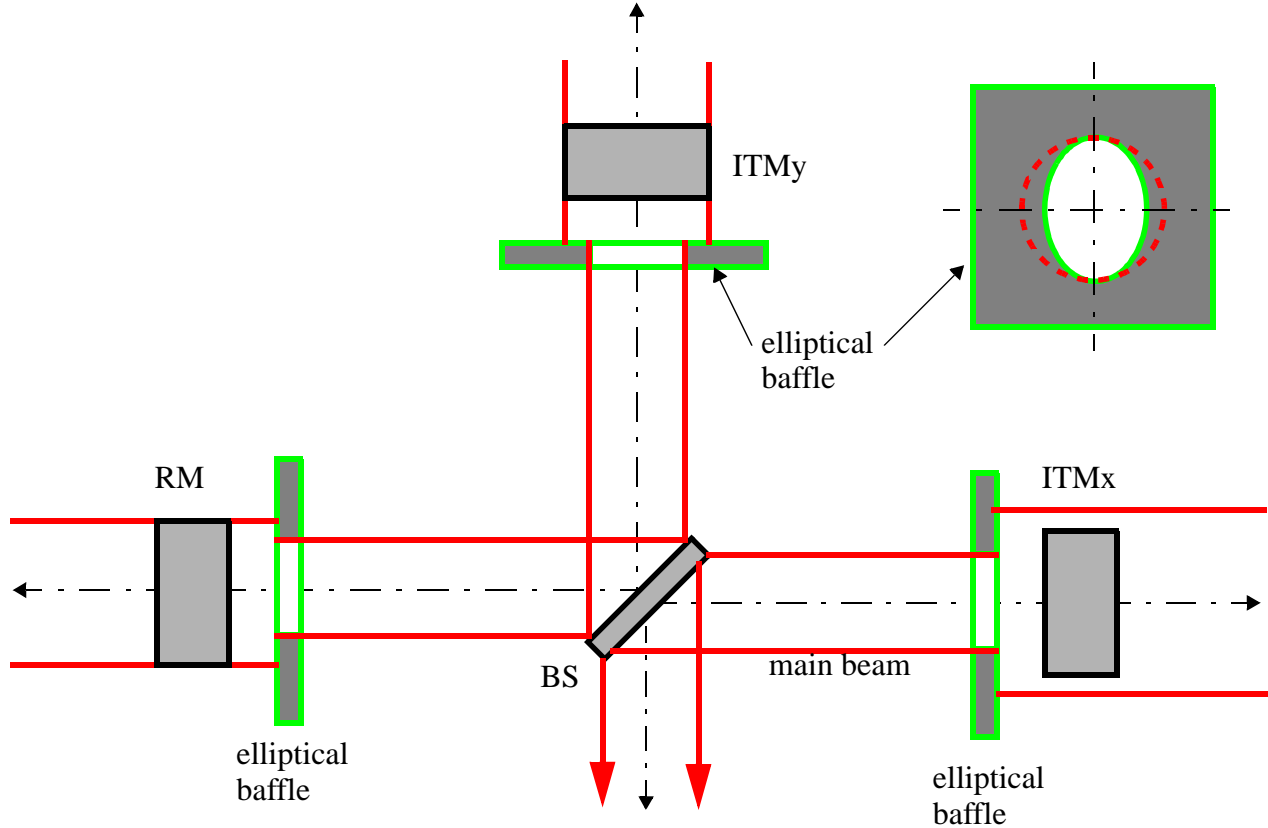


**Figure 34: Elliptical baffles for RM, ITMx, and ITMy**

## 5.4. Mode-cleaner Baffles

The scattered light from the mode-cleaner mirrors will eventually spill around each of the mirrors in the form of an annular beam. These three annular beams may hit a chamber wall and cause a glint or scatter into the IFO beam. The annular beams around mirrors MC1 and MC2 can be caught at the source by mounting baffles to the outside of the SOS structures which support the mode-cleaner mirrors. The baffle at MC1 contains an aperture for passage of the pick-off beam from the mode-cleaner, as shown in figure 35. Part of the annular beam around MC3 will pass through the mode matching telescope (not shown) and be caught by the COC baffle in front of the RM.

The light power scattered back into the mode-cleaner from a surface with an amplitude attenuation factor  $A$  is given by

$$P_s = P_i BRDF \Delta \Omega_{mc} A.$$

The requirement for the maximum light amplitude scattered back into the mode-cleaner will be taken to be the same relative scattered light amplitude allowed into the recycling cavity through the RM,

$$P_s)_{REQRM} = 5.8 \times 10^{-13} \text{ watt.}$$

Then the requirement for scattered light power into the mode-cleaner which enters the IFO through the RM is,

$$P_s)_{REQmodecleaner} = \frac{9300}{6} 5.8 \times 10^{-13} = 9.0 \times 10^{-10} \text{ watt.}$$

A summary of the scattered light calculations for the mode-cleaner is presented in Table 7 on page 44. Neither the glint power of the scattered light nor scattering from the surfaces of the vacuum housing back into the mode-cleaner exceed the scattering requirement. *Therefore baffles are not required.*

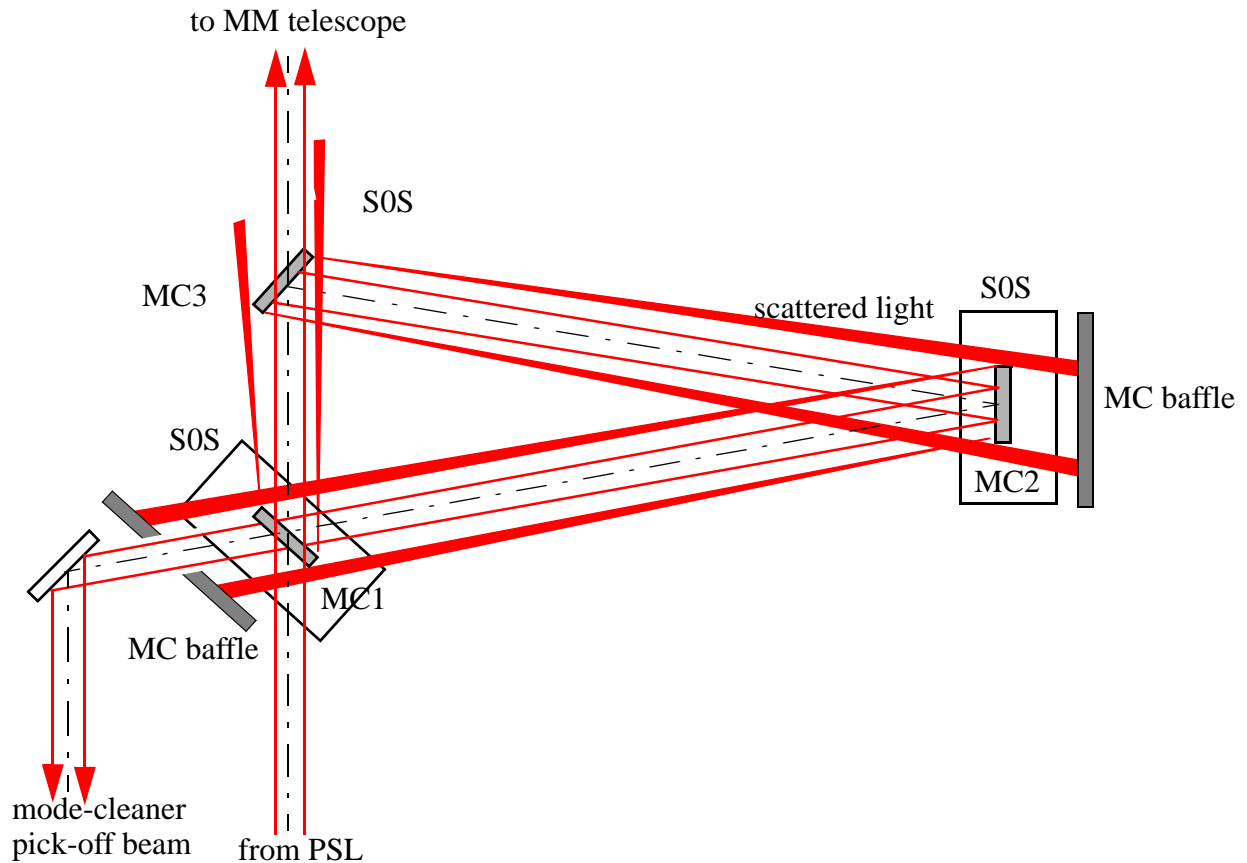


**Figure 35: Mode-cleaner baffles, mounted to SOS structure**



However because of the inordinately large amount of power scattered from the mode-cleaner, *baffles may be mounted on the SOS structure to catch the scattered light from the mode-cleaner mirrors.*

**Table 7: Summary of Light Scattered from Mode-cleaner Mirrors**

<i>Parameter</i>	<i>4K</i>	<i>2K</i>
power in the mode-cleaner cavity, watt	9300	9300
beam parameter, w, mm	2.0	2.0
BRDF of baffle, sr <sup>-1</sup>	0.01	0.01
mode-cleaner solid angle, sr	$8.3 \times 10^{-8}$	$8.3 \times 10^{-8}$
seismic isolation factor	$3.6 \times 10^{-9}$	$3.6 \times 10^{-9}$
power spilling around mode-cleaner mirrors, watt	0.27	0.27
glint power back into mode-cleaner, watt	$2.6 \times 10^{-13}$	$2.6 \times 10^{-13}$
scattered power from chamber wall, watt	$2.2 \times 10^{-10}$	$2.2 \times 10^{-10}$
effective scattered power from isolated baffles, watt	$8.1 \times 10^{-19}$	$8.1 \times 10^{-19}$
scattered light requirement, watt	$9.0 \times 10^{-10}$	$9.0 \times 10^{-10}$

## 6 VERTEX (ITM, BS, AND APS) PO BEAM OPTICAL TRAIN

The ITM and BS PO beam optical trains consist of a pick-off mirror, an 8X demagnification PO telescope, a series of steering mirrors, an output vacuum window, and a 3.1X demagnification ISC telescope mounted outside the vacuum on the ISC table. After the ISC telescope the PO beams are directed into the Guoy phase telescope of the WFS. The APS PO beam does not contain a pick-off mirror but has the addition of a Faraday isolator and a half wave retardation, polarization rotator on the SEI platform.

### 6.1. Wavefront Aberrations in the PO Beam Optical Train

The effect of aberrations on the WFS signal was analyzed by using amplitude and phase maps of the carrier and sideband spots generated by the coherent optical modeling program ASAP, as described in *Effect of PO Telescope Aberrations on Wavefront Sensor Performance*, LIGO-T980007-00-D. A summary of these results is presented in the appendix. See “The effect of opti-

cal aberrations on the Wavefront sensor signal” on page 75. The acceptance criteria for determining the allowed aberrations are that the contrast ratios between pure tilt and pure displacement of the IFO carrier beam would be >5:1 for both the tilt sensor and the displacement sensors. The individual optical element aberrations can be inferred from the ASAP WFS model.

The aberration specifications for the entire ITM, APS and BS PO beam optical trains are shown in Table 8 on page 45. They were inferred from the ASAP Geometrical WFS model, and therefore meet the signal contrast requirements for the WFS. The ETM PO beam is not used for wavefront sensing, so the aberrations are relatively unimportant. A much cheaper on-axis folded refractive telescope is proposed for the ETM PO beam, with twice as much allowed p-v aberration.

**Table 8: Aberration Specifications on the 1.3m PO Beam Optical Train**

<i>Optical element</i>	<i>Maximum aberration, p-v @ 0.6328 micron</i>	<i>Comment</i>
pick-off mirror	0.25	
ITM, APS and BS PO telescope, primary mirror	0.25	
ITM, APS and BS PO telescope, secondary mirror	0.25	
ETM PO telescope, objective	0.50	
ETM PO telescope, eyepiece	0.50	
Faraday Isolator	0.5	includes glass rotator and two polarizers
isolator windows (2 required)	0.2	per each
half wave retarder (if needed)	0.2	
accessory fold mirrors (7 required)	0.1	per each
output window	0.2	
ISC Telescope, objective	0.1	
ISC Telescope, eyepiece	0.1	
Guoy 1st lens	0.1	
Guoy 2nd lens	0.1	

## 6.2. Image Distortion and Polarization Rotation of the PO Beams

Image rotation will occur within the PO beam optical train because of out-of-plane reflections and compound wedge angles of the BS. Provided there are no strong prefigurement effects in the coatings of the PO mirrors, the polarization rotation will follow the image rotation.

The image rotation of the ITM PO beam at the output of the PO telescope is approximately 4 deg, and this orientation will be maintained out to the ISC table. The image also has some amount of anamorphicity due to the wedge of the ITM mirror. The image rotation of the BS PO beam at the

output of the PO telescope is approximately 1 deg, and this orientation will be maintained out to the ISC table. The image of the APS beam is < 1deg. The Faraday isolator will rotate the plane of polarization by 45, and a following half-wave plate will rotate the plane of polarization back to vertical. The orientation of the image and the polarization will be maintained out to the ISC table.

### 6.3. Vertex PO Telescope and ISC Telescope

#### 6.3.1. Mechanical Specifications of the ITM, BS, APS PO Telescope and ISC Telescope

The mechanical specifications for the PO beam reducing telescopes are shown in Table 9 on page 46.

**Table 9: Specifications for Vertex PO Beam Optical Train Reducing Telescopes**

<i>Property</i>	<i>Value</i>	<i>Comment</i>
<i>PO beam telescope: ITM, BS, and APS</i>		
configuration	off-axis parabolic	
input clear aperture diameter	173 mm	@ 100 ppm beam power diameter
input FOV	$\pm 5.5 \times 10^{-4}$ rad	due to initial alignment error
output clear aperture diameter	22 mm	
Internal resonance and Q	TBD	
demagnification ratio	8X	
<i>ISC beam telescope</i>		
configuration	on-axis refractive	
input clear aperture diameter	46 mm	
input FOV	$\pm 4.4 \times 10^{-3}$ rad	due to initial alignment error
output clear aperture diameter	13 mm	
demagnification ratio	3.1X	

A schematic layout of the optical elements in the PO telescope are shown in figure 36.

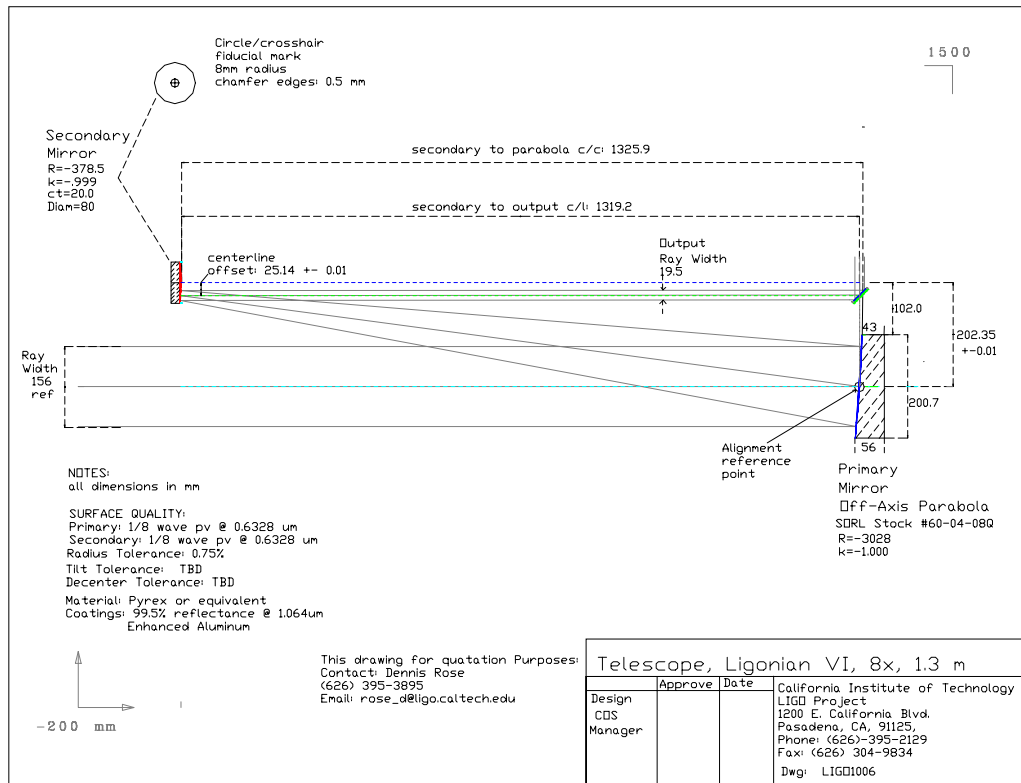


**Figure 36: PO Beam Reducing Telescope**

## 6.3.2. PO Telescope Mounting Structure

### 6.3.2.1 PO Telescope Assembly

The PO telescope assembly consists of a rigid outer housing made up of a bottom plate, two sides, an end, and a top plate; onto which are mounted the optical mounts which hold the optical elements. The top plate forms a rigid tubular assembly so that internal resonances do not add excessive thermal noise to the SEI platform. See “Thermal Noise Contribution to SEI Platform Motion from PO Telescope and PO Mirrors” on page 89.

The PO telescope assembly is mounted to a pivot yoke, which provides azimuth and elevation alignment, with the pivot point located at the optical center of the objective mirror of the telescope. The height of the pivot point above the SEI platform is adjustable by moving the vertical sides of the pivot yoke. A support bracket at the entrance end of the telescope rigidly supports the telescope above the SEI platform at the aligned elevation angle. A preliminary design concept of the telescope and the mounting yoke are shown in figure 37.

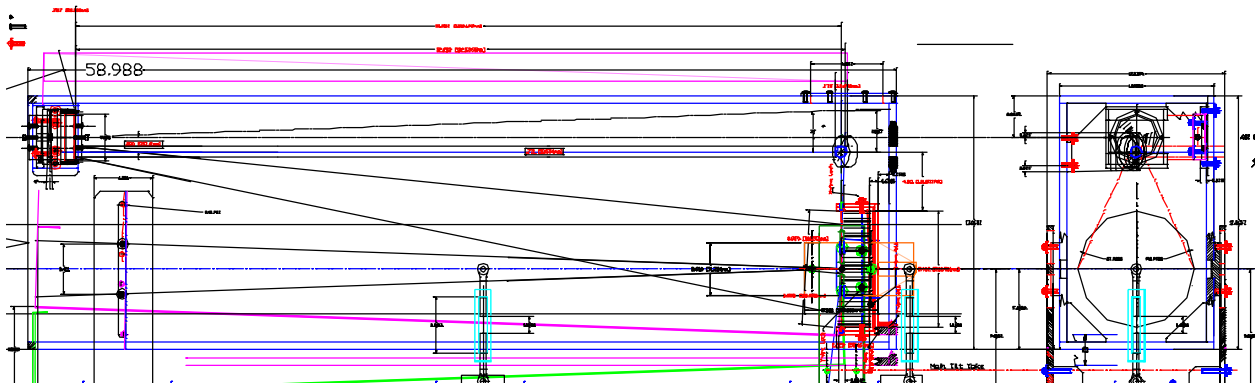


Figure 37: Preliminary design concept of the PO telescope with pivot yoke

The overall weight of the structure is reduced while maintaining stiffness, by reducing the thickness of the housing plates in a truss pattern, as shown in figure 38.

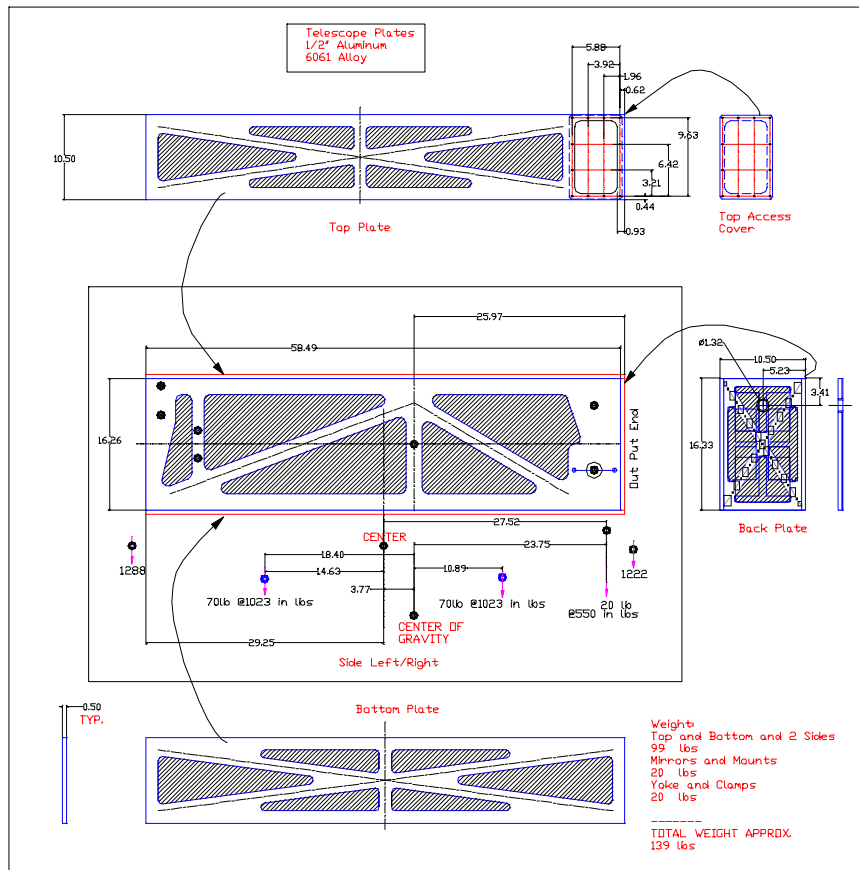


Figure 38: Preliminary design of the PO telescope housing with a thinning truss pattern for weight reduction

### 6.3.3. Thermal Noise Amplitude at Test Mass Due to Telescope Assembly

## Mounted on SEI Platform

An estimate of the resonant frequency of the telescope assembly was calculated-- see “Thermal Noise Contribution to SEI Platform Motion from PO Telescope and PO Mirrors” on page 89--and the results are shown in Table 10 on page 49.

**Table 10: Summary of Thermal Noise Characteristics for Telescope Assembly**

<i>Characteristic</i>	<i>Value</i>	<i>Requirement</i>
Resonant frequency	80 Hz	
@ Q	300	
rms noise amplitude	$2.5 \times 10^{-21} \text{ m}/\sqrt{\text{Hz}}$	$< 1 \times 10^{-20} \text{ m}/\sqrt{\text{Hz}}$

## 6.4. ETM PO Telescope

TBD

**Table 11: Specifications for ETM PO Beam Optical Train Reducing Telescopes**

<i>Property</i>	<i>Value</i>	<i>Comment</i>
<i>PO beam telescope: ETM</i>		
configuration	on-axis refractive	
input clear aperture diameter	173 mm	ETM:@ TBD ppm
input FOV	$\pm 5.5 \times 10^{-4} \text{ rad}$	due to initial alignment error
output clear aperture diameter	22 mm	
Internal resonance and Q	TBD	
demagnification ratio	8X	

## 6.5. PO mirror

### 6.5.1. PO Mirror Specification

The specifications for the BS and ITM PO mirrors are listed in Table 12 on page 50.

**Table 12: PO Mirror Specifications**

<i>parameter</i>	<i>BS</i>	<i>ITM</i>
surface flatness	$<\lambda/8$ , @ 632.8nm	$<\lambda/8$ , @ 632.8nm
clear aperture	>156 mm, normal incidence	>156 mm, @ 45 deg incidence, elliptical shape
thickness	20 mm	20 mm
reflectivity	>99%, @ normal incidence, 1060nm	>99%, @ 45 deg incidence, 1060nm, p polarization

### 6.5.2. PO Mirror Mount

A schematic view of the PO mirror mount is shown in figure 39. The height below the SEI platform is adjustable with the sliding vertical mirror bracket. Azimuth adjustment is provided by the oversized mounting holes on the base plate. Elevation adjustment is provided by the kinematic tilt mechanism on the mirror mount. The vernier adjustment screws provide a temporary means for making fine adjustments of the mirror position and tilt. After the adjustments are completed the mirror assembly is rigidly locked in place with the mounting screws. A preliminary mechanical layout with plan and elevation views is shown in figure 40. The PO mirror mounts use oversized mounting holes and shims to provide displacement and tilt alignment.

The internal resonances of the mirror assembly have been estimated-- see "Thermal Noise Contribution to SEI Platform Motion from PO Telescope and PO Mirrors" on page 91-- and the thermal noise induced onto the SEI platform is not excessive, as shown in Table 13 on page 52.

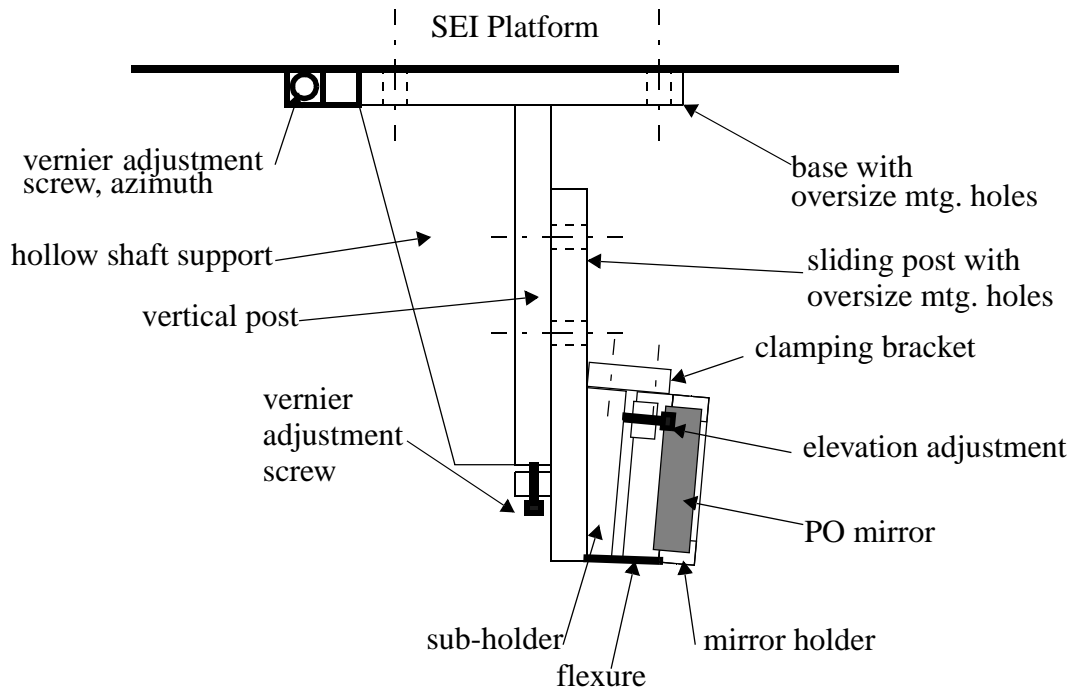


**Figure 39: Schematic Drawing of the PO Mirror in Its Mount**

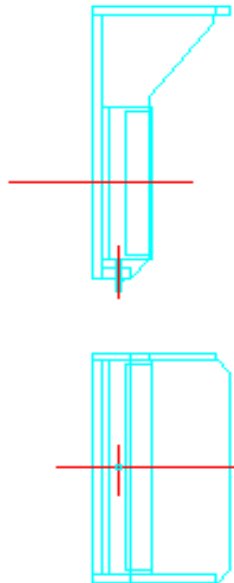


**Figure 40: Preliminary mechanical layout of PO mirror assembly**



### 6.5.3. Thermal Noise Amplitude at Test Mass Due to PO Mirror Assembly

**Table 13: Summary of Thermal Noise Characteristics for PO Mirror Assembly**

<i>Characteristic</i>	<i>Value</i>	<i>Requirement</i>
Resonant frequency	258 Hz	
@ Q	300	
rms noise amplitude	$1.9 \times 10^{-22} \text{ m}/\sqrt{\text{Hz}}$	$< 1 \times 10^{-20} \text{ m}/\sqrt{\text{Hz}}$

## 6.6. Output Vacuum Window

### 6.6.1. Output Window Specification

#### 6.6.1.1 Surface Figure

The surface figure of the window will cause a slight aberration in the wavefront of the PO beam. The ASAP WFS model indicated that a wavefront aberration of  $< 0.225\lambda$  was acceptable. A calculation of the pressure induced bowing of the vacuum window also indicated a negligible wavefront distortion with a 3in diameter by 0.25 in thick window.

#### 6.6.1.2 Surface Scattering

The BRDF of the vacuum window will be  $< 0.001 \text{ sr}^{-1}$  in order to meet the  $< 0.065 \text{ sr}^{-1}$  scattering requirement for a 9mm Gaussian beam diameter beam.

#### 6.6.1.3 Specifications for the Vacuum Windows

The specifications for the Vacuum windows are summarized below. The surface figure will be specified at HeNe wavelength.

**Table 14: Specification for PO Beam Vacuum Window**

<i>Property</i>	<i>Value</i>
material	fused silica
thickness	TBD
substrate diameter	TBD
wedge	$34^\circ \pm 5'$
clear aperture	$>30 \text{ mm}$ , includes 13 mm to allow for initial alignment and long-term drift

**Table 14: Specification for PO Beam Vacuum Window**

<i>Property</i>	<i>Value</i>
wavefront distortion	$\lambda/8$ @ 632.8nm, over any 22 mm diameter within the clear aperture
AR coating, both surfaces	<.001 @1064 nm, @ normal incidence angle
BRDF <sub>wo</sub>	< $1 \times 10^{-3}$ sr <sup>-1</sup> @ 5deg incidence TBD
Vacuum properties	Vacuum Equipment Specification, LIGO-E940002-02-V

## 6.6.2. Output Window Mount

### 6.6.2.1 Conflat Flange Mount

The output window will be mounted in a modified conflat flange, similar to the mounting configuration of the window in the 40 meter mode cleaner. Ref: LIGO Dwg. 1205030.

### 6.6.2.2 Differential Pressure Distortion of the Window

The differential pressure due to the vacuum interface at the window will cause a distortion at normal incidence of 0.3nm for a 3.0 in diameter by 0.22 in thickness window<sup>1</sup>. This causes a negligible optical path difference and will not significantly affect the wavefront curvature.

## 6.7. Faraday Isolator

A vacuum enclosure may be needed to allow the Faraday isolator to be used in the IFO vacuum. The windows will be tipped slightly to avoid direct reflections into the IFO. They will be sealed to the housing with viton o-rings. The wavefront distortion specifications for the Faraday isolator assembly, and the windows are described in Table 3 on page 40. The surface scattering specifications for each surface are BRDF  $< 1 \times 10^{-4}$ .

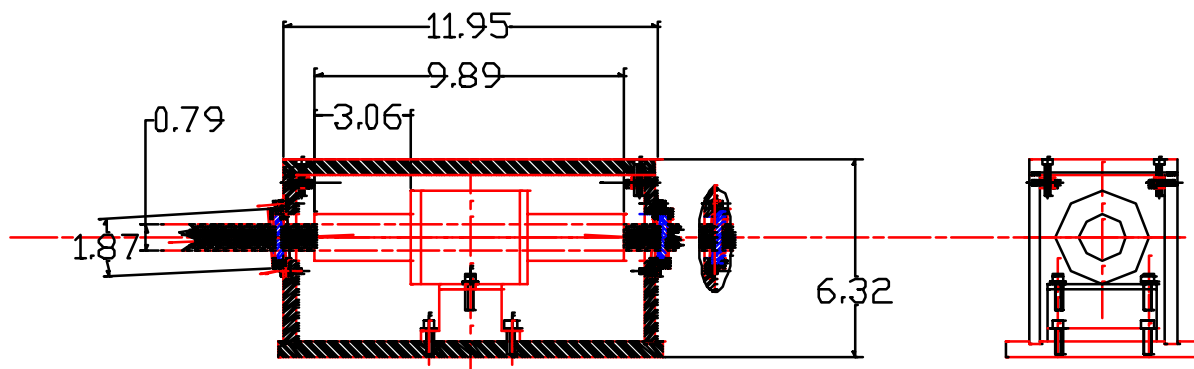


**Figure 41: Preliminary layout of Faraday isolator inside its vacuum housing.**

1. Calculation by Dennis Coyne, 6/3/97

## 7 OPTICAL ALIGNMENT OF COS ELEMENTS

### 7.1. Alignment of beam-dumps and baffles

Alignment of the beam-dumps and baffles will be accomplished visually, or with enhanced viewing devices, by viewing the locations of the ghost beams generated by the COS alignment autocollimator. The beam-dumps and baffles will be mounted to a reference bracket so they may be removed and subsequently replaced in the same position without requiring realignment, to facilitate the initial alignment of the IFO.

### 7.2. Alignment of PO Beam Telescope

#### 7.2.1. Telescope pre-alignment

The PO telescopes will be pre-aligned on an optical fixture using apertures and an infrared interferometer.

### 7.3. Final alignment

#### 7.3.1. Special alignment equipment

Special alignment equipment will consist of the following:

- laser autocollimator, 670 nm wavelength 50-100 mw
- Mylar centering reticles for COC
- Mylar centering reticles for telescope
- TV video caliper system

#### 7.3.2. Alignment procedure

The alignment of the PO mirrors and PO beam telescopes will be accomplished with the aid of a high power visible autocollimator (50 mW), following the initial alignment of the COC by ISC. Preliminary reflectance data from REO for the COC HR and AR coatings at 675 nm are shown in Table 15 on page 54.

**Table 15: Reflectivity of COC surfaces @ 675 nm wavelength**

<i>COC surface</i>	<i>Reflectivity @ 675 nm</i>	<i>Polarization</i>
ITM AR	0.4	p-polarization
ITM HR	0.15	p-polarization

**Table 15: Reflectivity of COC surfaces @ 675 nm wavelength**

<i>COC surface</i>	<i>Reflectivity @ 675 nm</i>	<i>Polarization</i>
BS AR	0.2	p-polarization
BS HR	0.1	p-polarization
ETM AR	0.4	p-polarization
ETM HR	0.1	p-polarization

The expected powers of the various ghost beams, based on these reflectivities are shown in Table 16 on page 55.

**Table 16: Ghost Beam Power, Assuming 15% Reflectivity on Both COC Surfaces**

<i>ITM Ghost Beam</i>	<i>Power, W</i>	<i>Location</i>
Autocollimator output	0.050	HAM3
main x-beam	1.56E-03	HAM4
ITM <sub>x</sub> PO	1.94E-03	HAM4
GBITM <sub>x</sub> AR1	1.44E-02	beam dump BSC2
GBITM <sub>x</sub> AR4	1.17E-04	beam dump BSC2
GBITM <sub>x</sub> HR3	1.10E-03	beam dump BSC7
GBITM <sub>x</sub> HR4	6.61E-05	beam dump BSC7
GBBSAR3 <sub>x</sub>	7.20E-04	beam dump BSC3
GBBSHR3 <sub>y</sub>	1.44E-04	beam dump BSC1
GBBSAR1 <sub>y</sub> '	3.89E-04	beam dump HAM4
GBBSAR3 <sub>y</sub> '	1.56E-04	beam dump HAM4
GBBSHR3 <sub>x</sub> '	2.80E-05	beam dump HAM4
BS PO	8.10E-03	HAM4
main y-beam	1.94E-04	HAM4
ITM <sub>y</sub> PO	2.70E-04	HAM3
GBITM <sub>y</sub> AR1	2.00E-03	beam dump BSC2
GBITM <sub>y</sub> AR4	1.62E-05	beam dump BSC2
GBITM <sub>y</sub> HR3	1.53E-04	beam dump BSC8

A schematic layout of the alignment set-up is shown in figure 42. The autocollimator, mounted to a tripod outside the HAM4 chamber, will reflect from a turning mirror mounted to the SEI optics platform along the axis of the IFO. The autocollimator beam will be aligned perpendicular to the HR surface of the ITM. The centering of the autocollimator on the ITM will be accomplished by scattering the autocollimator beam from a precision Mylar reticle referenced to the ITM center-line and mounted to the SUS cage. The position of the centroid of the autocollimator beam will be imaged and measured with a commercial video caliper system.

The ghost beams generated by the autocollimator beam will be used to align the PO beams through the telescopes and through the vacuum window. The ghost beams will also be used to visually align the beam-dumps and the apertures of the stray light baffles for the ITM and ETM.

The deviation angles of the PO beams at 670nm wavelength are estimated to be  $< 4 \times 10^{-5}$  rad greater than at 1060nm because of the variation in index of refraction of the fused silica COC. This will result in a maximum displacement of  $< 1$ mm at the PO telescope entrance aperture. The increase in deviation angles of the second order ghost beams at 670nm wavelength are estimated

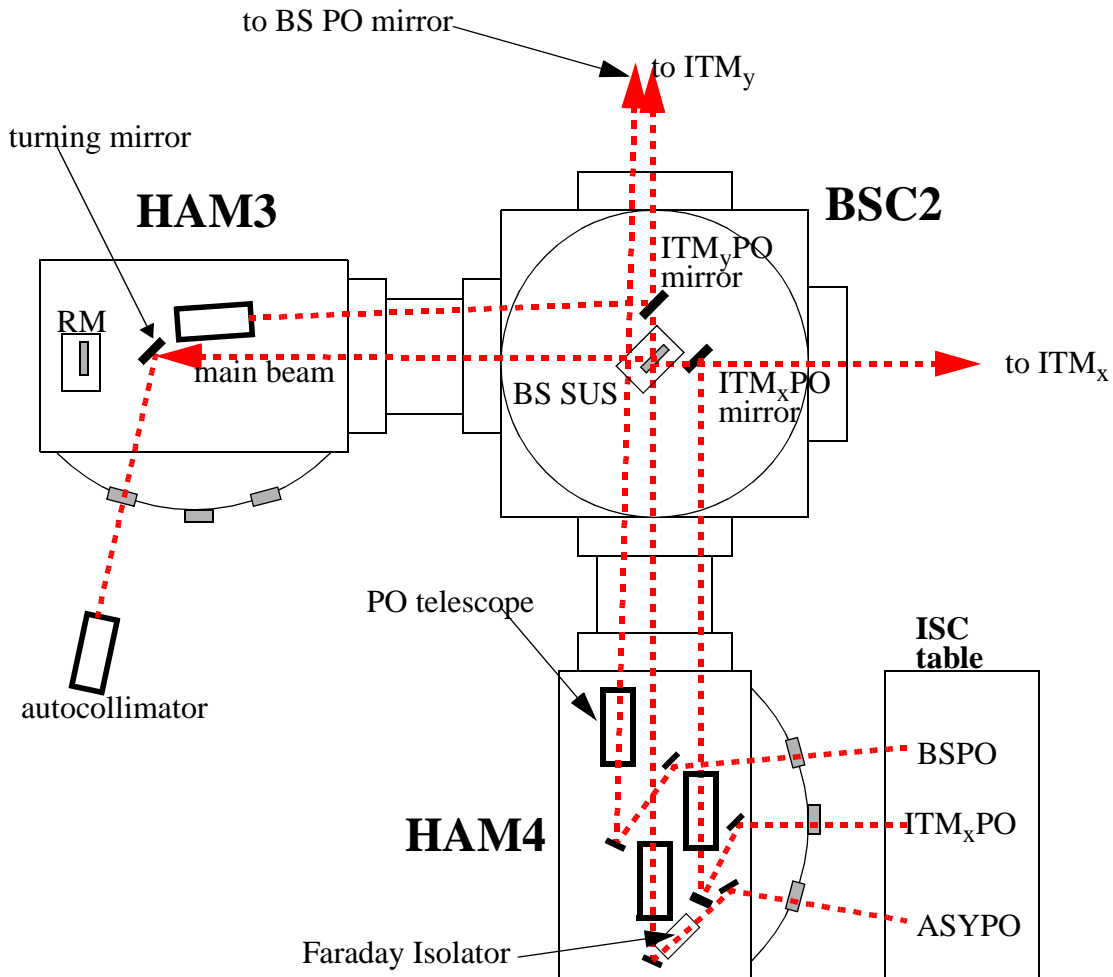


**Figure 42: Alignment Procedure for COS**

to be  $< 8 \times 10^{-5}$  rad, with a maximum beam displacement of  $< 1$  mm at the beam-dump aperture. These errors, combined with the expected initial alignment errors described in Table 17 on page 57, will be tolerated within the allowed field-of-view of the telescopes and no corrections will be made to the alignments based on 670 nm wavelength.

### 7.3.3. PO Beam Initial Alignment Error

- ISC will provide the initial alignment of the COC to a limited accuracy. The initial alignment of the ITM mirror will be further degraded by the shift of the BSC SEI platform during pump-down. The following estimates are taken from the ASC P D D, and IAS FDR.
- initial ISC alignment accuracy of ITM<sup>1</sup>  $\Delta\theta_i = \pm 0.8 \times 10^{-4}$  rad
- PO mirror shift during pump-down<sup>2</sup>  $\Delta\theta_p = \pm 1 \times 10^{-4}$  rad,
- telescope shift during pump-down<sup>3</sup>  $\Delta\theta_t = \pm 1 \times 10^{-4}$  rad
- initial displacement error of COS autocollimator centerline, 3 mm (estimate)

The angular alignment errors of the PO mirrors, and the optical lever arms to the telescopes will result in angle and displacement errors of the telescope input and output beams. The BS PO and ITM PO mirrors are approximately 9 m distance from the telescope. The telescope output beam angle error will be magnified approximately 10 times, and the output displacement error is demagnified by 0.1. The telescope output beam errors will cause beam displacement and a tilt angle errors at the output window, approximately 1 m away; and at the ISC table, approximately 2.5 m away. A summary of the initial PO beam alignment errors is presented in Table 17 on page 57. The PO beams are likely to shift by the amount shown after initial IFO lock is acquired.

**Table 17: PO Beam Initial Alignment Errors**

<i>Location</i>	$\Delta\theta$ , rad	$\Delta x$ , mm
telescope input	$\pm 4 \times 10^{-4}$	$\pm 6$
telescope output	$\pm 4 \times 10^{-3}$	$\pm 0.6$
output window	$\pm 4 \times 10^{-3}$	$\pm 6$
ISC table	$\pm 4 \times 10^{-3}$	$\pm 13$

### 7.3.4. PO Beam Long-term Drift Alignment Error

The HAM and BSC SEI platforms will shift due to long-term settling of the viton stack elements, and other possible creep mechanisms. It will be assumed that the maximum angular drift of the

---

1. ASC PDR LIGO T970060-00-D, p7, 11

2. SEI platform will shift during initial pump-down, private communication Dennis Coyne

3. SEI platform will shift during initial pump-down, private communication Dennis Coyne

SEI stack between corrections is  $\pm 0.5 \times 10^{-4}$ . The tilt of the PO mirror will result in an input angle and displacement error at the input of the telescope. The additional tilt of the telescope will add to the angle error at the output of the telescope. Finally, the long-term drift pointing error at the output of the telescope will result in pointing and displacement errors at the output window and at the ISC table. These errors are summarized in Table 18 on page 58.

**Table 18: PO Beam Additional Long-term Drift Alignment Errors**

<i>Location</i>	$\Delta\theta, \text{ rad}$	$\Delta x, \text{ mm}$
telescope input	$\pm 1.5 \times 10^{-4}$	$\pm 1.4$
telescope output	$\pm 1.5 \times 10^{-3}$	$\pm 0.14$
output window	$\pm 1.5 \times 10^{-3}$	$\pm 1.5$
ISC table	$\pm 1.5 \times 10^{-3}$	$\pm 3.8$

### 7.3.5. PO Beam Alignment Error Correction

The initial alignment error will be accommodated by increasing the field-of-view and clear aperture of the PO telescope and the ISC optics.

*A long-term drift of 10% of the ISC clear aperture (approximately 4 mm), which is caused by independent BSC and HAM stack angular motions of  $50 \times 10^{-6}$  rad, will be tolerated.* Excessive long-term drift will be corrected periodically by means of the BSC and HAM stack actuator mechanisms. The DC offset changes of the BS SUS and RM SUS actuators are a measure of the tilts of the BSC2 SEI and the HAM3 SEI platforms. They can provide error signals to drive a tilt correction. The tilt of the BSC2 stack must be corrected first. Then the tilt of HAM4 SEI can be inferred after the tilt of BSC2 stack has been corrected by observing the offset of the PO beam at the ISC quadrant detector. The tilt of HAM4 stack will be corrected independently whenever the tilt exceeds the tolerable range.

### 7.3.6. PO Optics Clear Aperture and Field-of-view Requirements

The clear aperture and FOV of the PO telescopes, the output windows, and the ISC optics will be increased to allow for the initial alignment beam displacement error and for an additional error due to the periodically corrected long-term drift of the SEI platform. The results are presented in Table 19 on page 59.

**Table 19: Clear Aperture and Field-of-View Increase Needed to Compensate for Initial Alignment Errors of PO beams**

<i>Item</i>	<i>Initial Alignment Error</i>		<i>Drift Error</i>		<i>Total Field-of-view and Clear Aperture to cover initial alignment and drift errors</i>	
	$\Delta\theta$ , rad	$\Delta CA$ mm	$\Delta\theta$ , rad	$\Delta CA$ mm	$\Delta\theta$ , rad	CA mm
PO telescope input	$\pm 4 \times 10^{-4}$	12	$\pm 1.5 \times 10^{-4}$	2.8	$\pm 5.5 \times 10^{-4}$	173
PO telescope output	$\pm 4.4 \times 10^{-3}$	2	$\pm 1.5 \times 10^{-3}$	0.28	$\pm 5.9 \times 10^{-3}$	18
output window @ normal incidence	$\pm 4 \times 10^{-3}$	12	$\pm 1.5 \times 10^{-3}$	3.0	$\pm 5.5 \times 10^{-3}$	31
ISC input	$\pm 4 \times 10^{-3}$	27	$\pm 1.5 \times 10^{-3}$	7.5	$\pm 5.5 \times 10^{-3}$	49

## 8 ENGINEERING MOCK-UP

A mock-up of the BSC2 chamber will be constructed to facilitate the final design of the COS. The actual configuration and placement of COS elements is intimately dependent upon the location of COC suspension housings, and the actual paths of optical beams within the chamber. A full size mock-up will provide a sanity check on possible interference of the beam-dump baffles, and other bulky COS elements with other IFO elements. The mock-up will function as an engineering prototype by enabling engineering prototype suspensions, COS elements, etc. to be mounted to the SEI platforms. The mounted items will provide valuable information necessary for the implementation of workable IFO initial alignment procedures. A schematic layout of the mock-up is shown in figure 43.

### 8.1. ITM PO Beam Optical System Mock-up

The ITM PO beam optical system mock-up will consist of: 1) a simulated pick-off mirror mounted on the BSC optics platform, and 2) a simulated beam-reducing telescope assembly, and a relay mirror to direct the beam through the output vacuum port; all mounted to the HAM optical table. A simulated SUS cage assembly will be mounted to the BSC optics platform.

### 8.2. Anti-symmetric Port Pick-off Beam Optical System

The anti-symmetric port PO beam optical system mock-up will consist of: 1) a simulated beam-reducing telescope assembly, simulated Faraday isolator, and a relay mirror to direct the beam through the output vacuum port; all mounted to the HAM optical table.



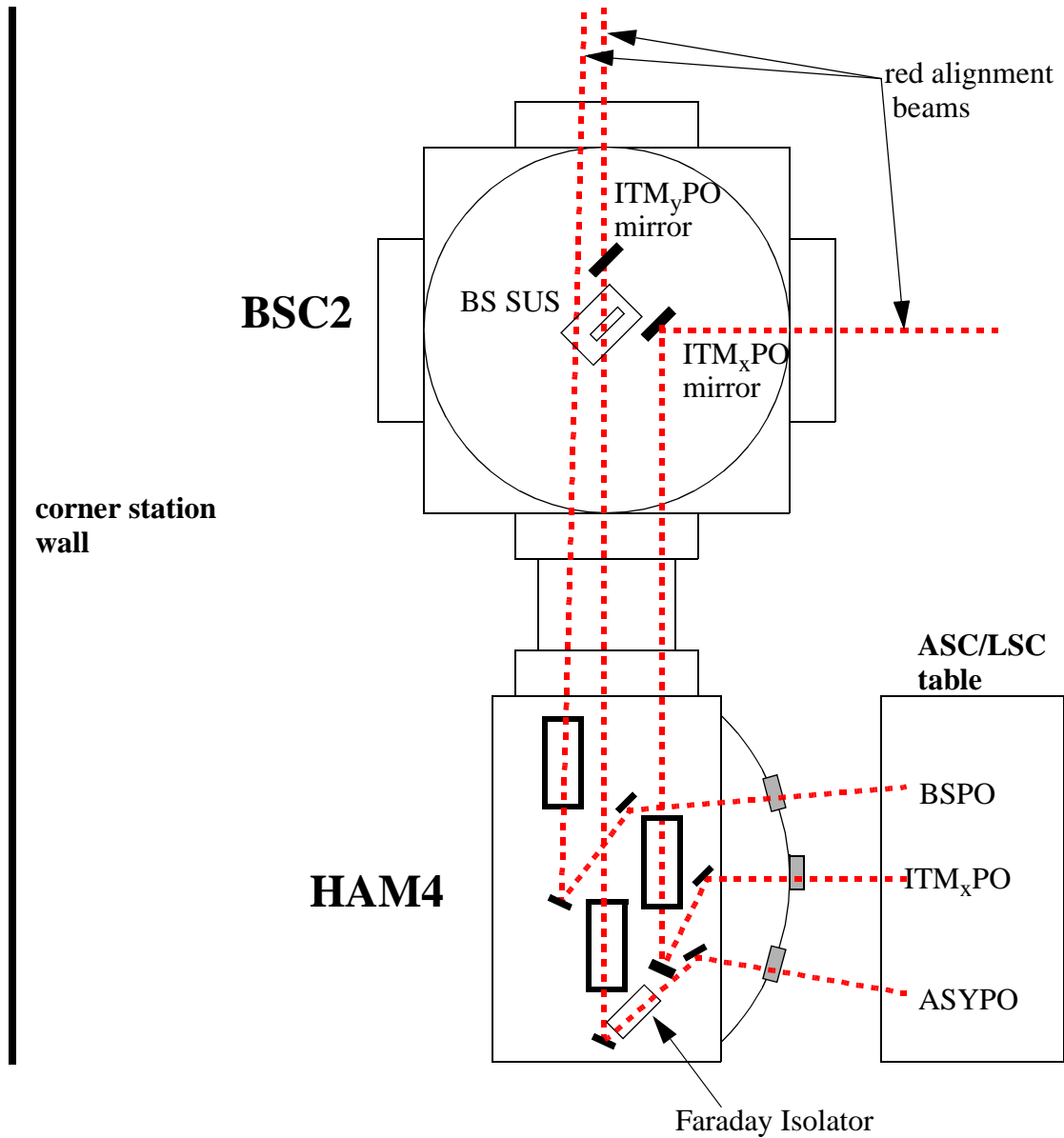


**Figure 43: Mock-up of COS Elements on BSC2/HAM4**

### 8.3. BS PO Beam Optical System

The BS PO beam optical system mock-up will consist of: 1) a simulated beam-reducing telescope assembly, and 2) a relay mirror to direct the beam through the output vacuum port; all mounted to the HAM optical table.

## 8.4. ETM PO Beam Optical System

The ETM PO beam optical system mock-up will consist of: 1) a simulated beam-reducing telescope assembly, hanging from the BSC optics platform, and 2) a relay mirror to direct the beam through the output vacuum port.

## 8.5. Beam-dump

### 8.5.1. Beam-dumps in the BSC2 chamber

Simulated beam-dumps for the  $ITM_xGBAR4$ ,  $ITM_yGBAR4$ , and  $RMGBHR3$  beams will be mounted to the inside of the BSC chamber walls.

### 8.5.2. Beam-dumps in the HAM4 chamber

A simulated beam-dump for the  $ITM_yGBAR1$  beam will be mounted to the inside of the HAM chamber wall, and a simulated beam-dump assembly for the  $BSGBAR1_x$  beam will be mounted to the surface of the HAM optical table.

A simulated stray light baffle will be mounted to the wall of the BSC to model the ITM/ETM baffling of the arm cavity.

# 9 ENGINEERING TEST PLANS

## 9.1. Receiving Inspection

All received optical parts; which will include telescope mirrors, folding mirrors, output windows, black glass beam-dump material, and dark-oxidized baffles will undergo a visual receiving inspection.

The receiving inspection will verify that the optical elements meet the appropriate scratch and dig, and other surface qualify specifications.

## 9.2. Engineering Tests

### 9.2.1. Alignment of PO Telescopes

A test apparatus will be developed for the pre-alignment, and testing of the collimation and centering of the telescopes during assembly. The apparatus will consist of 1) a full-aperture 1060nm wavelength collimated source, consisting of a low-power 1060nm wavelength laser with a beam expander and a spare 10X telescope assembly, 2) 670nm laser initial alignment beam, 3) miscellaneous mounting fixtures with alignment apertures, 4) alignment telescope, 5) IR interferometer, and 6) TV video caliper system for measuring the beam centering.

### 9.2.2. Wavefront Distortion of PO Telescopes

The output wavefront distortion of the telescopes will be measured using IR interferometric techniques.

### 9.2.3. BRDF Measurement of Beam-dump Surfaces.

A BRDF apparatus will be used to verify that the surfaces of the telescope optical elements, Faraday isolators, and the output windows meet the BRDF specifications.

### 9.2.4. Vibration Test of Telescope Assembly and PO Mirror Assembly

Vibration tests will be conducted to aid in the design as well as in the final verification, by determining the magnitudes of the low order resonant frequencies and the associated damping factors of the self-resonant modes of the telescope and PO mirror assemblies.

## 10 COS BILL OF ASSEMBLIES

The COS assemblies for the 4K IFO are listed in Table 20 on page 62.

**Table 20: COS Assemblies for the 4K IFO**

<i>ASSEMBLY</i>	<i>NO. REQD</i>	<i>DESCRIPTION</i>
BAF_ETMX	1	baffle, COC at end station x
BAF_ETMY	1	baffle, COC at end station y
BAF_ITMX	1	baffle, COC at vertex x
BAF_ITMY	1	baffle, COC at vertex y
BAF_LCPX_L	1	baffle, large cryopump x left
BAF_LCPX_R	1	baffle, large cryopump x right
BAF_LCPY_L	1	baffle, large cryopump y left
BAF_LCPY_R	1	baffle, large cryopump y right
BAF_MC	1	baffle, mode cleaner
BAF_SCPEX_L	1	baffle, small cryopump end x left
BAF_SCPEX_R	1	baffle, small cryopump end x right
BAF_SCPEY_L	1	baffle, small cryopump end y left
BAF_SCPEY_R	1	baffle, small cryopump end y right
BAF_SCPMX_L	1	baffle, small cryopump mid x left
BAF_SCPMX_R	1	baffle, small cryopump mid x right
<i>ASSEMBLY</i>	<i>NO. REQD</i>	<i>DESCRIPTION</i>
BAF_SCPMY_L	1	baffle, small cryopump mid y left

**Table 20: COS Assemblies for the 4K IFO**

BAF_SCPMY_R	1	baffle, small cryopump mid y right
BAF_SCPVX_L	1	baffle, small cryopump vertex x left
BAF_SCPVX_R	1	baffle, small cryopump vertex x right
BAF_SCPVY_L	1	baffle, small cryopump vertex y left
BAF_SCPVY_R	1	baffle, small cryopump vertex y right
BD_BSAR3P	1	beam-dump, BSGBAR3x'/3y'
BD_BSHR3P	1	beam-dump, BSGBHR3x'/3y'
BD_ITMXAR1	1	beam-dump, ITMxGBAR1
BD_ITMXAR4	1	beam-dump, ITMxGBAR4
BD_ITMXHR3_4	1	beam-dump, ITMxGBHR3/4
BD_ITMYAR1	1	beam-dump, ITMyGBAR1
BD_ITMYAR4	1	beam-dump, ITMyGBAR4
BD_ITMYHR3_4	1	beam-dump, ITMyGBHR3/4
BD_RMAR3	1	beam-dump, RMGBAR3
BD_RMHR3	1	beam-dump, RMGBHR3
MPO_BS	1	PO mirror assy, BS
MPO_ITMX	1	PO mirror assy, ITMX
MPO_ITMY	1	PO mirror assy, ITMY
MS_ETMX	1	steering mirror assy, ETMx
MS_ETMY	1	steering mirror assy, ETMy
MS_TEL-ITMY	1	steering mirror assy, ITMy
MS_TEL_APS	1	steering mirror assy, APS
MS_TEL_BS	1	steering mirror assy, BS
MS_TEL_ITMX	1	steering mirror assy, ITMx
PERSM_APS	1	periscope mirror assy, APS
PERSM_BS	1	periscope mirror assy, BS
PERSM_ETM_END	1	periscope mirror assy, ETM indistinct
PERSM_ETM_MID	1	periscope mirror assy, ETM Maidstone
PERSM_ITMX	1	periscope mirror assy, ITMx
PERSM_ITMY	1	periscope mirror assy, ITMy
TEL_ISC_APS	1	telescope, APS ISC
TEL_ISC_BS	1	telescope, BS ISC
TEL_ISC_ETMX	1	telescope, ETMx ISC
TEL_ISC_ETMY	1	telescope, ETMy ISC
<i>ASSEMBLY</i>	<i>NO. REQD</i>	<i>DESCRIPTION</i>
TEL_ISC_ITMX	1	telescope, ITMx ISC

**Table 20: COS Assemblies for the 4K IFO**

TEL_ISC_ITMY	1	telescope, ITMy ISC
TEL_PO_APS	1	telescope, APS
TEL_PO_BS	1	telescope, BS PO
TEL_PO_ETMX	1	telescope, ETMx PO
TEL_PO_ETMY	1	telescope, ETMy PO
TEL_PO_ITMX	1	telescope, ITMX PO
TEL_PO_ITMY	1	telescope, ITMY PO
WND_PO_APS	1	window assy, APS PO beam
WND_PO_BS	1	window, BS PO beam
WND_PO_ETMX	1	window, ETMx PO beam
WND_PO_ETMY	1	window, ETMy PO beam
WND_PO_ITMX	1	window assembly, ITMx PO beam
WND_PO_ITMY	1	window, ITMy PO beam

The COS assemblies for the 2K IFO are listed in Table 20 on page 62.

**Table 21: COS Assemblies for the 2K IFO****Table 22:**

<i>ASSEMBLY</i>	<i>NO. REQD</i>	<i>DESCRIPTION</i>
BAF_MIDX	1	baffle, COC at mid station x
BAF_MIDY	1	baffle, COC at mid station y
BD_BSAR3P	1	beam-dump, BSGBAR3x'/3y'
BD_BSHR3P	1	beam-dump, BSGBHR3x'/3y'
BD_ITMXAR1	1	beam-dump, ITMxGBAR1
BD_ITMXAR4	1	beam-dump, ITMxGBAR4
BD_ITMXHR3_4	1	beam-dump, ITMxGBHR3/4
BD_ITMYAR1	1	beam-dump, ITMyGBAR1
BD_ITMYAR4	1	beam-dump, ITMyGBAR4
BD_ITMYHR3_4	1	beam-dump, ITMyGBHR3/4
BD_RMAR3	1	beam-dump, RMGBAR3
BD_RMHR3	1	beam-dump, RMGBHR3
MPO_BS	1	PO mirror assy, BS
<i>ASSEMBLY</i>	<i>NO. REQD</i>	<i>DESCRIPTION</i>
MPO_ITMX	1	PO mirror assy, ITMX

**Table 21: COS Assemblies for the 2K IFO****Table 22:**

MPO_ITMY	1	PO mirror assy, ITMY
MS_ETMX	1	steering mirror assy, ETMx
MS_ETMY	1	steering mirror assy, ETMy
MS_TEL-ITMY	1	steering mirror assy, ITMy
MS_TEL_APS	1	steering mirror assy, APS
MS_TEL_BS	1	steering mirror assy, BS
MS_TEL_ITMX	1	steering mirror assy, ITMx
PERSM_APS	1	periscope mirror assy, APS
PERSM_BS	1	periscope mirror assy, BS
PERSM_ETM_END	1	periscope mirror assy, ETM ENDSTATION
PERSM_ETM_MID	1	periscope mirror assy, ETM MIDSTATION
PERSM_ITMX	1	periscope mirror assy, ITMx
PERSM_ITMY	1	periscope mirror assy, ITMy
TEL_ISC_APS	1	telescope, APS ISC
TEL_ISC_BS	1	telescope, BS ISC
TEL_ISC_ETMX	1	telescope, ETMx ISC
TEL_ISC_ETMY	1	telescope, ETMy ISC
TEL_ISC_ITMX	1	telescope, ITMx ISC
TEL_ISC_ITMY	1	telescope, ITMy ISC
TEL_PO_APS	1	telescope, APS
TEL_PO_BS	1	telescope, BS PO
TEL_PO_ETMX	1	telescope, ETMx PO
TEL_PO_ETMY	1	telescope, ETMy PO
TEL_PO_ITMX	1	telescope, ITMX PO
TEL_PO_ITMY	1	telescope, ITMY PO
TESTEQUIP	1	test equipment
WND_PO_APS	1	window assy, APS PO beam
WND_PO_BS	1	window, BS PO beam
WND_PO_ETMX	1	window, ETMx PO beam
WND_PO_ETMY	1	window, ETMy PO beam
WND_PO_ITMX	1	window assembly, ITMx PO beam
WND_PO_ITMY	1	window, ITMy PO beam

## APPENDIX 1 SCATTERED LIGHT NOISE CALCULATIONS

### 11 SCATTERED LIGHT NOISE CALCULATIONS

The scattered light from each COS scattering path was calculated, and their contribution to the scattered light phase noise budget was estimated using the parameters in Table 23 on page 66.

**Table 23: Noise Amplitude Parameters in the Frequency Range  $30 < f < 1000$  Hz**

<i>Noise Amplitude Parameter</i>	<i>30 Hz</i>	<i>100 Hz</i>	<i>1000Hz</i>
rms displacement amplitude of vacuum enclosure, $\text{m/Hz}^{1/2}$ --see SEI DRD	$x_{\text{vac}} < 1 \times 10^{-10}$	$x_{\text{vac}} < 1 \times 10^{-11}$	$x_{\text{vac}} < 1 \times 10^{-13}$
initial LIGO sensitivity, $\text{m/Hz}^{1/2}$ - see SRD	$X < 1 \times 10^{-18}$	$X < 1 \times 10^{-19}$	$X < 5 \times 10^{-19}$
standard quantum limit, 1000Kg (SQL), $\text{m/Hz}^{1/2}$ -- see SRD	$X_{\text{SQL}} < 5.3 \times 10^{-21}$	$X_{\text{SQL}} < 1.6 \times 10^{-21}$	$X_{\text{SQL}} < 1.6 \times 10^{-22}$
horizontal SEI transfer function, see SEI DRD	$A_{\text{SEI}} < 6 \times 10^{-5}$	$A_{\text{SEI}} < 1 \times 10^{-5}$	NA
horizontal SUS transfer function, see SEI DRD	$A_{\text{SUS}} < 7 \times 10^{-4}$	$A_{\text{SUS}} < 6 \times 10^{-5}$	$A_{\text{SUS}} < 6 \times 10^{-7}$
rms thermal displacement of SEI platform, $\text{m/Hz}^{1/2}$ , see Motion of Optical Platforms Driven by Thermal Noise from Spring Elements, LIGO-T97005-D	NA	NA	$X_{\text{SEIthermal}} < 3 \times 10^{-18}$

#### 11.1. Scattering from Vacuum Housing Mounted Surfaces

The maximum expected backscattered power from each ghost beams was calculated by assuming that the ghost beam diameters were demagnified 72x (corresponding to a Gaussian beam radius parameter of 0.5mm) and then scattered from seismic floor-mounted surfaces. The effective BRDF of the scattering surfaces in the demagnified PO beam was assumed to be  $\text{BRDF} = 8 \times 10^{-4} \text{ sr}^{-1}$ .

### 11.1.1. APS beam scattered light power

The APS beam is scattered by the output surfaces mounted on the vacuum housing, as shown schematically in figure 44. *Note that a Faraday isolator has been included to reduce the backscattered light to acceptable levels.* The expected backscattered power of the APS beam ( $P_{S_{APS}}$ ) was calculated with the following equation.

$$P_{S_{DPS}} = P_0 \cdot \frac{P_{DPS}}{P_0} \cdot T_{BSAR} \cdot [\cos\theta_{iwo} \cdot BRDF_{w_0}(\theta_s)] \cdot \Delta\Omega \cdot \frac{1}{M^2} \cdot A_{Fi}, \text{ where}$$

transmissivity of BS AR coating,

$$T_{BSAR} = 0.999$$

scattering surface incidence angle

$$\theta_{iwo} = 57 \text{ deg}$$

de-magnification of the beam

$$M = 0.01389$$

power attenuation factor of the Faraday isolator

$$A_{Fi} = 0.001,$$

ratio of the APS signal to the input laser power,

$$P_{DPS}/P_0 = 0.05$$

laser power

$$P_0 = 6 \text{ watts}$$

laser wavelength

$$\lambda = 1.06 \times 10^{-6} \text{ m}$$

IFO Gaussian beam parameter

$$w_0 = 0.0364 \text{ m.}$$

IFO scattering solid angle

$$\Delta\Omega = \frac{1}{\pi} \cdot \frac{\lambda^2}{w_0^2} = 2.7 \times 10^{-10} \text{ sr}$$

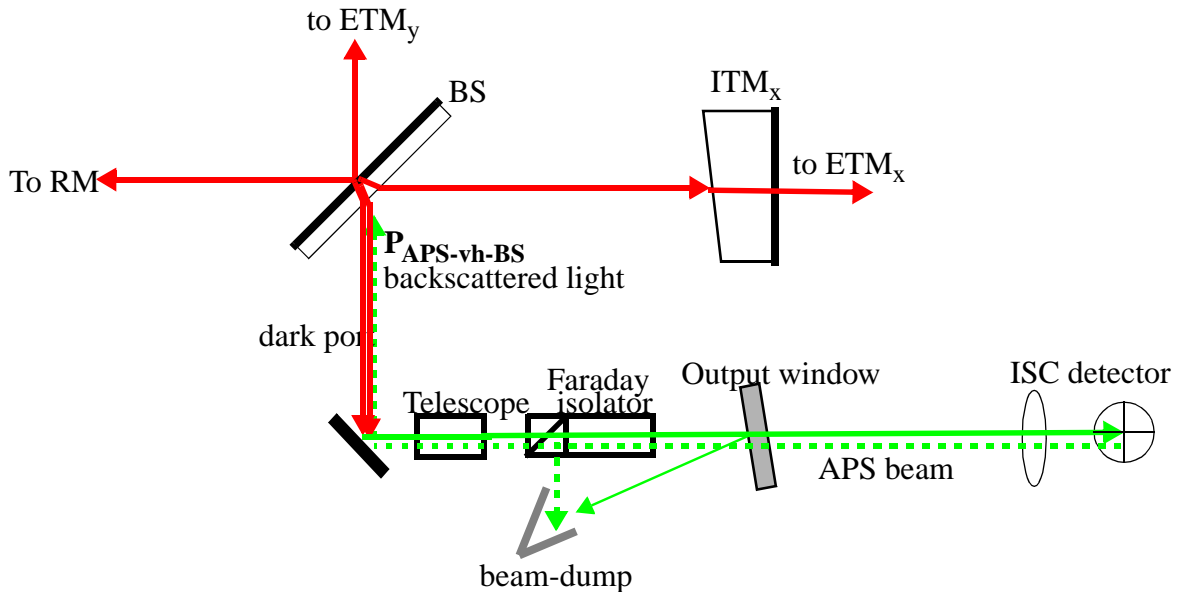


**Figure 44: The Scattered APS Beam from the Output Window Mounted on the Vacuum Housing**



Then  $P_{s_{APS}} = 3.3 \times 10^{-13}$  watt.

### 11.1.2. ITM PO beam scattered light power

The ITM<sub>x</sub> and ITM<sub>y</sub> PO beams back-scatters from the output windows and inject noise fields into the recycling cavity, as shown functionally in figure 45.

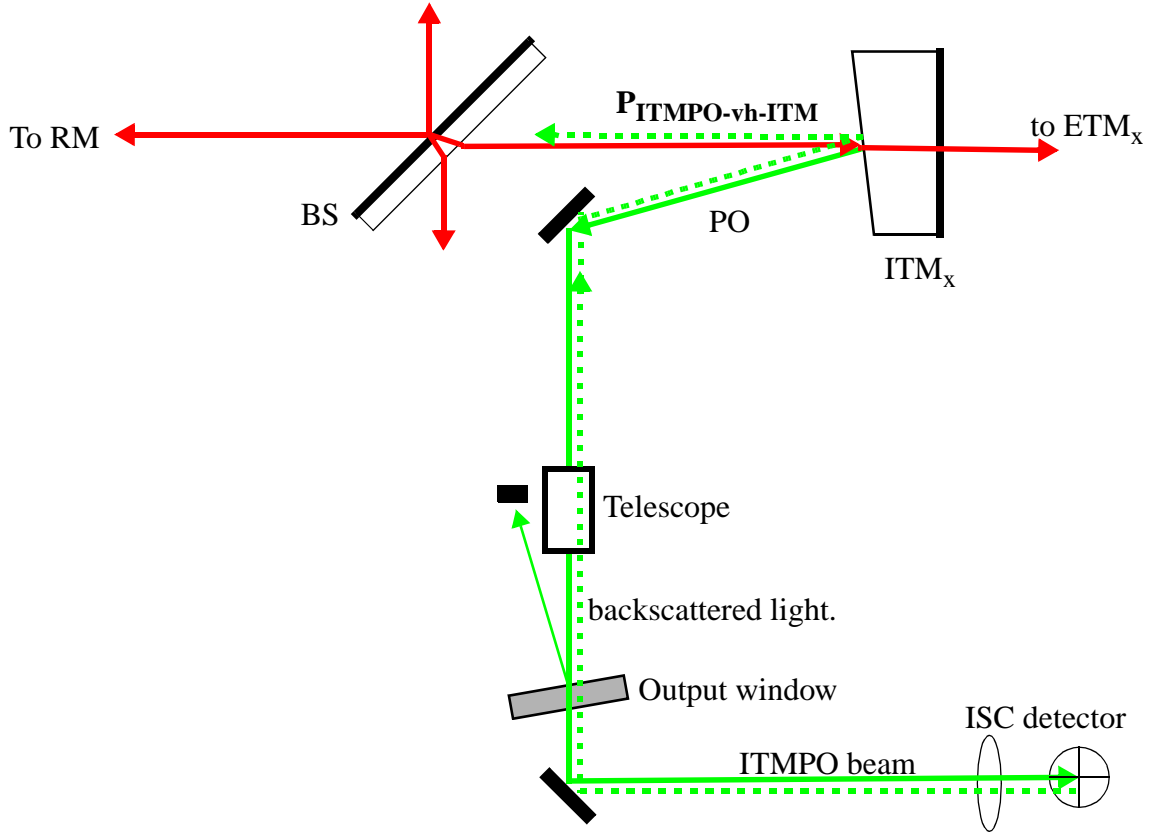


**Figure 45: Backscattered light from ITM<sub>x</sub> PO and ITM<sub>y</sub> PO beams injects noise into the recycling cavity.**

Note that the output window must be tipped in order to avoid a direct glint into the IFO from the parallel AR surfaces of the window. The scattered light power was calculated with the following equation.

$$P_{s_{ITM}} = P_0 \cdot \frac{1}{2} \cdot \left(\frac{P_i}{P}\right)_{ITMPO}^2 \cdot G_{rc} \cdot [\cos \theta_{iwo} \cdot BRDF_{wo}(\theta_s)] \cdot \Delta\Omega \cdot \frac{1}{M^2}, \text{ where}$$

scattering surface incidence angle

$$\left(\frac{P_i}{P}\right)_{ITMPO} = R_{ITMAR}$$

$$\theta_{iwo} = 57 \text{ deg}$$

magnification of the telescope  
 scattering solid angle  
 reflectivity of ITM AR coating  
 recycling cavity gain

$$M = 0.01389$$

$$\Delta\Omega = 2.7 \times 10^{-10} \text{ sr}^{-1}$$

$$R_{ITMAR} = 0.001$$

$$G_{rc} = 50$$

Then  $P_{s_{ITM}} = 1.5 \times 10^{-13}$  watt.

### 11.1.3. ETM PO beam scattered light power

ETM PO beam backscatters into the arm cavity from the output surfaces mounted on the vacuum housing, as shown in Figure 46

A neutral density attenuator is placed in the output PO beam after the telescope to attenuate the scattered light.

The expected backscattered power of the ETM PO beam  $P_{s_{ETM}}$  was calculated with the following equation.

$$P_{s_{ETM}} = P_0 \cdot \frac{1}{2} \cdot \left(\frac{P_i}{P}\right)_{ETMPO}^2 \cdot G_{rc} \cdot T_{FP} \cdot T_{ND} \cdot [\cos\theta_{iwo} \cdot BRDF_{wo}(\theta_s)] \cdot \Delta\Omega \cdot \frac{1}{M^2},$$

$$\left(\frac{P_i}{P}\right)_{ETMPO} = T_{AR},$$

transmissivity of ETM AR coating  
 transmissivity of ETM HR coating  
 reflectivity of ETM HR coating  
 reflectivity of ITM HR coating  
 recycling cavity gain  
 scattering surface incidence angle  
 magnification of the telescope  
 IFO scattering solid angle  
 transmissivity of the Fabry-Perot arm cavity at resonance is

$$T_{ETMAR} = 0.999$$

$$T_{ETMHR} = 0.000020$$

$$R_{ETMHR} = 0.999980$$

$$R_{ITMHR} = 0.97$$

$$G_{rc} = 50$$

$$\theta_{iwo} = 57 \text{ deg}$$

$$M = 0.01389$$

$$\Delta\Omega = 2.7 \times 10^{-10} \text{ sr}^{-1}$$

$$T_{FP} = \frac{(1 - R_{ITMHR}) \cdot (1 - R_{ETMHR})}{(1 - \sqrt{R_{ITMHR} \cdot R_{ETMHR}})^2} = 0.0026$$

$$T_{ND} = 0.10$$

transmissivity of neutral density filter

Then  $P_{s_{ETM}} = 2.4 \times 10^{-12}$  watt.

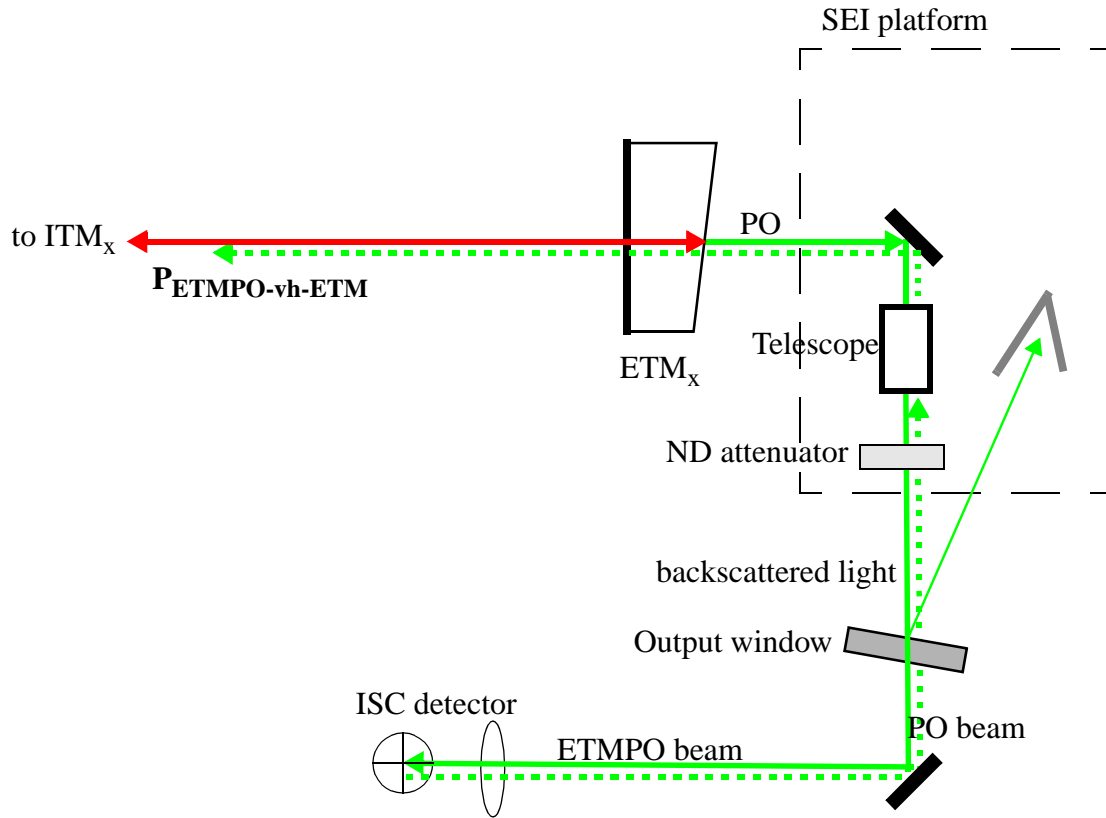


**Figure 46: ETM PO beam backscattered into arm cavity from output window mounted on vacuum housing**

### 11.1.4. SPS beam scattered light power

The SPS beam will scatter from the surfaces of the output window and inject noise into the recycling cavity through the RM, as shown in figure 47.

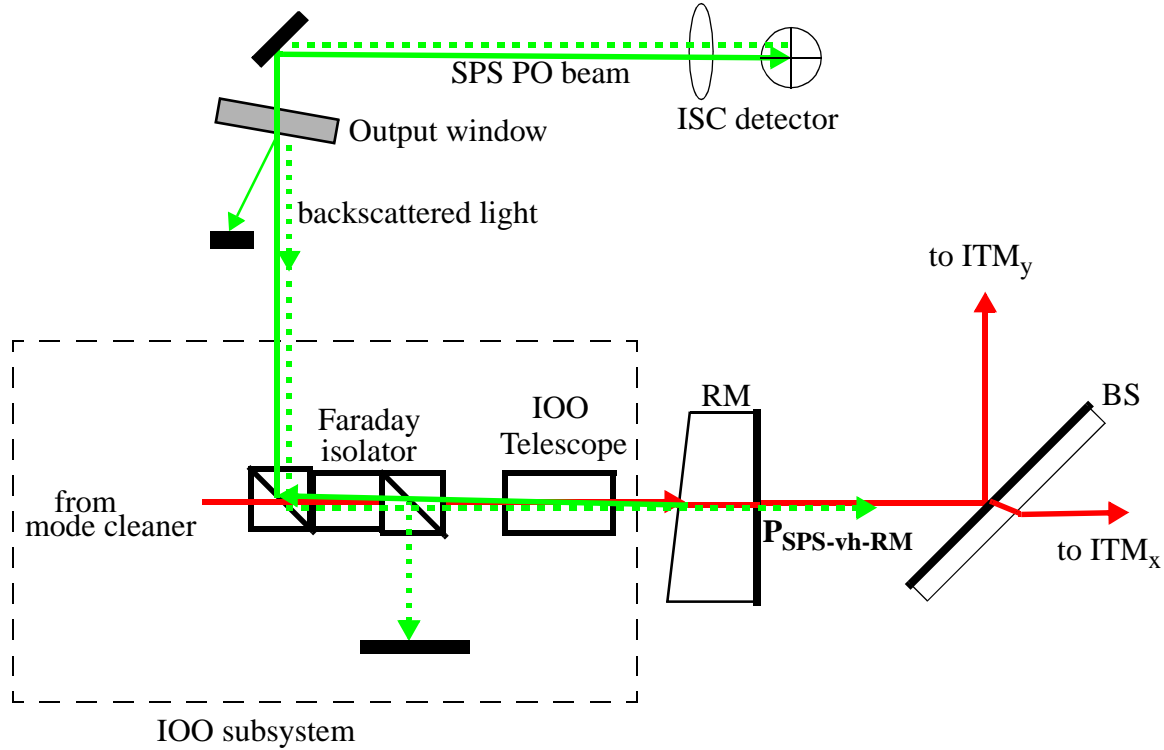


**Figure 47: RM SPS beam backscattered into recycling cavity from output window mounted on vacuum housing**

The expected backscattered power of the SPS PO beam  $P_{sSPS}$  was calculated with the following equation.

$$P_{sSPS} = P_0 \cdot \left( \frac{P_{SPS}}{P_0} \right) \cdot T_{HR} \cdot T_{AR} \cdot [\cos \theta_{iwo} \cdot BRDF_{wo}(\theta_s)] \cdot \Delta\Omega \cdot \frac{1}{M^2} \cdot A_{Fi},$$

ratio of the SPS signal to the input laser power,  $\frac{P_{SPS}}{P_0} = 0.02$

$$A_{Fi} = 0.001$$

$$T_{RMAR} = 0.999$$

$$T_{RMHR} = 0.03$$

$$\theta_{iwo} = 57 \text{ deg}$$

$$M = 0.05$$

$$\Delta\Omega = 2.7 \times 10^{-10} \text{ sr}^{-1}.$$

Then  $P_{sSPS} = 1.8 \times 10^{-12}$  watt.

## APPENDIX 2 GHOST BEAM GLINT CALCULATIONS

### 12 GHOST BEAM GLINT CALCULATIONS

Those ghost beams that are not dumped may hit a surface and cause a glint back into the IFO. The worst case glint from a chamber wall will occur when the ghost beam hits a cylindrical surface aligned exactly perpendicular to the ghost beam direction, as shown in the figure 48 (note: the surface can be either convex or concave). An example of such a glint surface might be the inner wall of the BSC housing.

The ghost beam glint from the reflecting surface will retroreflect into the solid angle of the IFO, provided the tilt of the curved surface is within the diffraction angle of the IFO beam. The maximum illuminated area of the glint surface which meets these conditions is

$$A_g = R\theta_d w = R \cdot \left( \frac{2}{\pi} \cdot \frac{\lambda}{w} \right) \cdot w = \frac{2}{\pi} R\lambda.$$

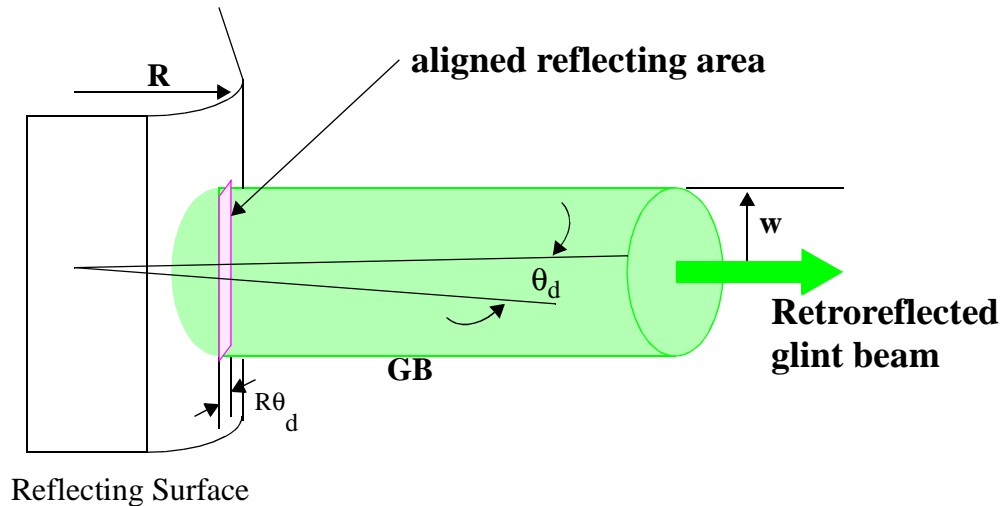


**Figure 48: Glint Reflection of GBAR<sub>3</sub> Back Into the IFO**

The retroreflected light from the glint into the IFO is proportional to the incident power, to the ratio of glint area to ghost beam area, and to the return transmissivity through the COC. An additional factor, the glint efficiency  $\eta_{glint}$ , has been included to account for the roughness of the surface and the coherent reduction of the reflected amplitude due to interference effects. See “Glint Efficiency” on page 73.

$$P_g = P_i \cdot \frac{2R\lambda}{\pi^2 w^2} \cdot T\eta_{glint}.$$

The width of the glint surface is  $l = \frac{2}{\pi} \cdot \frac{R\lambda}{w}$ . The geometric optics approximation is valid for  $l \gg \lambda$ ; so with a 1.064 micron wavelength beam, the approximation is valid for  $R > 0.4m$

We will estimate the glint power assuming a radius of  $R=1.5m$ , which corresponds to the inside wall of the BSC chamber, using the following parameters:

$$R=1.5m$$

$$w=0.0364 m$$

$$\theta_d = 9.3 \times 10^{-6} \text{ rad},$$

$$\eta_{glint} = 1 \times 10^{-5}$$

$$P_g = 2.43 \times 10^{-9} P_i T$$

## 12.1. Glint Efficiency

Two different phenomena associated with the surface roughness account for a reduction in the glint power; 1) the random surface curvature causes a local deviation of the reflected beam power away from the IFO solid angle, and 2) the optical path length differences due to local surface irregularities causes a reduction in the reflected wave amplitude because of coherent wave interference across local regions of the surface.

### 12.1.1. Surface Curvature Efficiency

The glint area consists of a narrow strip a few tens of wavelengths wide with a length equal to the beam diameter. Along the length of the glint strip the surface topology will change drastically due to the surface irregularity and surface roughness. It will be assumed that the surface height does not change across the width because the dimension is so small, and that the surface variation can be treated as a one-dimensional function. The topology of the glint surface is shown schematically in figure 49

Only the local surfaces that are tilted within the diffraction angle of the IFO beam will reflect light power into the beam, so the surface curvature efficiency can be defined as the fraction of surface angles which are less than the IFO diffraction angle. For the purpose of estimating the local surface curvatures, we will assume that the surface amplitude spectrum can be described as a spatial frequency power law

$\zeta_{0v} = A_0 v^{-n}$ , where the amplitude coefficient is related to the maximum surface height at the lowest frequency by

$$A_0 = \zeta_0 v_0^n.$$

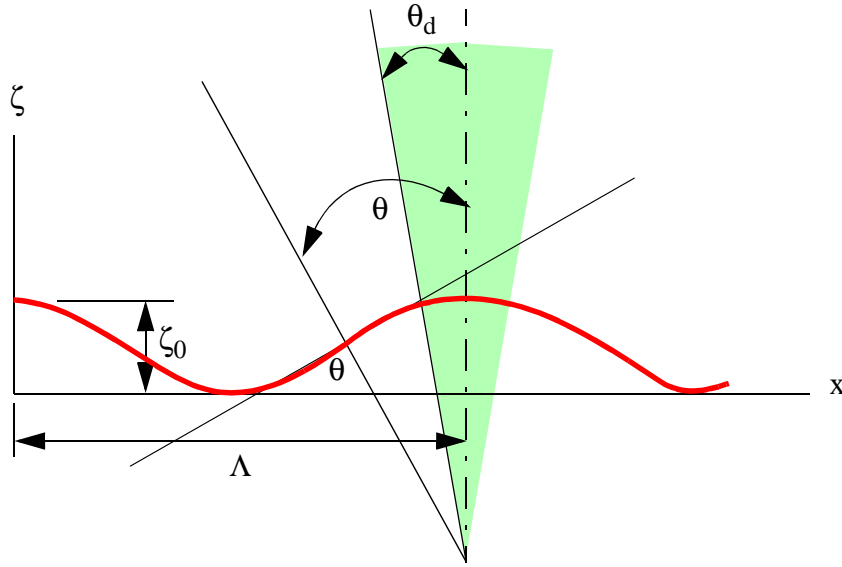


**Figure 49: Topology of the glint surface**

The spatial frequency is related to the period of the surface ripple component

$$v = \frac{2\pi}{\Lambda}.$$

A typical component of the surface spectrum can be described mathematically as

$$\zeta = \zeta_{0v} \cos\left(\frac{2\pi x}{\Lambda}\right).$$

The local tilt of the surface is given by

$$\theta = \frac{d\zeta}{dx} = -\zeta_{0v} \frac{2\pi}{\Lambda} \sin\left(\frac{2\pi x}{\Lambda}\right), \text{ and the condition for a glint reflection is } |\theta| \leq \theta_0.$$

This places a limit on the maximum fractional length within a component surface period which can contribute to the glint,

$$\frac{x_m}{\Lambda} \leq \frac{1}{2\pi} \sin\left(\theta_0 \frac{\Lambda}{2\pi \zeta_{0v}}\right)^{-1}$$

The total fractional contribution, which will be defined as the glint surface efficiency, is obtained by integrating over all possible surface ripple components, from the minimum to the maximum spatial frequencies.

$$\eta_{\text{glint\_sur}}(v_m) := \int_{v_0}^{v_m} \frac{\text{asin}\left(\frac{\theta_0}{v \cdot \zeta_{0v}(v)}\right)}{2 \cdot \pi \cdot (v_m - v_0)} dv$$

This expression was evaluated assuming a  $1/v$  surface spectral distribution law, with the following parameters.

IFO divergence angle	$\theta_0 = 9.3 \times 10^{-6}$ rad
minimum spatial frequency	$v_0 = 0.17$ 1/mm
maximum surface height	$\zeta_0 = 0.2$ mm

Then  $\eta_{glint_{sur}}(v_m) = 4.3 \times 10^{-5}$ ,

and the value is independent of the maximum surface frequency because of the assumed  $1/v$  surface spectral distribution law.

### 12.1.2. Coherence Efficiency

The beam illuminating the glint area is coherent across the entire length of the area and the entire area is within a resolution element of the COC mirror, therefore the net reflected light amplitude is the algebraic sum of the differential reflected amplitudes with varying phases across the length of the glint surface.

The differential reflected light wave amplitude due to a particular spatial frequency component is

$dE = E_0 \cos\left(\frac{4\pi}{\lambda} \zeta_{0v}(v)\right)$ , and the total amplitude is obtained by integrating over all possible spatial frequencies. The square of the ratio of net amplitude to peak amplitude will be defined as the glint coherence efficiency.

$$\eta_{glint_{coh}}(v_m) := \left[ \int_{v_0 + \delta}^{v_m} \frac{\cos\left(\frac{\pi \cdot \zeta_{0v}(v)}{\lambda}\right)}{(v_m - v_0 - \delta)} dv \right]^2$$

### 12.1.3. Total Glint Efficiency

The total glint power efficiency is the product of the two efficiencies. The results are plotted in figure 50. From these data we can estimate the maximum glint efficiency,  $\eta_{glint_{max}} < 1 \times 10^{-5}$ .



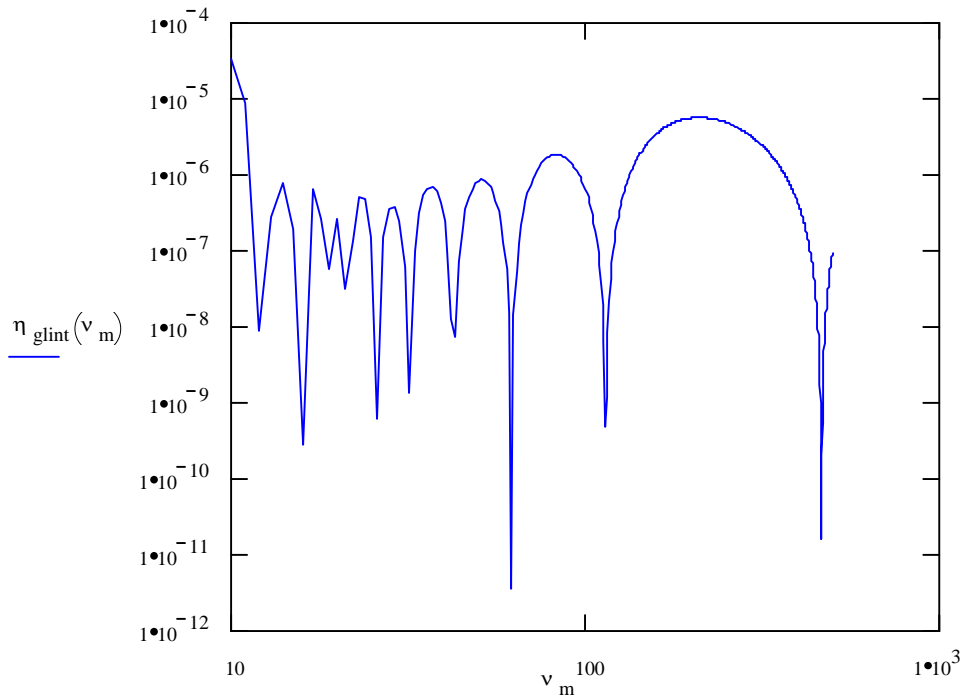


**Figure 50: Total glint efficiency as a function of maximum spatial frequency**

## APPENDIX 3 SCATTERING FROM COC SURFACES

### 13 SCATTERING FROM COC SURFACES

The need for baffles within the beam tube region and at the ends of the tube is dependent upon the scattering characteristics of the COC mirrors. The scattering probability per solid angle (BRDF) of the superpolished COC optical surfaces can be described empirically by a fractal expression with coefficients chosen to match the experimental data.

$$BRDF(\theta) = \frac{BRDF_0}{(1 + b\theta^2)^{\frac{c+1}{2}}}$$

Scattering data from two representative samples of superpolished fused silica mirror surfaces was obtained from the Pathfinder Optics. GO S/N 5 represents the lowest observed surface microroughness, and CSIRO S/N 2 is assumed to be typical of the LIGO superpolished mirrors. A fit of the one-dimensional surface roughness power spectral density data to the fractal expression was done by A. Lazzarini<sup>1</sup> for both these optical surfaces. The resulting BRDF is shown in figure 51.

1. Scattered Light and its Control in the LIGO Beam Tubes, Albert Lazzarini, LIGO Science Meeting Talk, 4/1/97

GO S/N 5 
$$BRDF_2(\theta) = \frac{1000}{(1 + 5.302 \times 10^8 \cdot \theta^2)^{1.55}} \text{ sr}^{-1}$$

CSIRO S/N/ 2 
$$BRDF_1(\theta) = \frac{2755}{(1 + 8.508 \times 10^8 \cdot \theta^2)^{1.24}} \text{ sr}^{-1}$$

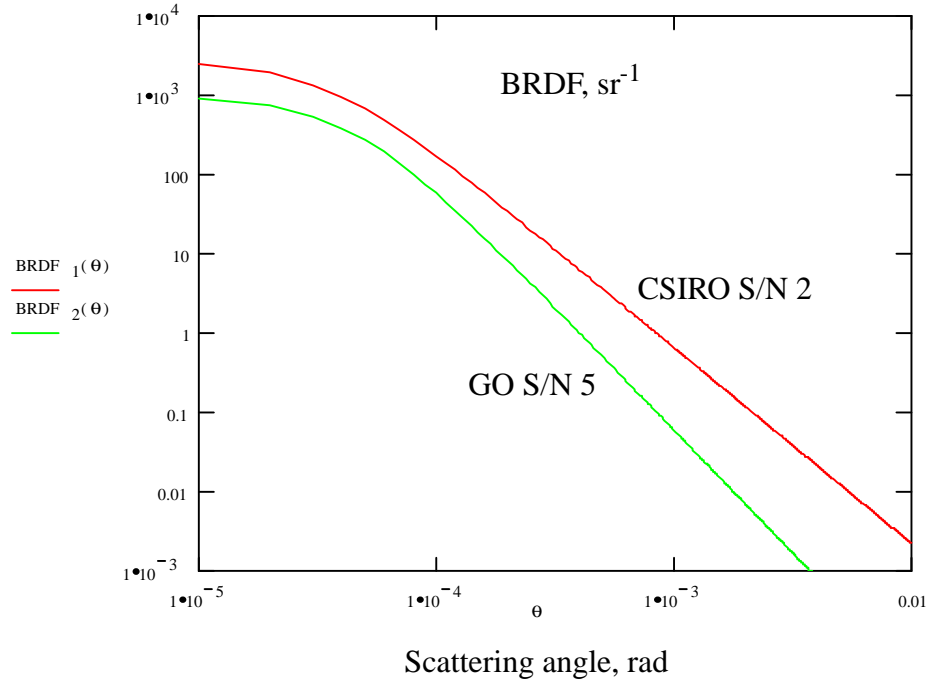


**Figure 51: BRDF of Pathfinder Optics: GO S/N 5 and CSIRO S/N2**

A significant amount of small angle scattered light from the COC mirrors will pass out the far end of the beam tube. This is calculated by integrating the BRDF of the COC mirror over the solid angle subtended by the far end of the beam tube.

$$P_2(\theta_{\max}) := P_1 \cdot 2 \cdot \pi \cdot \int_0^{\theta_{\max}} BRDF_2(\theta) \cdot \sin(\theta) d\theta$$

The calculation was made for the two representative BRDF functions described above, with 5000 watts in the arm cavity incident on the mirror. The results are shown in figure 52. The scattering angles subtended by the far end of the 2K and 4K beam tubes are shown for reference.

scattering angle subtended by the far end of the 2K beam tube  $3 \times 10^{-4}$  rad

scattering angle subtended by the far end of the 4K beam tube  $1.5 \times 10^{-4}$  rad

Note that with the higher BRDF approximately 150 milliwatts will be scattered out the far end of the beam tube in the 2K IFO.

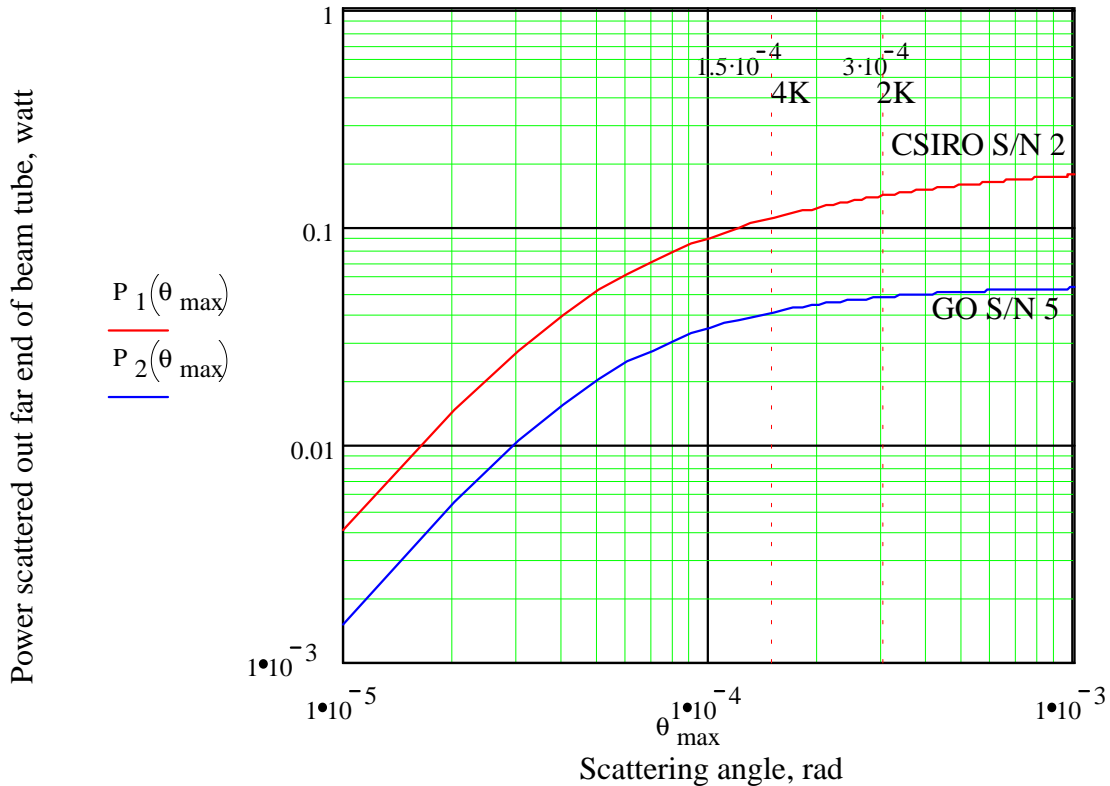


Figure 52: Scattered power from COC mirror out the far end of the beam tube

## APPENDIX 4 THE EFFECT OF OPTICAL ABERRATIONS ON THE WAVEFRONT SENSOR SIGNAL

### 14 THE EFFECT OF OPTICAL ABERRATIONS ON THE WAVEFRONT SENSOR SIGNAL

A determination of the effect of wavefront aberrations on the WFS signal, such as spherical aberrations in the PO beam optical train which destroy the Gaussian characteristic of the beam, was analyzed by using amplitude and phase maps for the carrier and sideband beams generated by the coherent optical modeling program ASAP, as described in *Effect of PO Telescope Aberrations on Wavefront Sensor Performance*, LIGO-T980007-D. A summary of these results is presented in the following.

The ASAP optical model used for the analysis of a typical PO beam optical train is shown in figure 53.

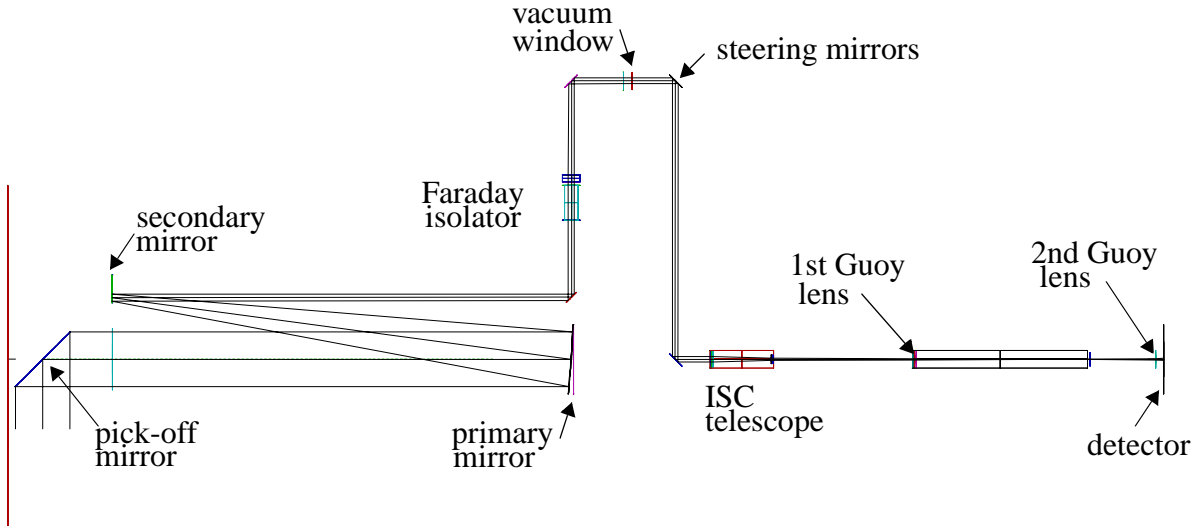


**Figure 53: ASAP model of typical PO beam optical train**

The electric field distributions for the sideband and carrier beams are calculated by ASAP program and are output in the form of  $m \times n$  discrete amplitude and phase values for the set of  $x_m$ ,  $y_n$  coordinate sample values. Then the field distributions can be represented as

$$E_C = E_{aC}(x_m, y_n) \cdot e^{i\phi_C(x_m, y_n)}, \quad E_{SB} = E_{aSB}(x_m, y_n) \cdot e^{i\phi_{SB}(x_m, y_n)},$$

and the intensity across the detector is given by

$$I_{mn} = E_{aC}(x_m, y_n) \cdot E_{aSB}(x_m, y_n) \cdot 2 \sin(\phi_C(x_m, y_n) - \phi_{SB}(x_m, y_n)).$$

The point by point product of the amplitudes and the sin of the phase difference between the sideband and carrier wavefronts were integrated numerically over the two halves of the detector plane along either axis and subtracted to obtain the predicted WFS signal.

The WFS signal integration across the detector can be approximated with a summation over the indices of the spatial map

$$S = \Delta x \Delta y \cdot \left( \sum_{n=0}^n \sum_{m=-n}^n I_{mn} - \sum_{n=-n}^{-n} \sum_{m=0}^n I_{mn} \right),$$

where  $\Delta x$  and  $\Delta y$  are the sampling increments of the spatial map coordinates, and  $m=n=0$  corresponds to the center of the detector plane  $x=y=0$ .

## 14.1. ASAP Wavefront Model Numerical Results

### 14.1.1. 0.9 Waves Astigmatic Aberration

The total aberration was computed by calculating the rms sum of the expected individual aberrations on each element in the optical train. Then, the aberrations were placed on each element

using Zernike coefficients in ASAP, and apportioned according to their rms contribution; with the requirement that the linear sum of the aberrations in the optical train have the same total as the rms total. The ASAP-geometric model was used to calculate the WFS signal for the case  $0.9\lambda$  total spherical aberration on the PO beam optical train. The details of the aberration calculations are shown in Table 24 on page 80.

**Table 24: Equivalent Surface Sag for Total 0.9 Wave RMS Astigmatic Aberration on the PO Beam Optical Train**

	<i>p-v</i> aberration per item	<i>p-v</i> aberration per item	<i>net</i> aberration	<i>aberration</i> <i>squared</i>	<i>fractional</i> <i>contribution</i>	<i>least squares</i> <i>linear</i> <i>equivalent</i>
	<i>waves</i> @.6328	<i>waves @ 1.06</i>				
pick-off mirror	0.250	0.149	0.297	0.088	0.109	0.098
PO telescope, primary	0.500	0.297	0.595	0.354	0.437	0.393
PO telescope, secondary	0.250	0.149	0.297	0.088	0.109	0.098
Faraday Isolator	0.433	0.258	0.258	0.066	0.082	0.074
isolator windows (2)	0.225	0.134	0.189	0.036	0.044	0.040
tel fold mirrors (5)	0.100	0.059	0.266	0.071	0.087	0.079
output window	0.225	0.134	0.134	0.018	0.022	0.020
ISC Telescope, objective	0.250	0.149	0.149	0.022	0.027	0.025
ISC Telescope, eyepiece	0.250	0.149	0.149	0.022	0.027	0.025
Guoy 1st lens	0.250	0.149	0.149	0.022	0.027	0.025
Guoy 2nd lens	0.250	0.149	0.149	0.022	0.027	0.025
sum of squares				0.810	1.000	0.900
total least squares p-v						0.900

The Zernike astigmatism coefficient describes a surface that has a value of sag equal to the coefficient along the x-axis and an equal amount of opposite sag along the y-axis; i.e the measured total p-v sag is exactly twice the value of the coefficient. Therefore the Zernike coefficient should be half the value of the desired p-v sage of the surface. Also, reflective surfaces contribute a total wavefront sag which is twice the value of the surface sag. These factors of two were taken into account when the total modeled aberration was apportioned among the elements in the optical train. The actual astigmatic Zernike coefficient values placed on the optical elements to produce a total 0.9 wave p-v added in an rms manner are shown in Table 25 on page 81

**Table 25: Equivalent Linear Astigmatic Zernike Coefficients for a Total 0.9 Wave RMS Aberration on the PO Beam Optical Train**

<i>element</i>	<i>equivalent Zernike aberration on surface, waves @ 1.06</i>
pick-off mirror	-0.025
PO telescope, primary	0.098
PO telescope, secondary	-0.025
Faraday Isolator	-0.037
isolator windows (2)	-0.020
tel fold mirrors (5)	-0.020
output window	-0.010
ISC Telescope, objective	-0.012
ISC Telescope, eyepiece	-0.012
Guoy 1st lens	-0.012
Guoy 2nd lens	0.012
total least squares p-v	0.900

ASAP amplitude and phase data files were obtained for a range of Guoy phase values with 0.01 normalized displacement and 0.01 normalized tilt of the carrier beam within the IFO. Two data sets were obtained, with +0.9 waves astigmatic aberration to represent the x-axis signal and with -0.9 waves astigmatic aberration to represent the y-axis.

A typical carrier and sideband amplitude product with +0.9 waves astigmatism for a normalized carrier displacement of 0.01 at 135 deg Guoy phase is shown in figure 54.

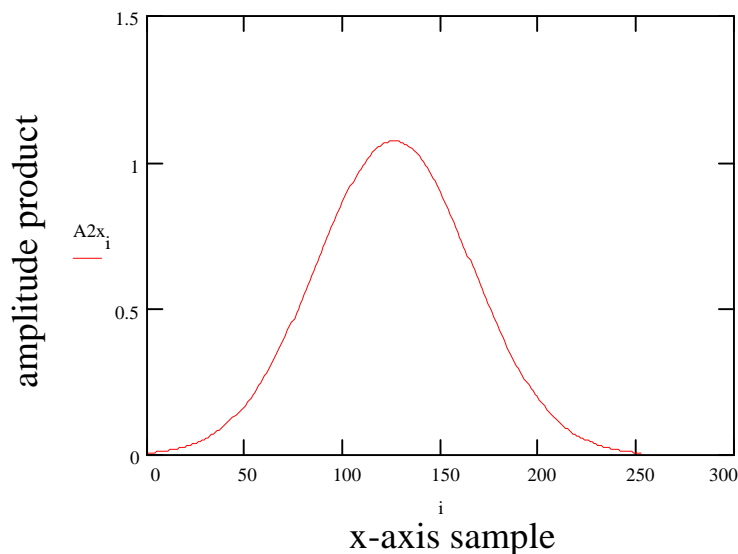


**Figure 54: Carrier and Sideband Amplitude Product at 135 deg Guoy Phase, for 0.01 Displacement, 0.9 Wave RMS Astigmatic Aberration**

A typical carrier and sideband wavefront phase difference for a normalized carrier displacement of 0.01 at 135 deg Guoy phase is shown in figure 55.

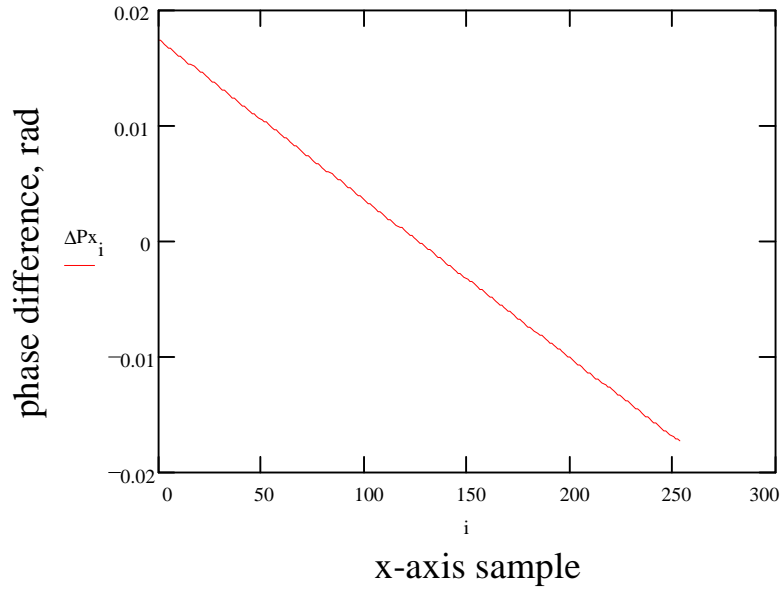


**Figure 55: Carrier and Sideband Wavefront Phase Difference at 135 deg Guoy Phase, for 0.01 Displacement, 0.9 Wave RMS Astigmatic Aberration**

A typical carrier and sideband intensity distribution across the WFS detector for a normalized carrier displacement of 0.01 at 135 deg Guoy phase is shown in figure 56.

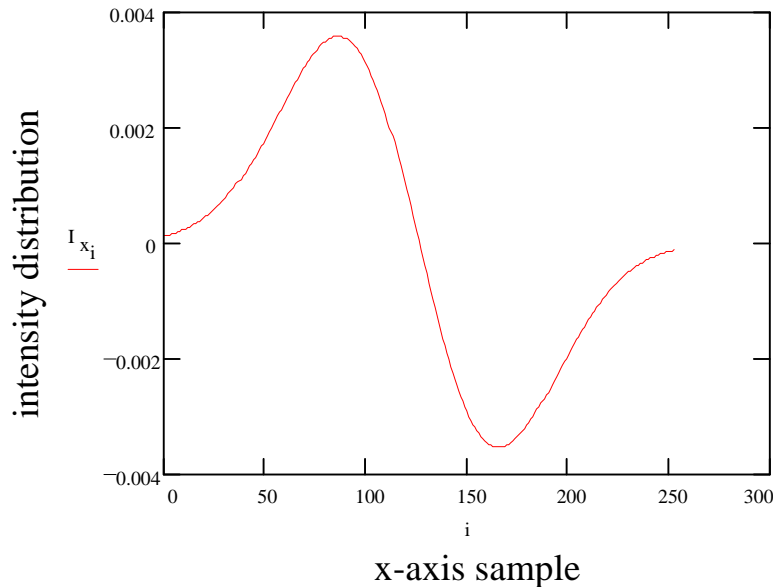


**Figure 56: Carrier and Sideband Intensity Distribution at 135 deg Guoy Phase, for 0.01 Displacement, 0.9 Wave RMS Astigmatic Aberration**

A contour profile of the intensity distribution across the WFS detector for a normalized carrier displacement of 0.01 at 135 deg Guoy phase is shown in figure57. There is a slight amount of cross-coupling of the x-axis tilt into the y-axis signal. However, the tilt component in the y-axis is negligible compared to the x-axis. The intensity distribution has the characteristics of the product of a TEM10 and TEM00 Gaussian modes, as predicted by the WFS modal model.

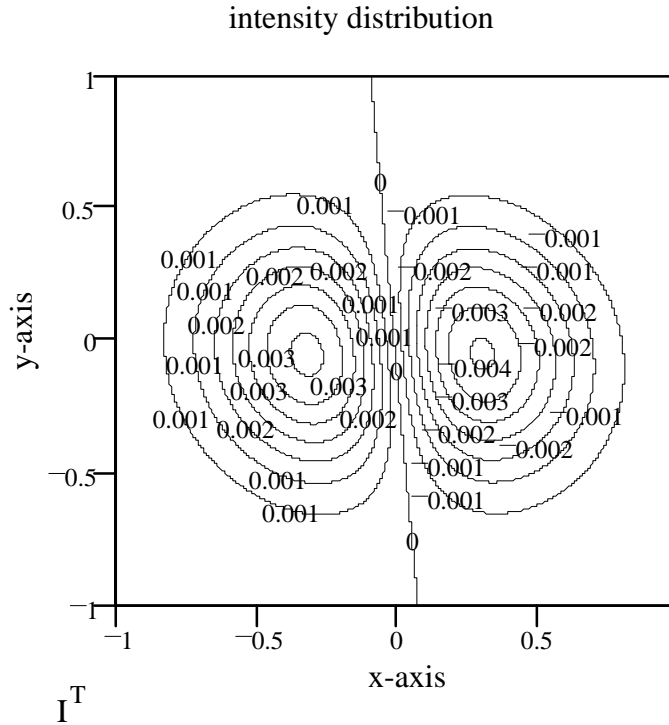


**Figure 57: Carrier and Sideband Wavefront Intensity Map at 135 deg Guoy Phase, for 0.01 Displacement, 0.9 Wave RMS Astigmatic Aberration**

A summary of the displacement and tilt WFS signals for various Guoy phases with +0.9 waves astigmatism and -0.9 waves astigmatism are shown in figures 58 and 59. The individual data points are connected with straight lines in all of the figures for clarity.



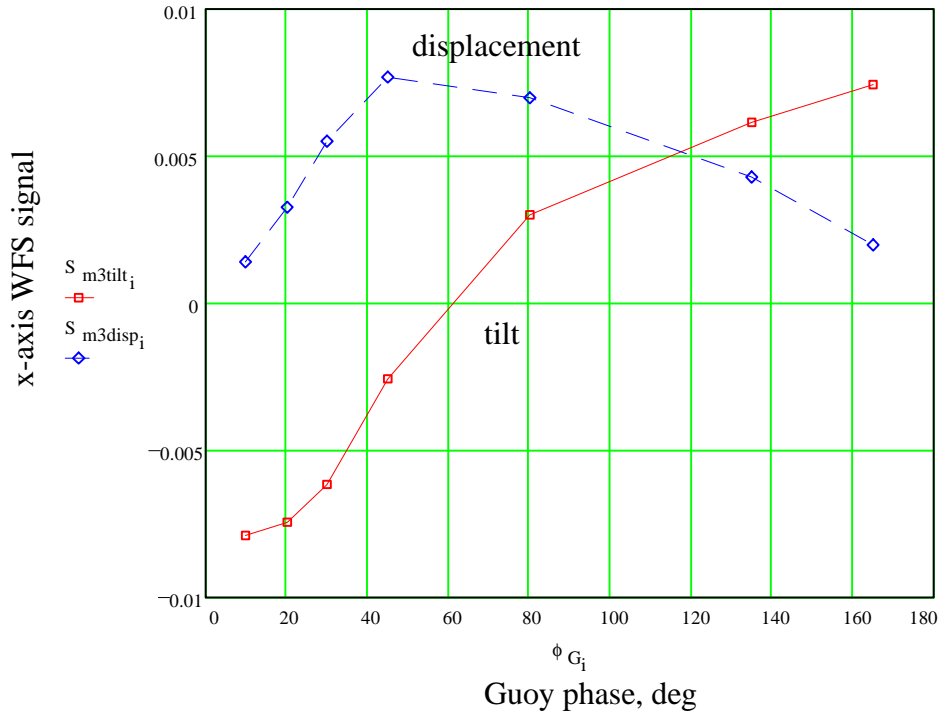


**Figure 58: Summary of WFS signals versus Guoy phase for 0.01 displacement and 0.01 tilt, with +0.9 waves astigmatism**

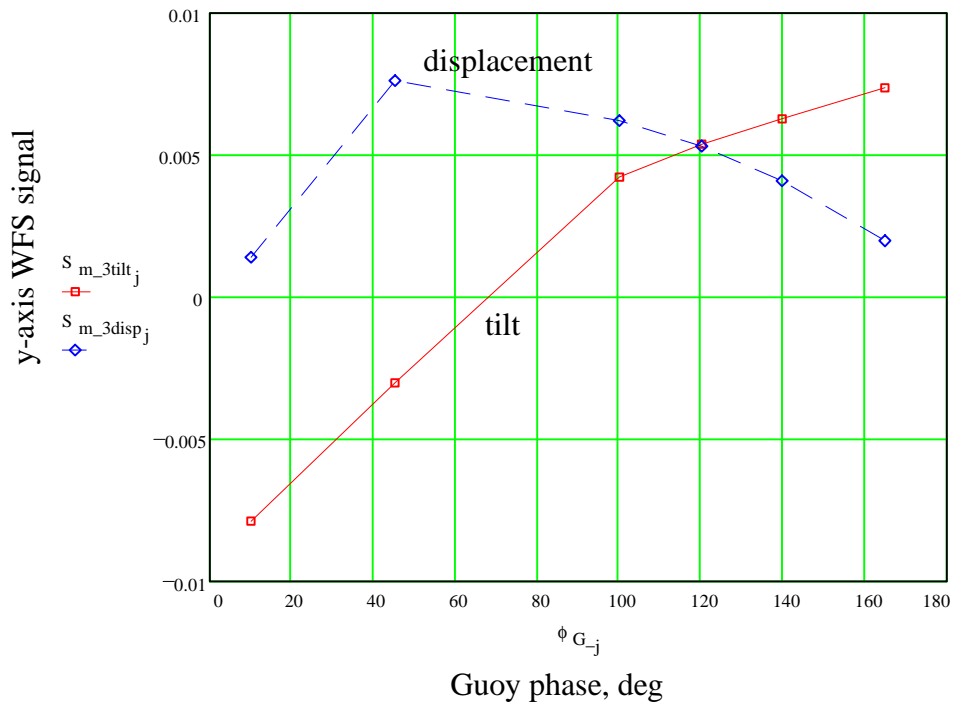


**Figure 59: Summary of WFS signals versus Guoy phase for 0.01 displacement and 0.01 tilt, with -0.9 waves astigmatism**

The +0.9 waves aberration relates to the x-axis signal, and the -0.9 waves aberration relates to the y-axis signal.

The optimum Guoy phase location for placing a tilt or displacement detector can be determined by calculating the tilt or displacement signal contrast ratios.

$R_D = \frac{S_{disp}}{S_{tilt}}$ , and  $R_T = \frac{S_{tilt}}{S_{disp}}$ . The tilt contrast ratio should be  $>5$  to unambiguously detect tilt, and likewise the displacement contrast ratio should be  $>5$  to detect displacement; according to ASC requirements.

The contrast ratios for tilt detection and displacement detection for the x-axis and y-axis are shown in figures 60 and 61, where the smooth curves were calculated by fitting the best cubic spline function to the discrete data points. It can be seen that the same ratios have peaks occurring at different Guoy phases for the x-axis and y-axis.

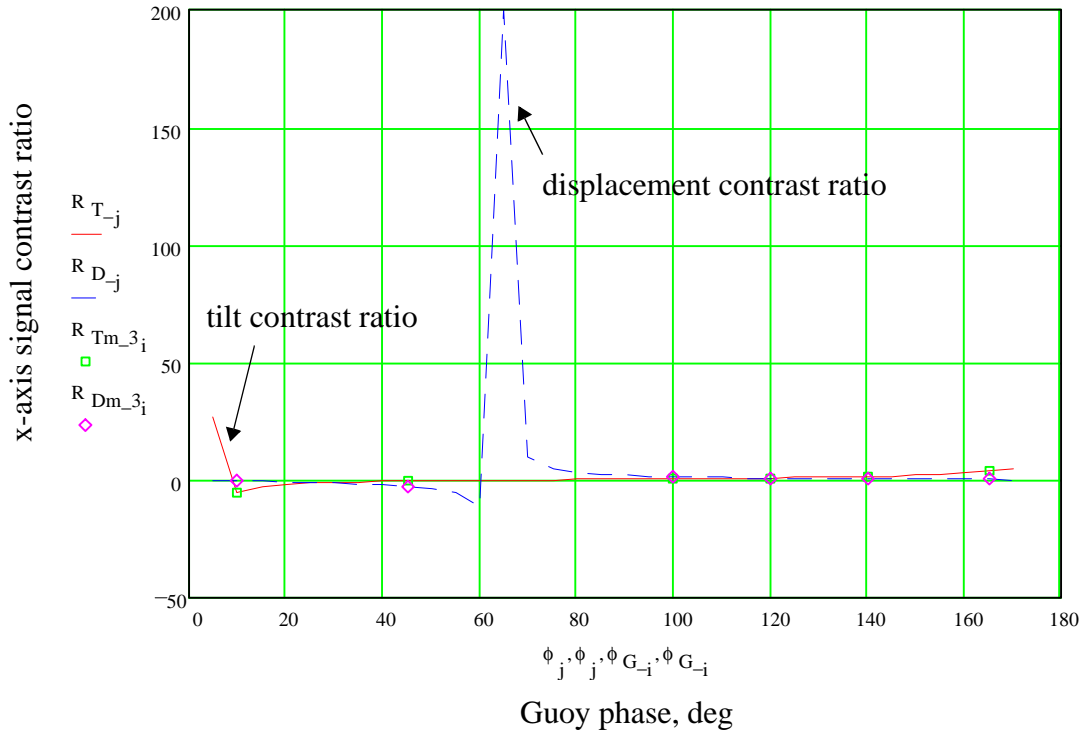


**Figure 60: X-axis contrast ratios for tilt and displacement, 0.9 waves astigmatism**

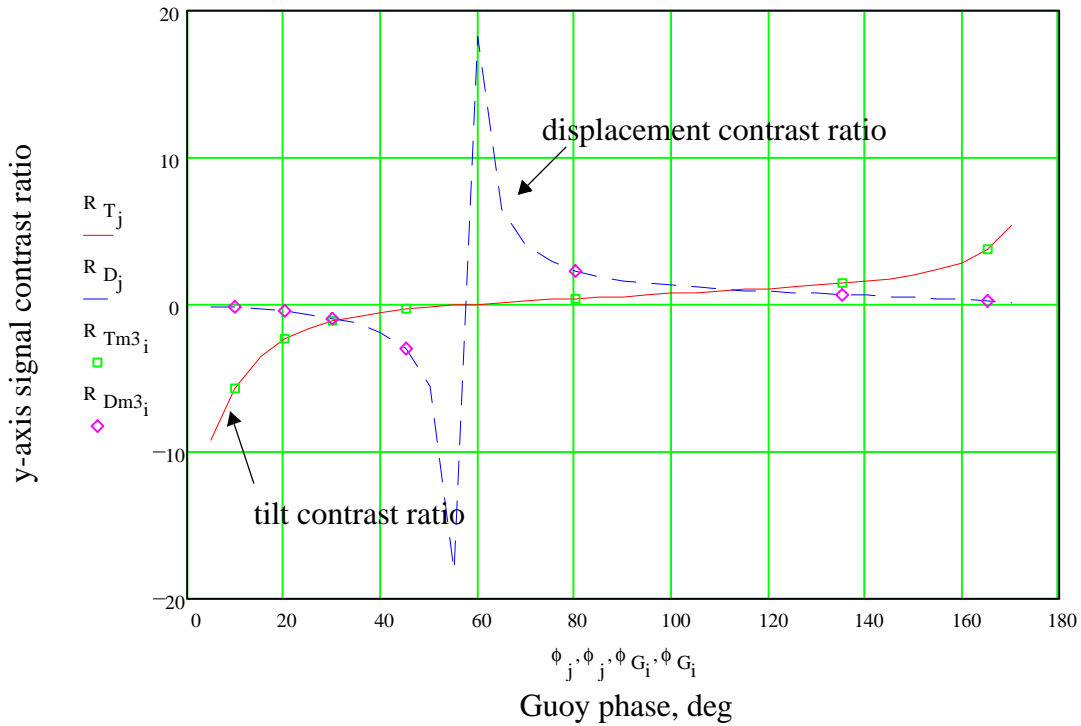


**Figure 61: Y-axis contrast ratios for tilt and displacement, 0.9 waves astigmatism**

A tilt contrast ratio of  $>5$  can be obtained in both axes by placing the tilt detector at 5 deg Guoy phase. Similarly, a displacement contrast ratio of  $>5$  can be obtained in both axes by placing the displacement detector at 65 deg Guoy phase.

#### 14.1.2. 0.98 Waves Spherical Aberration with 1.3 m PO telescope

The ASAP-geometric model was used to calculate the WFS signal for the case  $0.98\lambda$  total spherical aberration on the PO beam optical train using a 1.3 m PO telescope. The details of the aberration calculations are shown in Table 26 on page 87. The actual spherical Zernike coefficient values placed on the optical elements to produce a total 0.98 wave p-v added in an rms manner are shown in Table 27 on page 87.

The contrast ratios for tilt detection and displacement detection for the x-axis and y-axis are shown in figures 62 and 63, where the smooth curves were calculated by fitting the best cubic spline function to the discrete data points. It can be seen that the same ratios have peaks occurring at different Guoy phases for the x-axis and y-axis.

A tilt contrast ratio of  $>5$  can be obtained in both axes by placing the tilt detector at 5 deg Guoy phase. Similarly, a displacement contrast ratio of  $>5$  can be obtained in both axes by placing the displacement detector at 65 deg Guoy phase.

**Table 26: Equivalent Surface Sag for Total 0.98 Wave RMS Spherical Aberration on the 1.3m PO Beam Optical Train**

	<i>p-v</i> <i>aberration</i> <i>per item</i>	<i>p-v</i> <i>aberration</i> <i>per item</i>	<i>net</i> <i>aberration</i>	<i>aberration</i> <i>squared</i>	<i>fractional</i> <i>contribution</i>	<i>least</i> <i>squares</i> <i>linear</i> <i>equivalent</i>
	<i>waves</i> <i>@.6328</i>	<i>waves @ 1.06</i>				
pick-off mirror	0.464	0.276	0.552	0.305	0.320	0.312
PO telescope, primary	0.232	0.138	0.276	0.076	0.080	0.078
PO telescope, secondary	0.232	0.138	0.276	0.076	0.080	0.078
Faraday Isolator	0.509	0.303	0.303	0.092	0.096	0.094
isolator windows (2)	0.209	0.124	0.176	0.031	0.032	0.032
tel fold mirrors (7)	0.186	0.110	0.584	0.341	0.358	0.350
output window	0.209	0.124	0.124	0.015	0.016	0.016
ISC Telescope, objective	0.105	0.062	0.062	0.004	0.004	0.004
ISC Telescope, eyepiece	0.105	0.062	0.062	0.004	0.004	0.004
Guoy 1st lens	0.105	0.062	0.062	0.004	0.004	0.004
Guoy 2nd lens	0.105	0.062	0.062	0.004	0.004	0.004
sum of squares				0.952	1.000	0.976
least squares p-v						0.976

**Table 27: Equivalent Linear Spherical Zernike Coefficients for a Total 0.98 Wave RMS Aberration on the 1.3m PO Beam Optical Train**

	<i>equivalent Zernike aberration on surface,</i> <i>waves @ 1.06</i>
pick-off mirror	-0.156
PO telescope, primary	0.039
PO telescope, secondary	-0.039
Faraday Isolator	-0.094
isolator windows (2)	-0.032
tel fold mirrors (7)	-0.175
output window	-0.016

	<i>equivalent Zernike aberration on surface, waves @ 1.06</i>
ISC Telescope, objective	-0.004
ISC Telescope, eyepiece	-0.004
Guoy 1st lens	-0.004
Guoy 2nd lens	0.004
least squares p-v	0.976

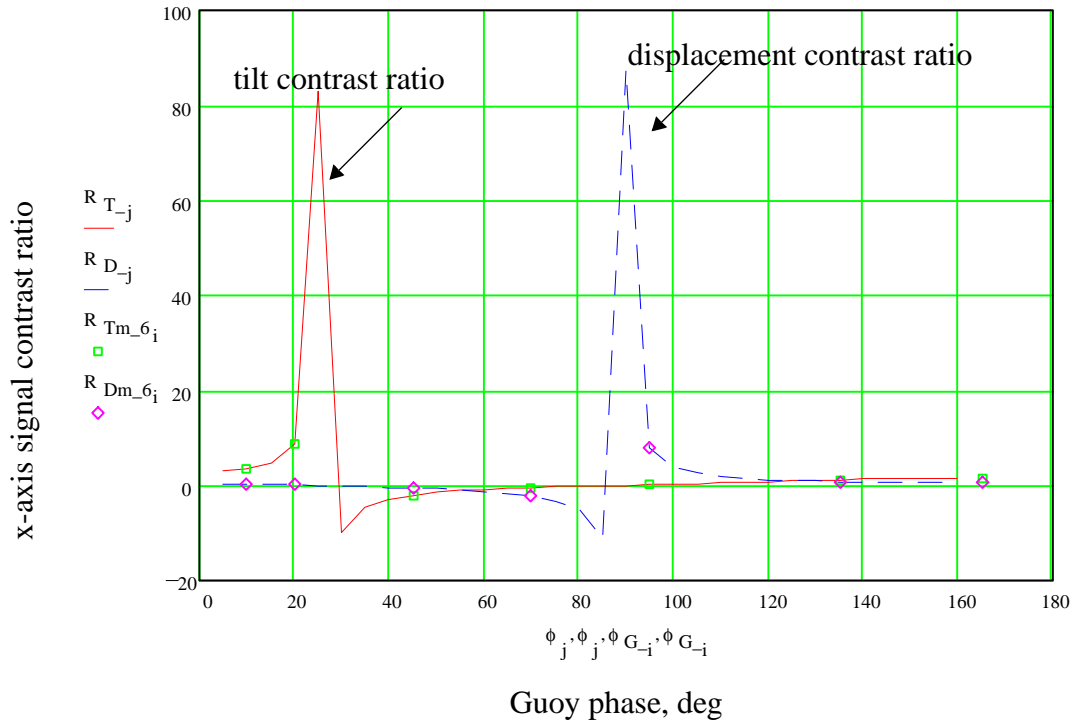


**Figure 62: X-axis contrast ratios for tilt and displacement, 0.98 waves spherical aberration**

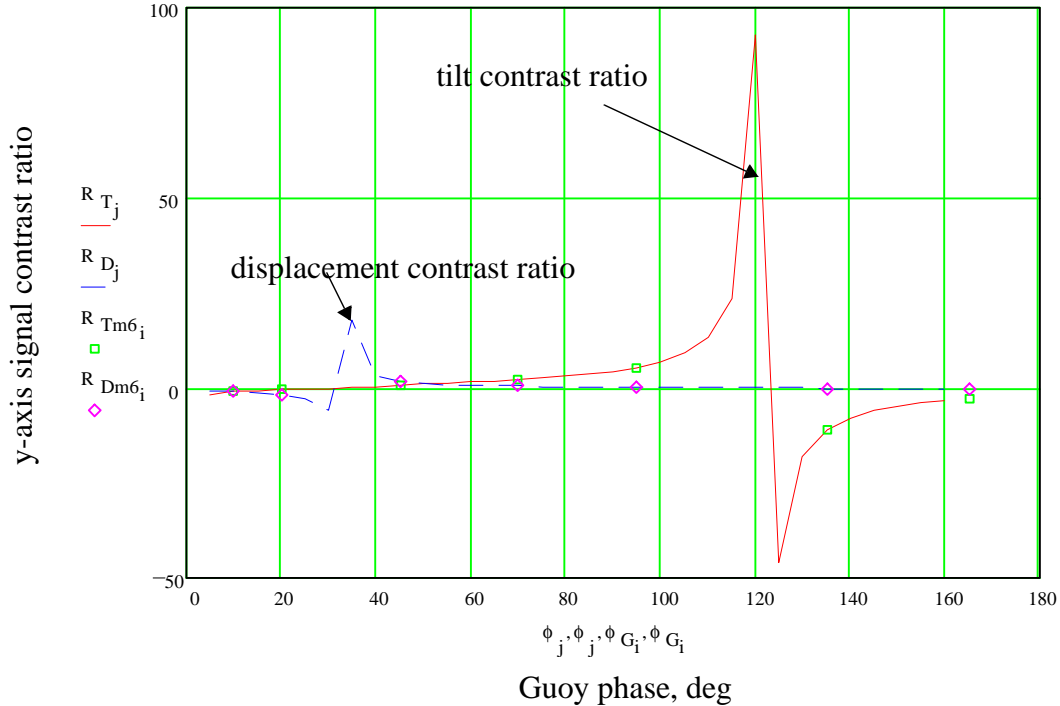


**Figure 63: Y-axis contrast ratios for tilt and displacement, 0.98 wave spherical aberration**

### 14.1.3. Mixed 0.45 Waves Astigmatic, and 0.23 Waves Spherical Aberration with 0.8 m PO telescope

The WFS signal for the mixed case  $\pm 0.45\lambda$  astigmatic and  $0.22\lambda$  spherical aberration on the PO beam optical train using a 0.8 m PO telescope was also calculated. The contrast ratios for tilt detection and displacement detection for the x-axis and y-axis are shown in figures 65 and 64, where the smooth curves were calculated by fitting the best cubic spline function to the discrete data points. It can be seen that the ratios have peaks occurring at different Guoy phases for the x-axis and y-axis.

A tilt contrast ratio of  $>5$  can be obtained in both axes by placing the tilt detector at 10 deg Guoy phase. Similarly, a displacement contrast ratio of  $>5$  can be obtained in both axes by placing the displacement detector at 60 deg Guoy phase.

*The conclusion that can be drawn from these results is that mixed astigmatic and spherical aberrations in the PO beam optical train totalling  $< 1$  wave will produce acceptable results for the WFS signal.*

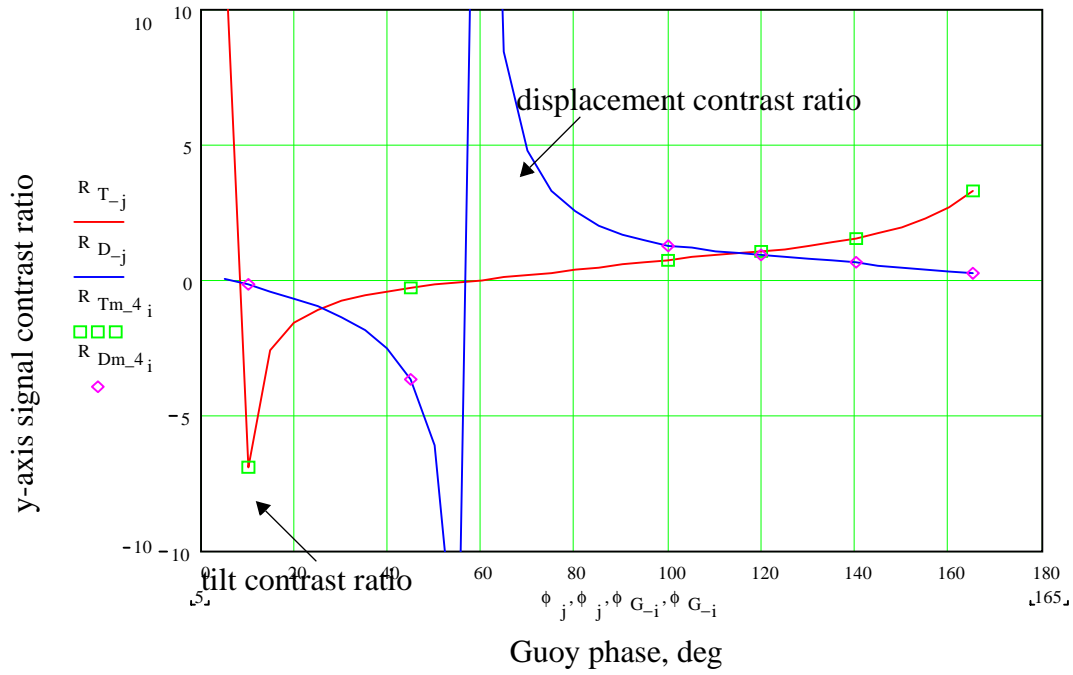


**Figure 64: Y-axis contrast ratios for tilt and displacement, for the mixed case  $\pm 0.45\lambda$  astigmatic and  $0.22\lambda$  spherical aberration**

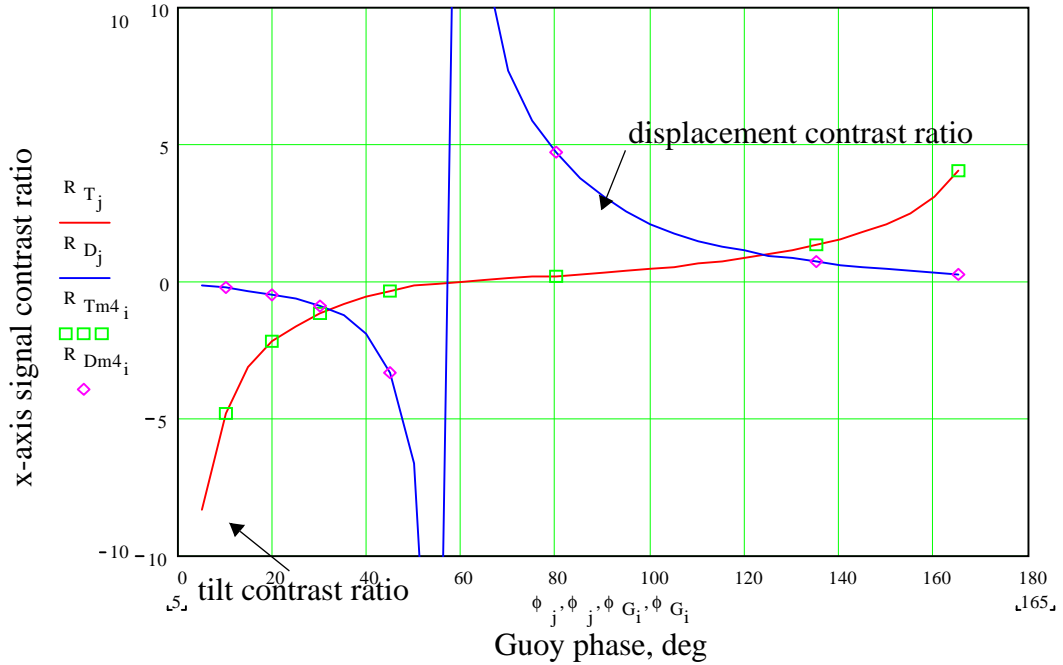


**Figure 65: X-axis contrast ratios for tilt and displacement, for the mixed case  $\pm 0.45\lambda$  astigmatic and  $0.22\lambda$  spherical aberration**

## APPENDIX 5 THERMAL NOISE CONTRIBUTION TO SEI PLATFORM MOTION FROM PO TELESCOPE AND PO MIRRORS

### 15 THERMAL NOISE CONTRIBUTION TO SEI PLATFORM MOTION FROM PO TELESCOPE AND PO MIRRORS

#### 15.1. Thermal Noise Amplitude of a Resonant Mechanical System Coupled to the SEI Platform

The damped self-resonance of the telescope assembly and the PO mirror assembly will add thermal noise amplitude fluctuations to the motion of the SEI platform and subsequently to the suspended test masses. Because of the large mismatch in masses of the objects  $m_i$  compared with the mass of the SEI platform  $M_i$ , the impressed noise effect can be adequately estimated by solving for the thermal noise in the resonant structure and then using the impedance mismatch between the structure and the SEI platform to estimate the resulting recoil of the platform<sup>1</sup>.

The induced noise amplitude on the SEI platform due to the self-resonance of the mounted object is given by

$$x_i(\omega) = \left[ \frac{4k_B T}{M\omega} \cdot \frac{m_i}{M} \cdot \frac{\omega_0^2 \cdot \phi}{(\omega_0^2 - \omega^2)^2 + (\omega_0^2 \cdot \phi)^2} \right]^{\frac{1}{2}} m / \sqrt{\text{Hz}}$$

The damping factor,  $\phi$ , is the reciprocal of the quality factor of the self-resonant object

$$Q = \frac{\Delta\omega}{\omega_0} = 1/\phi$$

#### 15.2. Transfer Of Thermal Noise Amplitude to the Test Mass

The thermal noise impressed on the test mass is attenuated by the transfer function of the SUS in the frequency band 30 to 1000 Hz,

$A_{SUS} = 5 \times 10^{-6}$ , so that the thermal noise amplitude impressed on the test mass is

$$x_{TM} = A_{SUS} \cdot x_i(\omega)$$

---

1. Fred Rabb, Motion of Optical Platforms Driven by Thermal Noise from Spring Elements, LIGO-T970055-00-D



### 15.3. Maximum Noise Amplitude at Resonance

The maximum thermal noise amplitude occurs at resonance,

$$x_i(\omega_0) = \left[ \frac{4k_B T}{M} \cdot \frac{m_i}{M} \cdot \frac{Q}{\omega_0^3} \right]^{\frac{1}{2}} m / \sqrt{\text{Hz}},$$

and the minimum resonant frequency which meets the Science Requirements is given by

$$(\omega_0)_{REQ} = \left[ \frac{4k_B T}{M} \cdot \frac{m_i}{M} \cdot \frac{Q}{x_i(\omega_0)_{REQ}^2} \right]^{\frac{1}{3}} m / \sqrt{\text{Hz}}.$$

The maximum allowed thermal motion requirement at the surface of the SEI platform is given by

$$x_i(\omega_0)_{REQ} = \frac{(x_{TM})_{REQ}}{A_{SUS}}.$$

The maximum allowed thermal motion requirement at the test mass is

specified in the LIGO Science Requirements Document,  $(x_{TM})_{REQ} = 1.0 \times 10^{-20} m / \sqrt{\text{Hz}}$ .

See Seismic Isolation DRD: LIGO-T960065\_02\_D.

Then

$$x_i(\omega_0)_{REQ} = 2 \times 10^{-15} m / \sqrt{\text{Hz}}.$$

#### 15.3.1. Torsional Resonance Model with Discrete Distributed Torques

The PO mirror assembly and the kinematically mounted telescope housing will be modeled as a hollow shaft with discrete applied torques, as shown in figure 66.

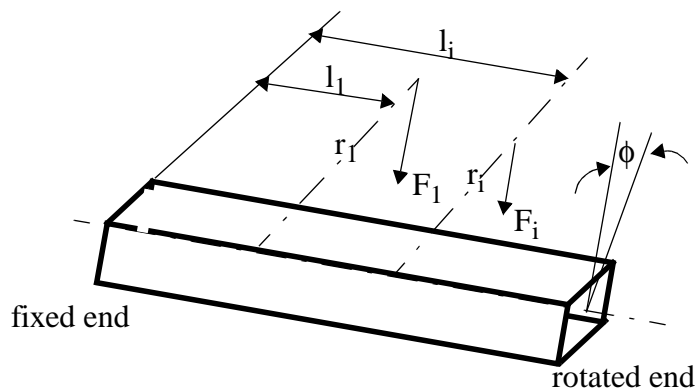


**Figure 66: Hollow shaft model of PO mirror mount, and telescope housing**

### 15.3.1.1 Equivalent Torque

The individual mirror mounts of mass  $m_i$  for the PO mirror and the telescope elements will cause inertial forces due to their acceleration. The inertial forces will be represented as discrete forces located at a radius  $r_i$  from the center of rotation, and a distance  $l_i$  from the fixed end of the shaft. Each torque  $T_i$  will cause the shaft to twist by an angle  $\phi_i$ , where  $J$  is the polar moment inertia of the cross section of the shaft, and  $G$  is the torsional modulus of elasticity.

$$\phi_i = \frac{T_i l_i}{JG}$$

Assuming small twists, the total twist will be the linear sum

$$\phi = \sum \phi_i = \sum \frac{T_i l_i}{JG}.$$

The inertial forces and the resulting torques can be calculated

$$F_i = m_i a$$

$$T_i = r_i m_i a.$$

Then the total twist angle is given by

$$\phi = \frac{a}{JG} \sum r_i m_i l_i.$$

We can define an effective radius, where the composite masses can be located to produce the equivalent torque.

$$\phi = \frac{a}{JG} \sum r_i m_i l_i = \frac{a}{JG} r_{eff} ML, \text{ and}$$

$$r_{eff} = \frac{1}{ML} \sum r_i m_i l_i,$$

where  $L$  is the maximum length of the shaft, and  $M$  is the total mass.

### 15.3.1.2 Effective Spring Constant

An effective spring constant can be defined in terms of the torque and the angular displacement of the shaft.

$$k = \frac{F}{\Delta s} = \frac{T/r_{eff}}{r_{eff}\phi} = \frac{JG}{r_{eff}^2 L}.$$

The torsional modulus of elasticity  $G$  is related to the Young's modulus,

$$G = \frac{E}{2(1 + \mu)},$$

where  $\mu$  is Poisson's ratio and we will assume the value 0.25. Then  $G=0.4E$ .

### 15.3.1.3 Torsional Resonant Frequency

The resonant frequency can now be calculated using the effective spring constant and the total mass.

$$f = \frac{1}{2\pi} \sqrt{\frac{k}{M}}$$

A preliminary design for an aluminum plate PO mirror assembly was modeled as a total mass of 24 lbs at the end of a 12 in hollow shaft at an effective radius of 1.9 in from the axis of rotation (See “Schematic Drawing of the PO Mirror in Its Mount” on page 51.) The calculated torsional resonant frequency is 258 Hz.

Similarly a preliminary design for an aluminum plate telescope assembly, as shown in figure 32, which is rigidly mounted to the SEI platform, was modeled as a total mass of 130 lbs at the end of a 59 in hollow shaft at an effective radius of 3.2 in. The calculated torsional resonant frequency is 80 Hz.

### 15.3.1.4 Bending Resonant Frequency

The bending resonance of the combined mounted telescope assembly, assuming a simply supported distributed beam of weight 114 lbs, was calculated to be approximately 513 Hz.

### 15.3.2. Thermal Noise Amplitude at Test Mass Due to Telescope Assembly

The maximum noise amplitude induced by the telescope assembly mounted to the SEI platform was calculated, assuming the following parameters.

Boltzmann factor	$k_B = 1.38 \times 10^{-23} J/K$
temperature	$T = 300 K$
mass of SEI platform	$M = 1690 kg$
mass of telescope assembly	$m = 59 kg$
resonant frequency of telescope assembly	$\omega_0 = 500 rad/s \approx 80 Hz$
estimated quality factor	$Q = 300$
	$x_i)_{telescope} = 2.5 \times 10^{-21} m / \sqrt{Hz}$ .

This noise amplitude is much smaller than the requirement of  $< 2 \times 10^{-15} m / \sqrt{Hz}$ , and is acceptable.

### 15.3.3. Thermal Noise Amplitude at Test Mass Due to PO Mirror Assembly

This result can be scaled for other parameter values, e.g. the PO mirror assembly mounted to the SEI platform, as follows.

$$x_{TM} = 5.4 \times 10^{-22} \left( \frac{Q}{300} \right)^{\frac{1}{2}} \left( \frac{1000}{\omega_0} \right)^{\frac{3}{2}} \left( \frac{m}{22} \right)^{\frac{1}{2}} m / \sqrt{Hz}.$$

mass of PO mirror assembly	$m = 11 kg$
resonant frequency of PO mirror assembly	$\omega_0 = 1621 rad/s \approx 258 Hz$

quality factor

$$Q = 300,$$

then

$$x_{TM})_{POmirror} = 1.9 \times 10^{-22} \text{ m}/\sqrt{\text{Hz}}.$$

This noise amplitude is much smaller than the requirement of  $< 2 \times 10^{-15}$ , so is acceptable.

## APPENDIX 6 EDGE DIFFRACTION

### 16 EDGE DIFFRACTION

Edge diffraction occurs whenever a coherent wavefront is terminated abruptly at a boundary such as the edge of a mirror, the edge of a baffle, or the edges of an aperture in a baffle. The magnitude of the power diffracted back in the direction of the incident beam, within the acceptance solid angle of the IFO, can be estimated using the Sommerfeld solution for diffraction from a semi-infinite plane with approximations to the Fresnel integral. The simplified geometry of the problem is shown in figure 67 below.

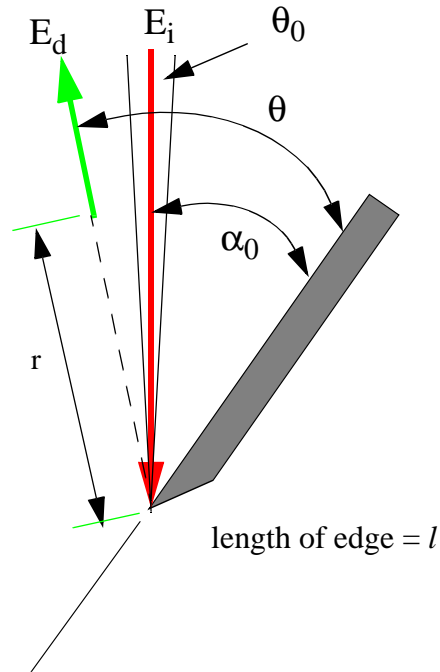


**Figure 67: Edge diffraction geometry**

The diffracted field amplitude a long distance away from the edge,  $kr \gg 1$ , is given approximately by

$$E_d = u_0 \cdot \frac{\sin \frac{\alpha_0}{2} \cdot \sin \frac{\theta}{2}}{\cos \theta + \cos \alpha_0} \cdot \frac{1}{\sqrt{kr}}$$

The diffracted field has a peak value approximately equal to the incident field along the specular direction, i.e.

$E_d = \frac{u_0}{\sqrt{kr}} = E_i$ , for  $\theta = \pi - \alpha_0$ ; so we can evaluate the diffracted field source term at a sufficiently close distance to the edge where the approximation is still valid, e.g.  $r = 10\lambda$ , then

$$u_0 = \sqrt{10k\lambda}, \text{ and}$$

$$E_d = E_i \cdot \sqrt{10\frac{\lambda}{r}} \cdot \frac{\sin\frac{\alpha_0}{2} \cdot \sin\frac{\theta}{2}}{\cos\theta + \cos\alpha_0}.$$

The total power diffracted into the solid angle of the IFO beam is given by

$$P_d = \int E_d^2 dA,$$

where the area element is the differential surface element of a cylinder with height equal to the diffracting edge of length  $l$ , then

$$dA = r d\theta l.$$

The integral must be evaluated within the acceptance angle of the IFO, where  $\theta_0 = 9.3 \times 10^{-6}$  rad is the divergence half-angle of the IFO beam.

$$P_d = \int_{\alpha_0 - \theta_0}^{\alpha_0 + \theta_0} E_i^2 \cdot 10\frac{\lambda}{r} \cdot \left( \frac{\sin\frac{\alpha_0}{2} \cdot \sin\frac{\theta}{2}}{\cos\theta + \cos\alpha_0} \right)^2 \cdot r l d\theta.$$

For typical small values, i.e.  $\theta_0 \ll \alpha_0$ ,

$$P_d = E_i^2 \cdot 10\lambda l \cdot \frac{\sin^2\frac{\alpha_0}{2}}{4\cos^2\alpha_0} \cdot 2\theta_0.$$

The field amplitude can be evaluated from the total integrated power in the Gaussian beam which is incident on the edge.

$$E_i^2 = \frac{P_T}{\pi w^2/2} \cdot e^{-2r_0^2/w^2},$$

where  $P_T$  is the total power in the beam. Then the diffracted power can be written as

$$P_d = \frac{P_T}{\pi w^2/2} \cdot e^{-2r_0^2/w^2} \cdot 10\lambda l \cdot \frac{\sin^2\frac{\alpha_0}{2}}{4\cos^2\alpha_0} \cdot 2\theta_0$$

Aside from the trigonometric factor, the result can be interpreted as a cylindrical wave diffracting from a line source of length  $l$  and width  $10\lambda$  into the solid angle of the IFO.

## 16.1. Effective Edge Length Reduction Due to Coherence Effects

The baffle aperture edge is inclined with respect to the incident beam direction, as shown in figure 68, and the phase of the diffracted light wave varies along the edge due to the optical path differences. The edge-diffracted light within a coherence length will overlap on the COC and will add coherently in amplitude. The resultant amplitude within each coherence region is the algebraic sum of the differential amplitudes along the edge path. Most of the edge will produce a negligible contribution to the net wave amplitude because the optical phase changes rapidly over many cycles, and the principal amplitude contribution will come from small edge segments at the top and bottom of the aperture. Diffracted light from adjacent coherence regions will not overlap on the COC, and the total diffracted power is the sum of the diffracted power from each coherence region.

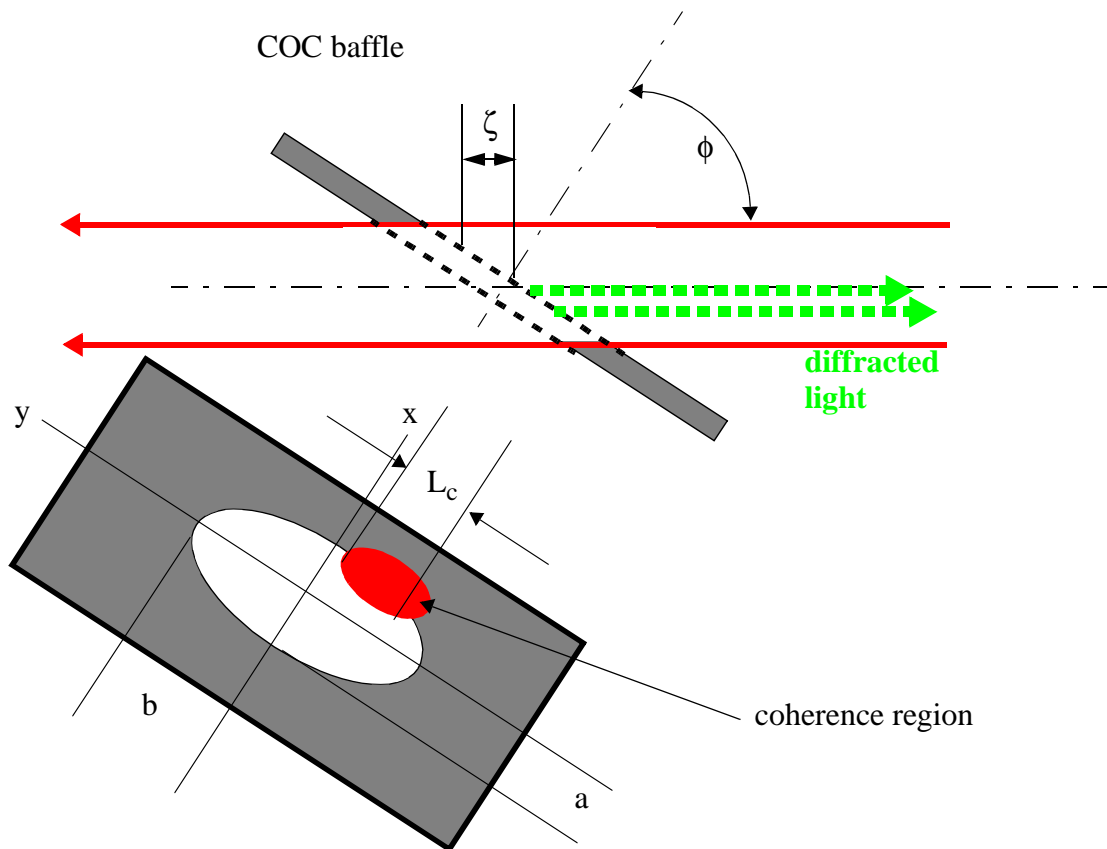


**Figure 68: Coherence region on aperture edge**

We will assume that each portion of the edge has a constant phase relationship with respect to the center of the aperture, even though the entire baffle may be vibrating. The coherence length is essentially the diameter of the resolved spot at the baffle location as seen from the COC at the far

end of the beam tube, which is about the size of the Gaussian beam parameter  $w$  of the main IFO beam.

The total edge-diffracted power into the IFO is given by

$$P = K \sum_j \langle E_j \rangle^2 l \lambda, \text{ where } K \text{ is the Sommerfeld geometric function and } l \text{ is the length of the aperture edge.}$$

The field strength will be expressed in terms of the peak field amplitude along the edge multiplied by an edge efficiency, which will be derived below.

$$P = KE_0^2 \eta_{edge} l \lambda$$

The optical path difference at a position  $y$  along the edge is

$\Delta\zeta = 2y \sin\phi$ , where  $\phi$  is the tilt angle of the baffle. The net light amplitude within the  $j$ th coherence region is the sum of the differential amplitudes along the edge

$$E_j = \frac{E_0}{S} \int_{y_j}^{y_{j+1}} \cos\left(\frac{4\pi y \sin\phi}{\lambda}\right) ds, \text{ where the differential path along the edge can be expressed in terms of the } y \text{ coordinate}$$

$$ds := \frac{dy}{\sin\left[\operatorname{atan}\left[-\sqrt{\frac{b(\phi)^4}{a^2 \cdot y} - \frac{b(\phi)^2}{a^2}}\right]\right]}$$

The semi-major axis of the elliptical aperture,  $b$ , is taken along the  $y$ -axis. The semi-minor axis,  $a$ , is taken along the  $x$ -axis. The arc length along the aperture edge measured from  $y=0$  is given by the path integral.

$$s(y) := \int_0^y \frac{1}{\sin\left[\operatorname{atan}\left[-\sqrt{\frac{b(\phi)^4}{a^2 \cdot u^2} - \frac{b(\phi)^2}{a^2}}\right]\right]} du$$

For tilt angles  $> 5$  deg, there are many wavelengths of optical path length change along the edge within the coherence region which will give a zero contribution, and only a small edge segment within each coherence region gives a non-zero contribution to the diffracted power. In fact, the principal contribution comes from the two edge segments at the top and bottom of the aperture.

A typical size of the coherence length is taken to be the Gaussian beam parameter projected onto the tipped baffle.

$$L_c(\phi) := \frac{w}{\cos(\phi)}$$

And there are

$$N(\phi) := \text{ceil}\left(\frac{b(\phi)}{L_c(\phi)}\right)$$

coherence lengths within an aperture quadrant (the “ceil” function calculates the largest integer value). The number of integral wavelengths within an optical path length is given by (the “floor” function calculates the smallest integer value)

$$N_\lambda(\phi, N) := \text{floor}\left(\frac{\Delta\zeta(\phi, N)}{\lambda}\right)$$

The non-zero contributing edge length within the coherence region is

$$\Delta L(\phi, N) := \frac{(\Delta\zeta(\phi, N) - \lambda \cdot N_\lambda(\phi, N))}{2 \cdot \sin(\phi)}$$

The fraction of the edge in the  $j$ th region which produces edge diffraction is

$$\eta_{\text{edge}j}(\phi, N) := \left[ \begin{array}{c} \bullet y_j(\phi, N) \\ \left[ \frac{1}{s(\phi)} \cdot \cos\left(4 \cdot \pi \cdot y \cdot \frac{\sin(\phi)}{\lambda}\right) \cdot \frac{1}{\sin\left[\text{atan}\left[-\sqrt{\frac{b(\phi)^4}{a^2 \cdot y^2} - \frac{b(\phi)^2}{a^2}}\right]\right]} \right] dy \\ \bullet y_j(\phi, N) - \Delta L(\phi, N) \end{array} \right]^2$$

and the total edge efficiency is the sum of the  $j$  regions

$$\eta_{\text{edge}}(\phi, N) := \eta_{\text{edge}1}(\phi, N) + \eta_{\text{edge}2}(\phi, N) + \eta_{\text{edge}3}(\phi, N) + \eta_{\text{edge}4}(\phi, N)$$

The edge efficiency is plotted in figure 69 as a function of tilt angle of the baffle aperture in radians, for  $N=4$  coherence regions within the aperture quadrant. The maximum edge efficiency is described reasonably well by the expression,

$$\eta_{\text{edgmax}} = \frac{1 \times 10^{-6}}{\phi}, \text{ as shown in figure 69.}$$

From the figure we can estimate that the edge diffraction efficiency for a 5 degree tilted baffle is  $< 1 \times 10^{-5}$ , and for a 57 degree tilted baffle is  $< 1 \times 10^{-6}$ .



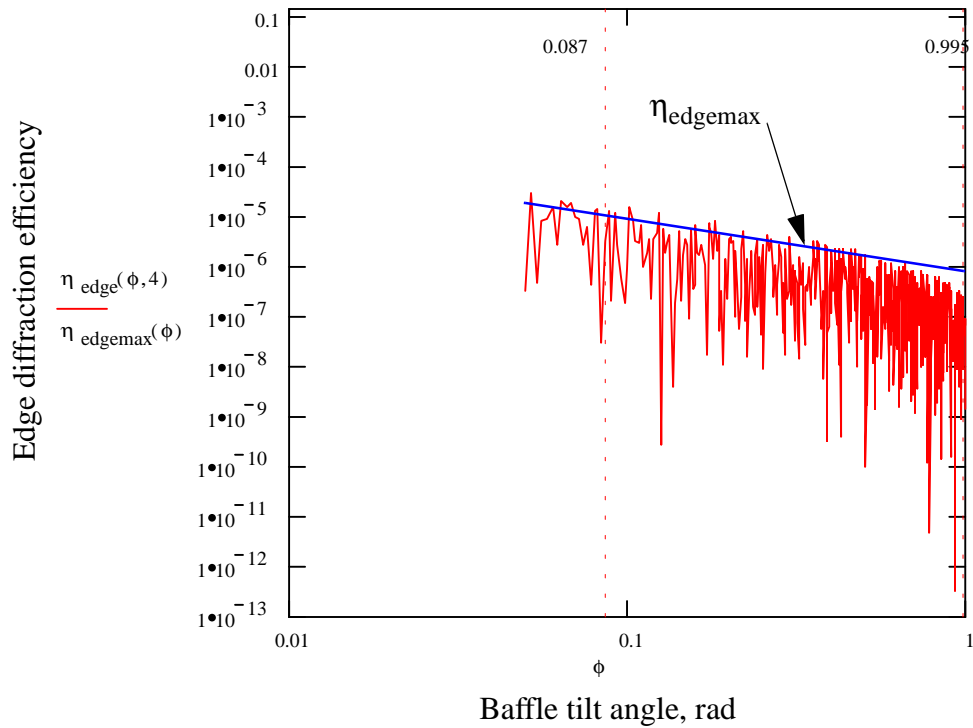


**Figure 69: Edge diffraction efficiency, with N=4, as a function of baffle tilt angle**

## 16.2. Edge Diffraction from COC Baffle Aperture

The edge diffraction of the main arm cavity beam from the aperture of the COC baffles can be calculated using the formalism developed above.

The Gaussian beam waist,  $w_0=35.1$  mm, is located 975000 mm from the 4K ITM mirror. The distance to the 4K ETM mirror is 3025000 mm. The Gaussian beam parameters in millimeters at the ITM and ETM mirrors can be calculated using the Gaussian beam expansion formula.

$$w_{4KITM} := w_0 \left[ 1 + \left( \frac{\lambda \cdot z_{ITM}}{\pi \cdot w_0^2} \right)^2 \right]^{0.5}$$

Then

$w_{4KITM}$	36.3 mm
$w_{4KETM}$	45.6 mm

The edge-diffracted power of a 5000 watt beam into the IFO from the ITM COC baffle with a 124 mm radius aperture as a function of complimentary incidence angle of the baffle surface, is shown in figure 70.

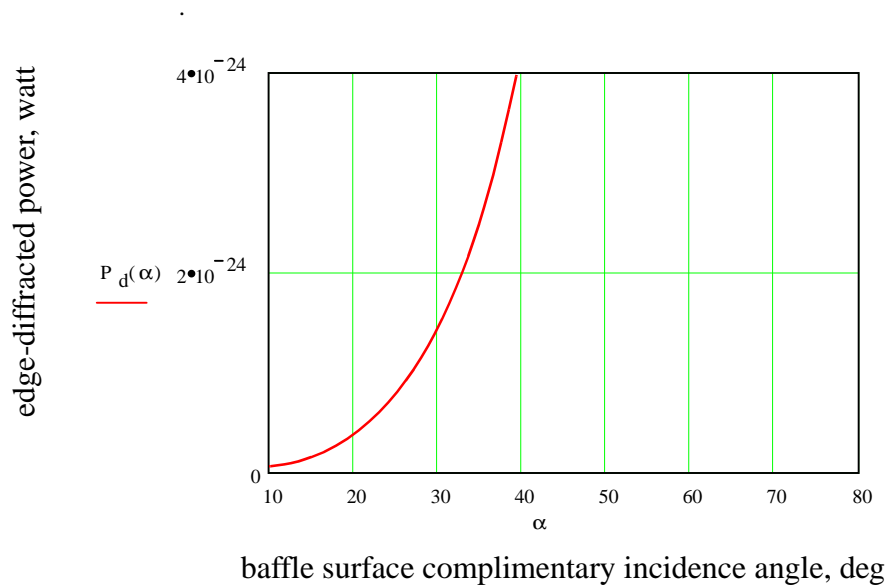


**Figure 70: Edge-diffracted power into IFO from 5000 watt beam passing through 248 mm diameter aperture in the tilted ITM COC baffle**

From figure 70 we can determine that the diffracted power into the IFO is  $2.0 \times 10^{-24}$  watts from the ITM COC baffle, tilted 33 deg from the beam axis. Similarly; the power diffracted into the IFO from the ETM COC baffle, with a 124 mm radius aperture, was calculated to be  $6.4 \times 10^{-21}$  watts.